Submesoscale dynamics in the Bay of Biscay continental shelf

Özge Yelekçi

▶ **To cite this version:**

Özge Yelekçi. Submesoscale dynamics in the Bay of Biscay continental shelf. Oceanography. Université Pierre et Marie Curie - Paris VI, 2017. English. ⟨NNT : 2017PA066529⟩. ⟨tel-01886804⟩

HAL Id: tel-01886804

https://theses.hal.science/tel-01886804v1

Submitted on 3 Oct 2018

HAL is a multi-disciplinary open access archive for the deposit and dissemination of scientific research documents, whether they are published or not. The documents may come from teaching and research institutions in France or abroad, or from public or private research centers.

L'archive ouverte pluridisciplinaire **HAL**, est destinée au dépôt et à la diffusion de documents scientifiques de niveau recherche, publiés ou non, émanant des établissements d'enseignement et de recherche français ou étrangers, des laboratoires publics ou privés.

HAL Authorization

Université Pierre et Marie Curie

École doctorale de Sciences de l'Environnement – ED 129

IFREMER, Laboratoire d'Océanographie Physique et Spatiale

The submesoscale Dynamics in the Bay of Biscay Continental Shelf

Par Özge Yelekçi

Thèse de doctorat d'Océanogaphie Physique

Dirigée par Gilles Reverdin, Guillaume Charria et Xavier Capet

Présentée et soutenue publiquement le 23 Octobre 2017

Devant un jury composé de :

M. Morel Yves , Directeur de Recherche, LEGOS, Toulouse	Rapporteur
M. Zakardjian Bruno, Professeur, MIO, Toulon	Rapporteur
Mme. Bouruet-Aubertot Pascale, Professeur, LOCEAN, Paris	Examinatrice
Mme Petrenko Anne, Maître de Conférence, MIO, Marseille	Examinatrice
M. Sudre Joël, Ingénieur de Recherche, LEGOS, Toulouse	Invité
M. Reverdin Gilles, Directeur de Recherche, LOCEAN, Paris	Directeur de thèse
M. Charria Guillaume, Cadre de Recherche, LOPS, Brest	co-encadrant de la thèse
M. Capet Xavier, Chargé de Recherche, LOCEAN, Paris	co-encadrant de la thèse

Abstract: This thesis explores the submesoscale dynamics in the Bay of Biscay continental shelf. The research consists of two main parts. In the first part, submesoscale features over the shelf are identified using remotely sensed high resolution sea surface temperature (SST) images by MODIS. Front detection is achieved through singularity exponents, a novel method of calculating irregularities on the SST fields, and an index for the frontal activity is generated. Results are complemented with 2.5 km horizontal resolution numerical simulations. Based on the investigation of the dominant physical drivers for regions that host increased frontal activity, different types of fronts are distinguished. Three main types of fronts are presented: *i)* tidal mixing fronts along the coast and most significantly in the Ushant region; *ii)* shelf break front related to internal tidal wave activity; *iii)* fresh water fronts along the edge of the river plumes in winter. In the second part, a realistic hydrodynamical model of Bay of Biscay is set up. The model has a 1 km horizontal resolution and 40 σ vertical layers. A scale decomposition, that distinguishes large, meso-, and submesoscale components, is applied to modeled fields. Diagnostics is based on the assumption that the submesoscale features in the upper ocean are the result of baroclinic instabilities. Available potential energy (APE) is then converted to eddy kinetic energy (EKE) in time scales in $O(1)$ day or less through this process. Spatial and temporal distributions of the submesoscale component of the vertical buoyancy flux and eddy kinetic energy are investigated. Occurrence of submesoscale dynamics over the shelf has a similar pattern to the observed frontal occurrence. Activity increases in the Ushant region and the coastal regions in summer, whereas, in winter, activity in the vicinity of the fresh water plumes dominates. In summer, dominant dynamic is the tidal fronts along the coast and the Ushant region. EKE conversion time scale in this region is $\sim$ 5 days, which can be considered shorter than mesoscale. In winter, regions of positive buoyancy flux are prominent along the river plumes. They have a time scale of $O(1)$ ($\sim$ 30 hours). This is an indicator that

the submesoscale baroclinic instability is happening at the plume. These findings will provide valuable information for future studies on the submesoscale dynamics and their interactions in coastal regions like continental shelves.

Keywords: submesoscale dynamics, fronts, singularity exponents, remotely sensed sea surface temperature, high resolution numerical ocean model, Bay of Biscay

Résumé : Ce travail de thèse explore la dynamique à sousmésoéchelle sur le plateau continental du golfe de Gascogne. Ces travaux de recherche se décomposent en deux parties. Dans la première partie, les caractéristiques des processus à sousmésoéchelle sur le plateau sont identifiées à l'aide de données satellites à haute résolution de température de surface de la mer (SST) issues du capteur MODIS. Une détection des fronts est réalisées à l'aide d'exposants de singularité, une approche récente pour identifier les irrégularités dans les champs de SST. A partir de ces exposants, un index de l'activité frontale est généré. Les résultats sont complétés par des simulations numériques à 2.5 km de résolution spatiale. Sur la base de l'analyse des principaux forçages physiques des régions présentant une activité frontale intense, différents types de fronts sont distingués. Trois types principaux de fronts sont présentés : *i)* les fronts de marée le long de la côte et plus marqués dans la région d'Ouessant; *ii)* les fronts au niveau du talus continental liés à l'activité des ondes internes; *iii)* les fronts d'eaux dessalées aux limites des panaches de rivières en hiver. Dans la seconde partie, un modèle hydrodynamique réaliste du golfe de Gascogne a été mis en place. Cette configuration a une résolution spatiale de 1 km et 40 niveaux verticaux sigma. Une décomposition d'échelle, permettant de distinguer les coposantes à grande, meso- et sousmesoéchelles, est appliquée aux champs simulés. Un diagnostic est basé sur l'hypothèse que les processus à sousmesoéchelles résultent d'instabilités baroclines. L'énergie potentielle disponible (APE) est ainsi convertie en énergie cinétique tourbillonnaire (EKE) avec des échelles temporelles $O(1)$ jour ou moins grâce à ces processus. Les distributions spatiales et temporelles de la composante à sousmesoéchelle du flux vertical de flottabilité et de l'énergie cinétique tourbillonnaire sont analysées. L'occurrence de processus à sousmesoéchelle sur le plateau a une structure similaire à l'occurrence frontale observée. L'activité est plus intense dans la région d'Ouessant et les régions côtières en été, alors qu'en hiver, l'activité à proximité des panaches d'eaux dessalées domine. En été, la dynamique dominante

est associées aux fronts de marée le long des côtes et dans la région d'Ouessant. En hiver, les régions avec un flux vertical de flottabilité positif apparaissent le long des panaches de rivières. Ces processus ont une échelle temporelle $O(1)$ jour ($\sim$ 30 heures). Ces échelles temporelles sont un indicateur de la présence d'instabilités baroclines à sousmésoéchelle à proximité du panache. Ces résultats apportent une information importante aux futures études sur la dynamique à sousmésoéchelle et ses interactions en région côtières telles que les plateaux continentaux.

Mots clés: dynamique à sousmésoéchelle, fronts, exposants de singularité, données satellites de température de surface de la mer modèle numérique océanique à haute résolution, golfe de Gascogne

Teşekkürler

İlk olarak beni hayatımın her anında destekleyen ve eğitimim için sayısız fedakarlıkta bulunan çok sevdiğim aileme kocaman teşekkür ederim. En küçük yaşlarımdan itibaren merağımı ve bilme istegimi hep beslemeleri ve beni bilime teşvik edişleri akademideki yolculuğumu sürdürmemdeki en büyük yardımcım oldu. Her ihtiyacim olduğunda koşarak yanıma gelen annecigim Ülkü'ye ve her zor anımda içimi rahatlatan babacığım Kemal'e sonsuz kere teşekkürler. Elin memleketinde hiçbir zaman yalnız hissetmememi sağlayan, her an yanımda olan abiciğim Erman'a ve yengeciğim Ayşe'ye yüz bin milyon kucak teşekkürler.

Doktora çalışmamın başından sonuna bana yol gösteren ve değeri ölçülemez tecrübeler edinmemi sağlayan danışmanlarım Gilles, Guillaume, ve Xavier'e çok minettarım. Özellikle Guilaume'un akademide eşine çok zor rastlanan erdemine, çalışma etiğine, yapıcılıgına ve öğrencilerine duyduğu saygı ve güvene yakından tanık olmak hayatımdaki en büyük şanstır. Ayrıca Ifremer'deki ekibimize, başta Sebastian ve Frederic olmak üzere, bana aktardıkları muazzam tecrübeleri ve sayısız sorularımı cevapladıkları için çok teşekkür ederim.

Bir bankta tanıştığımız o günden beri hayatımı kat kat zenginleştiren canım arkadaşım Pınar'a çok kocaman teşekkür ederim. Brest'ten Istanbul'a teşekkürden yol döşesem yine de minnetimi anlatmaya yetmez. Sensiz bu tez hayatta olmazdı. İyi ki varsın, iyi ki arkadaşımsın, seni çok seviyorum.

Ve canım Mişa'm. Evrenin en saf ve sonsuz sevgisini bana verdiğin için teşekkür ederim. Hayatın ne kadar da anlamsız oldugunu bana gösterdiğin için, bitmeyen neşen, sevincin, ve sadece varolduğun için teşekkür ederim. Nerede olursan ol ömrüm boyunca senin sevgini her an hatırlayacağım ve seni buradan sevmeye devam edeceğim.

Contents

1 Introduction **1**

1.1 General Context 1

1.2 The Bay of Biscay 2

1.3 Submesoscale Processes 6

1.3.1 Governing Equations 6

1.3.2 (Submeso-)Scaling 9

1.3.3 Submesoscale dynamics 11

1.4 Objectives 12

2 Spatial and Seasonal Distributions of Frontal Activity over the French Continental Shelf in the Bay of Biscay **15**

2.1 Introduction 16

2.2 Data and methods 19

2.2.1 Remotely sensed Sea Surface Temperature 19

2.2.2 Numerical Experiments 20

2.2.3 Singularity Exponents 25

2.3 Observed Frontal Activity 29

2.3.1 Variability of Sea Surface Temperature 29

2.3.2 Spatio-temporal variability of frontal activity 32

2.4 Modeled Frontal Activity 38

2.4.1 Spatio-temporal variability of frontal activity 38

2.5 Discussion 45

2.5.1 Freshwater fronts 45

2.5.2 Tidal fronts 51

2.5.3 Shelf break front 54
2.6 Conclusion 57
2.7 Acknowledgments 58

3 Submesoscale Regimes in the Bay of Biscay Continental Shelf 61

3.1 Introduction 62
3.2 MARS3D Numerical Model 62
3.2.1 Model Description 62
3.2.2 Bay Of Biscay Fine resolution (BOBF) Configuration 69
3.2.3 Modeled General Circulation and Hydrology 75
3.2.4 Model Skill Assesment 79
3.3 Submesoscale Diagnostics 89
3.3.1 Scale Decomposition 89
3.3.2 Submesoscale Vertical Buoyancy Flux and Eddy Kinetic Energy . 94
3.4 Discussion 103

4 Conclusions and Perspectives 109

4.1 Conclusions 109
4.2 Perspectives 112

Bibliography 115

List of Figures

1.1 Bathymetry and geographical features of the Bay of Biscay, from Eric Gaba, Wikimedia Commons. 3

1.2 Schematic illustration of circulation in the Bay of Biscay, derived from Koutsikopoulos and Le Cann (1996). 5

2.1 Map of the Bay of Biscay north of 45°N with bathymetry (30, 50, 100, 125, 150, 200 and 500 m isobaths are additionally drawn in gray), showing important geographical features and the locations of the boxes over which time-series analyses are performed (red). 17

2.2 Comparison between observed (SEVIRI satellite SST) and modeled (PREVIMER) sea surface temperature. a) Mean bias between model and observations for the year 2010. b) Temporal evolution of the SST bias during 2010. The shape of the curves represents the spatial standard deviation. 23

2.3 Normalized distribution of the misfit (modeled - observed) in a) temperature and b) salinity from RECOPESCA in situ profiles (only for profiles deeper than 100 m) for three vertical layers: 0-20 m depth (left), 20-40 m depth (middle), and 40-100 m depth (right). 24

2.4 An example of a) remotely sensed sea surface temperature, b) the corresponding singularity exponent field (zoom: selected frontal pixels in red), c) gradient magnitude of the remotely sensed sea surface temperature versus the corresponding singularity exponent (area between the dashed lines is the range of frontal pixel selection) on 27/01/2008 (isolines represent the 30, 50, 100, 200, 250 and 500 m depths). 28

2.5 Seasonally averaged remotely sensed sea surface temperature from 2003 to 2013 over a) winter (January, February, March), b) spring (April, May, June), c) summer (July, August, September), and d) autumn (October, November, December). Colorscales differ for each panel, but range by schematically 5 °C. 30

2.6 Front occurrence frequency of the MODIS remotely sensed sea surface temperature expressed in percentage of number of times a pixel is cloud-free from 2003 to 2013 in a) winter (January, February, March), b) spring (April, May, June), c) summer (July, August, September), and d) autumn (October, November, December) expressed in percentage of number of times a pixel is cloud-free. 34

2.7 Observed monthly averaged front occurrence frequency in each of the regions defined in Figure 2.1. Error represents one standard deviation centered around the average. 37

2.8 Front occurrence frequency of the modeled sea surface temperature expressed in percentage of number of times a pixel is cloud-free from 2006 to 2013 in a) winter (January, February, March), b) spring (April, May, June), c) summer (July, August, September), and d) autumn (October, November, December). 40

2.9 Monthly averaged front occurrence frequency in each of the regions defined in Figure 2.1. Error bars represent one standard deviation centered around the average. 42

2.10 Singularity exponents of sea surface temperature (blue) and its climatology (red) from PREVIMER model simulations averaged over box a) L, b) U, and c) S (Figure 2.1) from 2006 to 2013. 44

2.11 Remotely sensed sea surface temperature (a), modeled sea surface temperature (b), temperature (c) and salinity (d) along transect (black line on (b)) from the PREVIMER model simulations on 11/02/2008. 49

2.12 Remotely sensed sea surface temperature (a), modeled sea surface temperature (b), temperature (c) and meridional velocity (d) along transect (black line on (b)) from the PREVIMER model simulations on 26/10/2006. 50

2.13 Remotely sensed sea surface temperature (a), modeled sea surface temperature (b), and temperature (c) along transect (black line on (b)) from the PREVIMER model simulations on 14/08/2013. 53

2.14 Remotely sensed sea surface temperature (a), modeled sea surface temperature (b), and temperature (c) along transect (black line on (b)) from the PREVIMER model simulations on 20/10/2007. 56

3.1 BOBF configuration model domain and bathymetry, showing the locations of Loire and Ushant subregions where temporal analyses are applied. 70

3.2 Examples of modeled sea surface temperature from a) REF1, b) REF2, c) REF3, d) REF4, e) REF6, and e)REF7 of the sensitivity simulations (Table 3.1) on 12/02/2009. 74

3.3 Examples representing the winter time conditions of modeled sea surface a) temperature, b) salinity, c) density, d) density gradient, e) velocity on 02/04/2010. The isolines represent the 30, 50, 125, 150, and 250 m isobaths. 77

3.4 Examples representing the summer time conditions of modeled sea surface a) temperature, b) salinity, c) density, d) density gradient, e) velocity on 08/07/2010. The isolines represent the 30, 50, 125, 150, and 250 m isobaths. 78

3.5 Locations of the RECOPESCA profiles that are compared to BOBF simulations, and four subregions defined for detailed comparisons. 79

3.6 Composite comparison of BOBF simulations to RECOPESCA dataset. Modeled *vs.* (modeled - measured) temperature (top) and salinity (bottom). White ellipses are drawn such that their major(minor) axes is one standard deviation (σ) of the data along x(y), and the center is the point of maximum counts for the respective panels. (Locations of profiles in Figure 3.5). 80

3.7 Detailed comparison of BOBF simulations to RECOPESCA dataset. Modeled *vs.* (modeled - measured) temperature from a) La Chapelle bank, b) Iroise sea, c) southeast Bay of Biscay, and d) south of Brittany (Locations of profiles in Figure 3.5). Data are color coded with respect to month (top) and depth (bottom) for each panel. 83

3.8 Detailed comparison of BOBF simulations to RECOPESCA dataset. Modeled *vs.* (modeled - measured) salinity from a) La Chapelle bank, b) Iroise sea, c) southeast Bay of Biscay, and d) south of Brittany (Locations of profiles in Figure 3.5). Data are color coded with respect to month (top) and depth (bottom) for each panel. 84

3.9 Front occurrence frequency of the MODIS remotely sensed sea surface temperature expressed in percentage of number of times a pixel is cloud-free from 2003 to 2013 in a) winter (January, February, March), b) spring (April, May, June), c) summer (July, August, September), and d) autumn (October, November, December). The isolines represent the 30, 50, 125, 150, and 250 m isobaths. 86

3.10 Front occurrence frequency of the modeled sea surface temperature from BOBF simulations expressed in percentage of number of times a pixel is cloud-free from 2009 to 2010 in a) winter (January, February, March), b) spring (April, May, June), c) summer (July, August, September), and d) autumn (October, November, December). The isolines represent the 30, 50, 125, 150, and 250 m isobaths. 88

3.11 Modeled large, meso-, and submesoscale components of w (10^{-4} m s^{-1}) (top), b (10^{-3} m s^{-2}) (middle), and the comparison of the five most dominant wb (10^{-7} m^2 s^{-3}) terms to total wb (bottom), from 7 m depth, averaged over Loire subregion (Figure 3.1). 92

3.12 Examples of modeled large, meso-, submesoscale components, and total wb on 15/03/2010. The isolines represent the 30, 50, 125, 150, and 250 m isobaths. 93

3.13 Vertically averaged submesoscale vertical buoyancy flux ($w''b''$ - top) and eddy kinetic energy (EKE'' - bottom) simulated in 2010 using the BOBF for the winter season (January-February-March). The isolines represent the 30, 50, 125, 150, and 250 m isobaths. 95

3.14 Vertically averaged submesoscale vertical buoyancy flux ($w''b''$ - top) and eddy kinetic energy (EKE'' - bottom) simulated in 2010 using the BOBF for the spring season (April-May-June). The isolines represent the 30, 50, 125, 150, and 250 m isobaths. 97

3.15 Vertically averaged submesoscale vertical buoyancy flux ($w''b''$ - top) and eddy kinetic energy (EKE'' - bottom) simulated in 2010 using the BOBF for the summer season (July-August-September). The isolines represent the 30, 50, 125, 150, and 250 m isobaths. 99

3.16 Vertically averaged submesoscale vertical buoyancy flux ($w''b''$ - top) and eddy kinetic energy (EKE'' - bottom) simulated in 2010 using the BOBF for the autumn season (October-November-December). The isolines represent the 30, 50, 125, 150, and 250 m isobaths. 101

3.17 Climatology of vertically averaged EKE'' and $w''b''$ averaged over Loire and Ushant subregions (Figure 3.1). 102

3.18 Climatology of vertically averaged $w''b''$ and components of EKE computed with velocities that are mesoscale (u'), submesoscale (u''), a combination of both ($u'u''$) averaged over Loire subregion (Figure 3.1). . . . 103

List of Tables

3.1 List of sensitivity simulations. (IC: initial conditions, OBC: open boundary conditions, T: temperature, S: salinity, U: barotropic current velocity, UZ: 3D current velocity, η: free surface elevation) 72

Chapter 1

Introduction

Contents

1.1 General Context 1

1.2 The Bay of Biscay 2

1.3 Submesoscale Processes 6

1.3.1 Governing Equations 6

1.3.2 (Submeso-)Scaling 9

1.3.3 Submesoscale dynamics 11

1.4 Objectives 12

1.1 General Context

"Far and away, the most impressive discovery ... is that the submesoscale ocean (less than 100 km) is far more complex dynamically than ever imagined."

Paul Scully-Power [†]

With the start of space missions, humans, for the first time, were able to look at the Earth's oceans in a way we were not able to before. These were the first synoptic observations of the fact that the oceans, like the atmosphere, have weather (Munk et al.,

[†] Paul Scully-Power is the first trained oceanographer flown to orbit by NASA in 1984. From Scully-Power (1986), post-mission analysis.

2000). In other words, the properties of the surface ocean vary greatly in a wide range of scales. Among them, the mesoscale acts as a key player for distributing heat and salt in ocean. However, while the observations had become more available and higher in resolution, what revealed itself is that there exists a whole other ocean dynamics at scales smaller than those mesoscale fronts, vortices, and such, which is called the submesoscale range.

In this context, the present study aims at investigating the submesoscale processes over a continental shelf in a basin constrained by a macro-tidal dynamics.

1.2 The Bay of Biscay

Geography

This study focuses on the French continental shelf in the Bay of Biscay(Figure 1.1). This region covers in the north, the Armorican shelf from the English Channel to the Plateau de Rochebonne with an average width of 150 - 180 km, and in the south, the northern part of the Aquitaine shelf with an average width of 50 - 150 km (Koutsikopoulos and Le Cann, 1996). This portion of the shelf is the receiver of substantial amounts of fresh water from the two major rivers Loire and Gironde with an annual mean outflow of $\sim$ 900 m^3 s^{-1} (min. $\sim$ 200 m^3 s^{-1} in summer, max. $\geq$ 3000 m^3 s^{-1}, in winter-spring) for each, and to a smaller degree Vilaine river with an annual mean outflow of $\sim$ 100 m^3 s^{-1} (Puillat et al., 2004; Lazure et al., 2006).

Continental shelf circulation

Surface circulation over the shelf shows strong seasonal variability (*e.g.* Pingree et al. (1999); van Aken (2002)). Charria et al. (2013) observed, from drifter data, that

Figure 1.1: Bathymetry and geographical features of the Bay of Biscay, from Eric Gaba, Wikimedia Commons.

from October to March a clear (10 - 15 cm s^{-1}) poleward flow, whereas from April to September a weaker ($\leq$ 2.5 cm s^{-1} in summer) equatorward flow exists. The general circulation can be investigated under three main drivers: wind, tides, and density (Figure 1.2) (Koutsikopoulos and Le Cann, 1996). Over the shelf, the semi-diurnal (M2) tide is the dominant component (Le Cann, 1990). Tidal currents along the coast south of Brittany are $\leq$ 10 cm s^{-1}, and over the shelf $\sim$ 30 cm s^{-1} (Le Cann, 1990; Pingree et al., 1982). The residual current over the Armorican shlef is measured to be weak ($\sim$ 3 cm s^{-1}) (Pingree and Le Cann, 1989; Le Boyer et al., 2009; Kersalé et al., 2016). Dominant winds in the region are southwesterly (SW) in autumn-winter and north-

westerly (NW) in spring-summer, and generate currents $\sim$ 10 cm s^{-1} (Puillat et al., 2006). The direction of the flow induced is SW-S by NW winds, and the reverse by SW winds (Puillat et al., 2006, 2004; Pingree and Le Cann, 1989; Pingree et al., 1999). The modeling study by Lazure and Jégou (1998) showed that the density gradients induced by Loire and Gironde in vicinity of estuaries drive currents of $\sim$ 10 cm s^{-1} towards the north. In winter, when the runoff is at a maximum, onshore SW winds contain northward propagating plumes along the coast, whereas in spring and summer, when the runoff drops, NW winds (the upwelling favorable direction for coastline configuration north of 45N) detach the plumes from the coast and induce offshore spreading (Lazure and Jégou, 1998; Puillat et al., 2006, 2004).

Density gradients are also driving other major features over the continental shlef in the Bay of Biscay as the autumn current (Lazure and Jégou, 1998), linked with bottom density gradient with a strong interannual varibility (*i.e.* the current is not observed every autumn). Another jet-like feature related with density gradients and generated after the setup of winds along the Spanish coast is the Landes current flowing to the North through short time events (Batifoulier et al., 2012, 2013). These different circulation schemes related to intermittent events are detailed in Kersalé et al. (2016).

Continental shelf hydrology

Hydrology over the French continental shelf (summarized by Koutsikopoulos and Le Cann 1996 and Puillat et al. 2004) possesses significant seasonal variability. In winter, the water column is mostly vertically homogeneous in temperature, except for the thermal inversion observed more prominently in vicinity of estuaries. This structure results from the cold fresh waters occupying the upper layers. The seasonal thermocline starts to appear in the western part of the shelf in April and reaches the coast in May

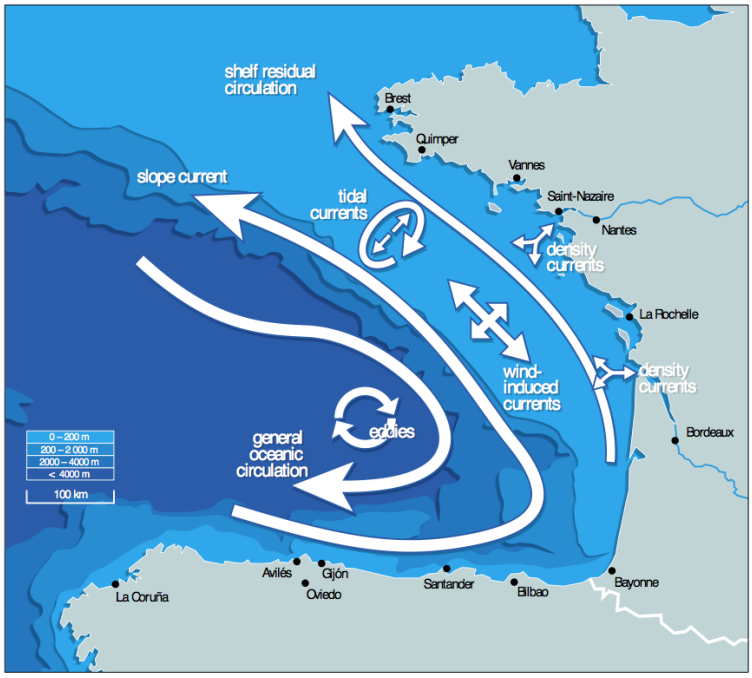

Figure 1.2: Schematic illustration of circulation in the Bay of Biscay, derived from Koutsikopoulos and Le Cann (1996).

(Ker et al., 2016). With the establishment of the thermocline, a cold water mass, called the "Cold Pool ", is isolated below the surface warmer waters. It is located from the south of Brittany to Gironde, centered over 100 m depth, and shows very small variation in temperature throughout the stratified months. In summer and early autumn vertical stratification in temperature is prominent and some seasonal thermal fronts can be observed mainly due to interactions of tidal currents and topography off western Brittany and internal tides across the shelf break. In autumn, thermocline deepens and in the shallow parts the water column is vertically homogeneous.

1.3 Submesoscale Processes

1.3.1 Governing Equations

Before defining fine scales considered in this study, referred as submesoscale, an overview of the main governing equation for ocean motions is given.

According to the conservation of mass, for water with density ρ that moves with the velocity $\mathbf{u}$ (= u$\mathbf{i}$ + v$\mathbf{j}$ + w$\mathbf{k}$), time rate of change of mass in a unit volume dV must be equal to the mass of water that passes through the surface that encloses dV per unit time. Let $\rho\mathbf{u}\cdot\mathbf{n}dA$ be the mass flux out of the unit area dA, then

$$\int \frac{\partial}{\partial t}\rho dV = -\oint \rho\mathbf{u}\cdot\mathbf{n}dA \tag{1.1}$$

and if we apply the divergence theorem to the right hand side,

$$\int \frac{\partial}{\partial t}\rho dV = -\int \nabla\cdot(\rho\mathbf{u})\, dV. \tag{1.2}$$

Since this applies to any arbitrary volume dV,

$$\begin{aligned} \frac{\partial\rho}{\partial t} + \nabla\cdot(\rho\mathbf{u}) &= 0 \\ \frac{\partial\rho}{\partial t} + \mathbf{u}\cdot\nabla\rho + \rho\nabla\cdot\mathbf{u} &= 0 \\ \frac{1}{\rho}\frac{\mathrm{D}\rho}{\mathrm{D}t} + \nabla\cdot\mathbf{u} &= 0. \end{aligned} \tag{1.3}$$

where $\frac{\mathrm{D}}{\mathrm{D}t} = \frac{\partial}{\partial t} + \mathbf{u}\cdot\nabla$ is called the material derivative. Under the assumption that the sea water is incompressible (density of a parcel does not change over time), the first term vanishes. What is left, called the continuity equation, is

$$\nabla\cdot\mathbf{u} = 0. \tag{1.4}$$

Newton's second law for our unit volume dV of water is

$$\frac{\mathrm{D}}{\mathrm{D}t}(\rho \mathbf{u} dV) = \underbrace{\mathbf{F}_P dV}_{\text{Hydrostatic Force}} + \underbrace{\mathbf{F}_F dV}_{\text{Friction}} + \underbrace{\mathbf{F}_B dV}_{\text{Body Forces}} . \tag{1.5}$$

$\mathbf{F}_P$, is the density flux of the hydrostatic force and is expressed as $-\nabla p$ where p is pressure. $\mathbf{F}_F$ are the frictional forces, it is expressed as $\nu\nabla^2\mathbf{u}$, where ν is called the kinematic viscosity. $\mathbf{F}_B$ is the total of the body forces and it consists of gravity and the pseudo-forces, centrifugal and Coriolis, due to the non-inertial frame of reference on the rotating Earth. $\mathbf{F}_B$ is expressed as

$$\mathbf{F}_B = \underbrace{\mathbf{g}_t - \Omega \times (\Omega \times \mathbf{r})}_{\mathbf{g}} - 2\Omega \times \mathbf{u} \tag{1.6}$$

where $\mathbf{g}_t$ is the true gravitational acceleration on earth, Ω is the rotational acceleration of the Earth, and r is the position vector with respect to the center of the Earth. $-\Omega \times (\Omega \times \mathbf{r})$ is the centrifugal force and it is generally omitted or subtracted from $\mathbf{g}_t$ and called the modified gravity, $\mathbf{g}$. $2\Omega \times \mathbf{u}$ is the Coriolis force, and it is expressed as $(2\Omega w \cos\theta - 2\Omega v \sin\theta)\mathbf{i} + 2\Omega u \sin\theta \mathbf{j} - 2\Omega u \cos\theta \mathbf{k}$, where θ is the latitude. The vertical component of the Coriolis force is neglected, and terms with w are omitted (see below, hydrostatic assumption), therefore the remaining coefficient $2\Omega \sin\theta$, denoted f, is called the Coriolis parameter.

The incompressibility and continuity dictate that the left hand side of the equation 1.5 is left with $\frac{\mathrm{D}\mathbf{u}}{\mathrm{D}t}$, then the remaining expression, called the momentum equation, is

$$\frac{\mathrm{D}\mathbf{u}}{\mathrm{D}t} = -\frac{1}{\rho}\nabla p + \nu\nabla^2\mathbf{u} + \mathbf{g} + 2\Omega \times \mathbf{u}. \tag{1.7}$$

If we assume an ocean at rest, the above equation reduces to

$$\frac{1}{\rho}\nabla p = \mathbf{g}. \tag{1.8}$$

Solving for the x, y and z components,

$$\frac{\partial p}{\partial x} = \frac{\partial p}{\partial y} = 0 \text{ and } \frac{\mathrm{d}p}{\mathrm{d}z} = -\rho g. \tag{1.9}$$

which means $p = p(z)$. This leads to $\rho = \rho(z)$, *i.e.* the ocean at rest is horizontally homogeneous (in hydrostatic equilibrium). The above expression is called the hydrostatic equation.

Let's assume the ocean can be defined in two parts; the static equilibrium and the perturbations from this equilibrium, such that

$$p = p_0(z) + p' \text{ and } \rho = \rho_0 + \rho', \tag{1.10}$$

where p_0 is a function of z, but ρ_0 is a constant reference density. When we substitute these in equation 1.7, assuming the perturbations are so small compared to the static state that we can drop primed terms in quadratic form, and keeping in mind the static equilibrium conditions (see equation 1.9), we get

$$\frac{\mathrm{D}\mathbf{u}}{\mathrm{D}t} = -\frac{1}{\rho_0}\nabla p' + \mathbf{b} + \nu\nabla^2\mathbf{u} + 2\Omega \times \mathbf{u}, \tag{1.11}$$

where $\mathbf{b} = \mathbf{g}\frac{\rho'}{\rho_0}$ is called buoyancy. With the continuity condition in equation 1.4, the above set of assumptions are called the Boussinesq approximation.

In the ocean where the vertical acceleration is very small compared to gravitational acceleration, hydrostatic assumption can be applied. This allows us to assume $\frac{\mathrm{D}w}{\mathrm{D}t} = 0$, and omit the diffusivity term in the vertical momentum equation. Then, the momentum equations for the x, y, and z directions are (dropping the primed notation for simplicity)

$$\begin{aligned} \frac{\mathrm{D}u}{\mathrm{D}t} - fv &= -\frac{1}{\rho}\frac{\partial p}{\partial x} + \nu\frac{\partial^2 u}{\partial x^2} \\ \frac{\mathrm{D}v}{\mathrm{D}t} + fu &= -\frac{1}{\rho}\frac{\partial p}{\partial y} + \nu\frac{\partial^2 v}{\partial y^2} \\ \frac{\partial p}{\partial z} &= -\rho g \end{aligned} \tag{1.12}$$

1.3.2 (Submeso-)Scaling

Motions in the ocean are categorized with respect to scales over which they occur. Flows that are basin wide and seasonal to annual in period are called the large scale motions. The subtropical gyre circulation in oceans is an example of large-scale circulation. Mesoscale motions, meso- meaning "middle", are the mid-range (sub-basin) motions, that are one to two orders of magnitude smaller than the large scale, and monthly to seasonal in time. The main mesoscale process is represented by eddies in oceans. Next in this categorization are the submesoscale motions. They are, as we go progressively from large to small by definition, one order of magnitude smaller than the mesoscale and in daily to weekly periods. There are different approaches to define motion scales depending on the physical conditions and what is needed in a certain study. In this section we will describe the submesoscale motion, but to do so we will start from the description of the mesoscale.

Based on the forces at play presented in the previous section, we can evaluate the balance between these forces. Using over which length, velocity, and etc. these forces act, we can produce dimensionless numbers that help us compare the dominance of each term in the momentum equation. Let us start with defining the length, depth, velocity and Coriolis parameter scales as $x, y \sim L$; $z \sim H$; $u, v \sim V$; $\Omega \sim f$, respectively. The two numbers we define to begin with are as follows:

1) The importance of rotational effects are evaluated using the ratio of the advective term to the Coriolis term, called the *Rossby Number, Ro*, such that

$$Ro \sim \frac{\mathbf{u} \cdot \nabla \mathbf{u}}{fu} \sim \frac{V^2}{LfV} \sim \frac{V}{Lf}. \tag{1.13}$$

If $Ro \lesssim 1$, the rotation of the Earth is effective, and *vice versa*.

2) The effect of stratification is described by the *Richardson Number, Ri*, as the ratio of the potential energy converted by disturbing a stratified fluid of density difference $\Delta\rho$ a vertical distance of H to the kinetic energy needed for this disturbance, such that

$$Ri \sim \frac{\Delta\rho g H}{1/2\rho_0 V^2} \sim \frac{N^2 H^2}{V^2} \tag{1.14}$$

where $N = \sqrt{\frac{\partial b}{\partial z}}$ is the buoyancy frequency. If $Ri \gtrsim 1$, there is not enough kinetic energy to disturb the stratification, meaning the stratification restricts the fluid motion, and *vice versa*.

A key number to define length in the ocean is the *Rossby deformation radius, R*. First baroclinic Rossby deformation radius is $R = \frac{NH}{f_0}$. By definition, motions at the length scale of R are defined as mesoscale motions. For the open ocean this length can vary from $O(10)$ to $O(100)$ km (Chelton et al., 1998). With this definition, places the submesoscale at $L \sim O(1)$ to $O(10)$ km.

The majority of the dynamics in the ocean, occur when $Ro \ll 1$ and $Ri \gg 1$, which includes both large and mesoscales. Thomas et al. (2008) define submesoscale as occurring where $Ro \sim O(1)$ and $Ri \sim O(1)$. Typically, vertical length scale of submesoscale motions in the upper ocean is the mixed layer depth, h_{ml}. When the above conditions are applied and N_{ml}, the mixed layer buoyancy frequency, is inserted, we end up with a length scale, L_{ml}, for the submesoscale motion, such that $L_{ml} = N_{ml} h_{ml}/f$. For a mid-latitude mixed layer with $f = 10^{-4} s^{-1}, h_{ml} = 100m, N_{ml} = 10^{-3} s^{-1}$, submesoscale length scale L_{ml} is 1 km.

1.3.3 Submesoscale dynamics

In the upper ocean, mechanisms that generate the situations of submesoscale dynamics mentioned above are mostly studied under two main topics, frontogenesis and instabilities.

Frontogenesis

Frontogenesis is the process of intensification of horizontal gradients at a front. When a horizontal density gradient is disrupted (*e.g.*, through instability processes and their associated meanders) by local lateral straining field, a secondary ageostrophic circulation is generated in the cross-front plane. The secondary circulation tries to tilt the isopycnals back to geostrophic balance, and by doing so vertical velocities arise. Towards the surface as the vertical velocity, w goes to zero, $\partial w/\partial z$ increases. The horizontal ageostrophic divergence compensates this, and instead lateral straining increases further. Submesoscale frontogenesis is thus created in regions of large Ro and small Ri (Thomas et al., 2008).

Instabilities

A horizontal gradient in a weakly stratified upper ocean layer that sits on top of a stratified deeper ocean (i.e. in the mixed layer) that is in a geostrophically adjusted state may go baroclinically unstable and undergo rapid restratification (light water further pushes over the denser side of the front). The rapid nature of this mechanism distinguishes it from mesoscale instabilities (Thomas et al., 2008; Boccaletti et al., 2007). These instabilities are termed "mixed-layer instabilities "and correspond to conditions where Ro and $Ri \sim 1$, the time scale T, is $\sim f^{-1}$, which is significantly faster than mesoscale instabilities (Boccaletti et al., 2007).

In the presence of a forcing that acts to reduce buoyancy and/or increase down-front wind stress, other variants of instability are also generated. In the case of Haine and Marshall (1998), differential cooling of a front with a baroclinic jet results in production of baroclinic waves along the jet that are similar in dynamics to baroclinic instability. Down-front winds generate an Ekman transfer that is from the denser to the lighter side of the front, destabilizing the front thus in turn gives way to further geostrophic adjustment (Boccaletti et al., 2007; Thomas et al., 2008; Molemaker et al., 2010).

Up to this point all descriptions and examples are given for open and/or theoretical ocean cases. In the coastal ocean, which is the main region of interest of the present study, few studies have been dedicated to submesoscale dynamics. Hetland (2016) studies conditions for formation of instabilities in river plumes using both idealized and realistic simulations of the Mississippi - Atchafalaya plume. Capet et al. (2008a) investigated, with a high resolution numerical model, the submesoscale activity and its relation to seasonal drivers in the Argentinian shelf.

1.4 Objectives

The spatial scales of ocean dynamics over continental shelves vary strongly depending on the region considered. These dynamics at different scales have an impact on the biological activity in addition to the large scale forcings (*e.g.* tides, winds, rivers). In this context, the present study proposes to explore the development mechanisms of (sub)mesoscale structures ($\sim$ 1-100 km) in the Bay of Biscay with a specific focus on river plume boundaries from the main French rivers in the Bay of Biscay (Gironde and Loire). This project is based on the use of satellite observations of sea surface temperature and ocean color, *in situ* observations, and primitive equation numerical simulations with a high degree of realism.

Objectives of this thesis study are:

- to identify and to characterize (sub)mesoscale activity, its intensity and variability over the continental shelf in the Bay of Biscay with a focus at the edges of main river plumes (via remotely sensed observations and numerical modeling, providing synoptic views),
- to understand the physical driving mechanisms of the observed structures,
- to assess the role of instabilities in this frontal dynamics (in vicinity of the river plumes) using high resolution modeling.

Plan

In Chapter 2, submesoscale activity in the Bay of Biscay is explored using observations. A long term remotely sensed Sea Surface Temperature (SST) dataset is presented. A novel front detection method, the singularity exponents, is introduced and the statistical approach of calculating front occurrence probability is described. Resulting frontal activity distributions together with model simulations of the study region are discussed and three main occurrences of fronts are identified according to their driving mechanisms.

In Chapter 3, a high resolution realistic modeling study of the Bay of Biscay is presented. The MARS3D model description, the Bay of Biscay configuration set-up for this study, and the model skill assessment are given. A flow decomposition separating the large, meso-, and submesoscale components is defined. Results of the modeling study are presented based on the exploration of the occurrence of baroclinic instability as the dominant mechanism for submesoscale dynamics. Submesoscale component of the vertical buoyancy flux and its relation to conversion of available potential energy to eddy kinetic energy are described. The seasonality and the spatial variability of the submesoscale dynamics and their possible drivers are discussed.

In Chapter 4, a summary of the efforts and the main outcomes of the study are given in the conclusion. Lastly, in perspectives, implications that the outcomes of this study may have and the open questions it has arisen are addressed.

Chapter 2

Spatial and Seasonal Distributions of Frontal Activity over the French Continental Shelf in the Bay of Biscay

---

Contents

2.1 Introduction 16

2.2 Data and methods 19

2.2.1 Remotely sensed Sea Surface Temperature 19

2.2.2 Numerical Experiments 20

2.2.3 Singularity Exponents 25

2.3 Observed Frontal Activity 29

2.3.1 Variability of Sea Surface Temperature 29

2.3.2 Spatio-temporal variability of frontal activity 32

2.4 Modeled Frontal Activity 38

2.4.1 Spatio-temporal variability of frontal activity 38

2.5 Discussion 45

2.5.1 Freshwater fronts 45

2.5.2 Tidal fronts 51
2.5.3 Shelf break front 54
2.6 Conclusion 57
2.7 Acknowledgments 58

This work has been published as an article in Continental Shelf Research (Yelekçi et al., 2017).

2.1 Introduction

Since oceans are observed from space, the two-dimensional depiction of the ocean surface circulation is becoming more detailed but also more complex. One of the key dynamical features is fronts (D'Asaro et al., 2011; Ferrari, 2011). These regions, where horizontal gradients of physical or biogeochemical properties are locally increased, play major roles in the exchanges (*e.g.* heat, gases) between the subsurface and the atmosphere. In particular, they tend to separate flow regions with distinct water masses, albeit with some exchanges across, *e.g.* due to even finer scale processes. These transition zones have typical across-scales, termed submesoscale, in the range from infrakilometric to ∼10 km.

Several past studies explored the role of fronts in terms of the generated vertical velocities (*e.g.* Taylor and Ferrari, 2010). The effect of submesoscale velocities on biological production is a subject of great interest (*e.g.* Owen, 1981; McGillicuddy et al., 1998; Oschlies and Garçon, 1998; Lévy et al., 2001; McGillicuddy et al., 2007). Due to this potential importance of frontal structures, together with the possibility to observe them via remote sensing, fronts have been widely mapped globally and also in many shelf regions. Submesoscale effects are believed to be very important as shown in the first

global remote sensing survey of fronts in Large Marine Ecosystems (Belkin et al., 2009). Many studies have been dedicated to the description of the frontal dynamics of coastal regions, such as in European shelf seas (Simpson and Hunter, 1974; Simpson et al., 1978; Bowers and Simpson, 1987; Simpson et al., 1981), over the US Southeastern Continental Shelf (Oey, 1986), along the Northeast US coast (Ullman and Cornillon, 1999), around South America (Acha et al., 2004), off North-West Iberia (Otero et al., 2009), east China (Hickox et al., 2000; Huang et al., 2010), and in Canadian coastal waters (Cyr and Larouche, 2014). In light of these previous observations, the main determinants of fronts in coastal seas are known to be combinations of tides, bathymetry, river runoffs, and wind.

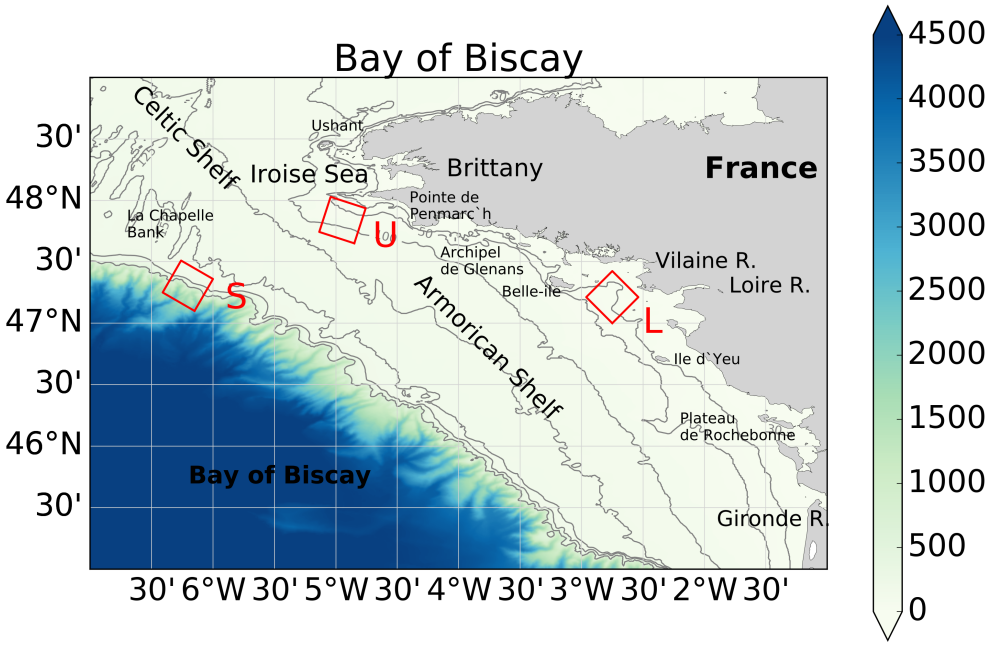

Figure 2.1: Map of the Bay of Biscay north of 45°N with bathymetry (30, 50, 100, 125, 150, 200 and 500 m isobaths are additionally drawn in gray), showing important geographical features and the locations of the boxes over which time-series analyses are performed (red).

The present study aims at improving the characterization and description of frontal

activity in the Bay of Biscay (Figure 2.1), using a recent image processing approach dedicated to turbulent systems. Analyses are focused on the seasonal evolution of frontal activity. Some frontal features in the Bay of Biscay have previously been considered most often in relation with plankton dynamics as in the Ushant front (Schultes et al., 2013), across the continental slope (Fernández et al., 1993), and over the Aquitaine shelf (Albaina and Irigoien, 2004). However, the different turbulence regimes in the Bay of Biscay shelf remain under-documented except for the tidally driven fronts described mainly in the Irish and Celtic Seas (Simpson and Hunter, 1974; Simpson et al., 1978, 1981). The Bay of Biscay is arguably an interesting natural laboratory to investigate submesoscale frontal dynamics, where many different processes take place that contribute to the maintenance of frontal activity. Baroclinic tides generated and dissipated over the continental slope and shelf break are responsible for intense mixing that produces large density contrasts. Stirring of these contrasts due to internal tide breaking frequently leads to submesoscale fronts. Spatial variations of frictional forces acting on the barotropic tide can modulate this activity spatially and temporally. This is, for instance, a source of submesoscale in the Ushant front region and other parts of the mid-shelf. River plumes are responsible for major buoyancy contrasts with freshwater input, in particular from Loire and Gironde, but their impact on submesoscale activity is not known.

The main objective of this study is to describe the frontal activity over the Bay of Biscay shelf exploring the potential of the Singularity Exponent Analysis to characterize turbulent systems. To this end, we use remotely sensed Sea Surface Temperature (SST) images for the 11 year long period from 2003 to 2013. Furthermore, their analysis is complemented with coastal model experiments to improve the description and the dynamical understanding of observed features. These datasets, which have high spatial resolution ($\sim$1 km for observation and 2.5 km for model), allow us to describe the spatial

and temporal evolution of frontal activity at the relevant meso- and submesoscales scales.

After describing the data and methods used to analyze frontal occurrence (Section 2), the variability of the SST is briefly described as the background physical setting and the spatial and the temporal variability of frontal activity over 11 years from observations (Section 3), and over 8 years from model experiments (Section 4). Finally, a discussion on the processes explaining these features is presented (Section 5).

2.2 Data and methods

2.2.1 Remotely sensed Sea Surface Temperature

A dataset of nighttime SST (short-wave at 4μm) remotely sensed by MODIS (Moderate Resolution Imaging Spectroradiometer) onboard Aqua and Terra satellites has been investigated. Level 2 ungridded SST products are downloaded from the PO.DAAC (Physical Oceanography Distributed Active Archive Center) data service provided by NASA. This dataset has $\sim$1 km spatial resolution. Daily products are considered. The time period extends over 11 years from 2003 to 2013. The area enclosed by latitudes 45°N to 49°N and longitudes 0°W to 7°W is defined as the study region. Cloud contaminated pixels on the images are masked using the flags provided with the Level 2 products. Images that are more than 90% cloud covered, which constitute $\sim$30% of the dataset for our region, are discarded from the analyses. The final database is rich of 3124 images. This number is considered adequate to extract the seasonal and spatial information presented.

2.2.2 Numerical Experiments

2.2.2.1 Model configuration

The numerical experiments considered are part of the coastal operational oceanography project PREVIMER (Dumas et al. (2014), http://www.previmer.org). The model outputs considered are based on the MARS3D (Model for Applications at Regional Scale, Lazure and Dumas (2008); Duhaut et al. (2008)) primitive equation model in a regional configuration extending from 18°W to 9.5°E and from 41°N to 55°N with 40 σ vertical levels (similar to the configuration described in (Berger et al., 2014)). The spatial resolution is 2.5 km. The tracer advection uses the upwind 5^{th} order and multidimensional MACHO3D scheme (Leonard et al., 1996). Momentum advection uses the 3^{rd} order QUICK. Vertical advection uses a 5^{th} order COMPACT scheme and vertical turbulence is based on a Generalized Length Scale formulation of the $k-\varepsilon$ scheme (Umlauf and Burchard, 2005). Thus, diffusion arises from truncation errors of the advection operators for tracers and momentum. Despite our high order advection schemes we do not expect to resolve submesoscale flow features with scales finer than $\sim$ 7-10 Δx, which is $\sim$ 20 km (Soufflet et al., 2016).

Open boundary conditions originate from PSY2V4 Mercator-Ocean simulations (http://www.mercator-ocean.fr) with a 1/12° spatial resolution and are located from the area investigated. These fields are provided with a daily temporal resolution. Boundary conditions used for tides are the FES 2004 harmonical components (Lyard et al., 2006). Atmospheric forcings are from Météo-France ARPEGE High Resolution (Déqué et al. 1994; 0.1° spatial resolution and hourly fields) and AROME (Seity et al. 2011; 0.025° spatial resolution and hourly fields) models. The AROME model with a limited geographical extent is used for a limited domain close to the coast and merged with ARPEGE fields for open ocean.

Modeled outputs are three-days' averages to remove tidal frequencies using a Demerliac filter (Demerliac, 1973), and are available from 2006 in real time as an operational forecast (http://www.previmer.org).

2.2.2.2 Model skill assessment

Before considering these modeled fields to explore the frontal dynamics, simulations have been evaluated against available observations (in situ and remotely sensed).

As a first overview, modeled SST has been compared with remotely sensed observations (SEVIRI Sea Surface Temperature remotely sensed data - METEOSAT SST provided by OSI-SAF belonging to EUMETSAT; Le Borgne et al. 2011). Instead of the MODIS dataset used for front detection, SST observations from SEVIRI are used for the model skill assessment, because they are available in hourly temporal resolution, and are compared to the unfiltered hourly modeled SST fields. Figure 2.2a shows the mean SST bias over the modeled domain. Based on the year 2010, the bias is generally lower than 1 °C with a colder modeled SST in the English Channel and along the coast in the south and southeastern part of the Bay of Biscay. In the open ocean, north of 46°N, the model tends to slightly overestimate the SST. The temporal evolution of the spatially averaged bias is represented in Figure 2.2b. This evolution shows a good agreement between simulation and observation in terms of average and spatial standard deviation. The differences observed are associated to very short periods. Finally, these biases remain very limited and confirm the ability of the model to reproduce the main features of the SST variability.

The evaluation of the vertical structure is important to consider as it will be used for the analysis of the fronts. In the Bay of Biscay, based on voluntary vessels, the RECOPESCA project provides observations of the fishery activity (effort and catches) and the environment (temperature and salinity) (Leblond et al., 2010; Charria et al.,

2014; Lamouroux et al., 2016). Dedicated sensors are implemented on the fishing gears and collect vertical hydrological profiles. This unique profile database in the Bay of Biscay over the continental shelf is used to evaluate the modeled vertical structure. In Figure 2.3, the distribution of the misfit between modeled and observed temperature and salinity shows a larger spread in the intermediate layers (20-40 m depth). This feature results from the fact that small errors in the position/sharpness of the thermocline and halocline produce large but localized errors in terms of temperature and salinity. However, most of the differences ranges below 2 °C in temperature and 1 psu in salinity. In the surface and bottom layers, very few points have a misfit exceeding 2 °C and 1 psu. The distributions also highlight a warm (around 0.9 °C in surface layers and around 0.38 °C in deeper layers) and salty (around 0.35 - 0.37 psu) bias over the water column. These comparisons with in situ profiles provide a more detailed analysis of model performance and confirm the coherence of the modeled vertical structure.

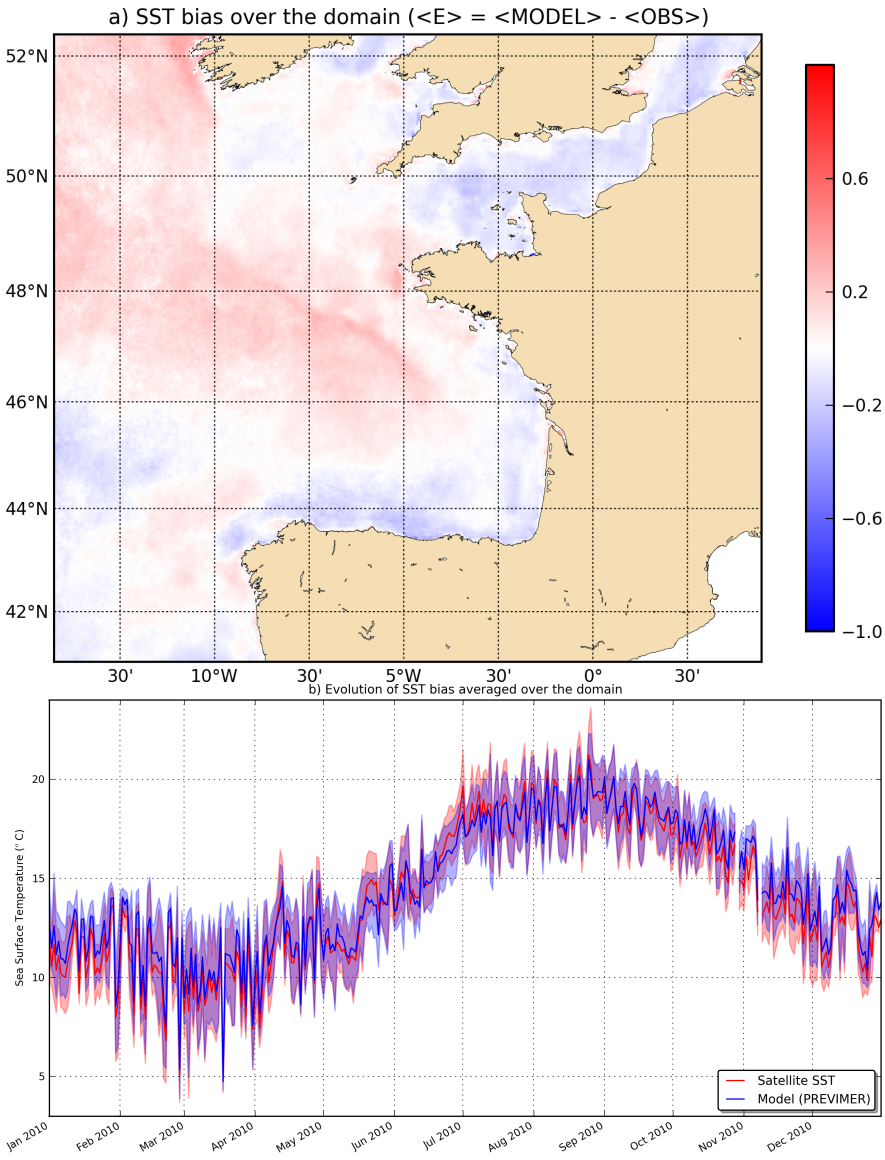

Figure 2.2: Comparison between observed (SEVIRI satellite SST) and modeled (PREVIMER) sea surface temperature. a) Mean bias between model and observations for the year 2010. b) Temporal evolution of the SST bias during 2010. The shape of the curves represents the spatial standard deviation.

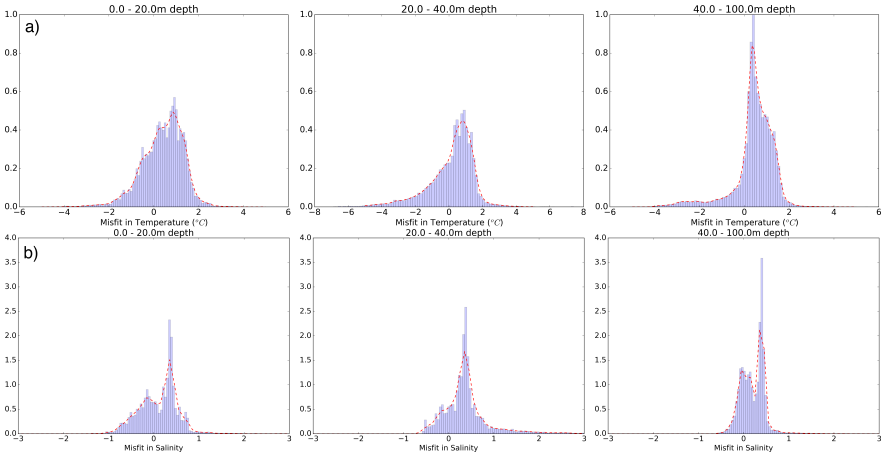

Figure 2.3: Normalized distribution of the misfit (modeled - observed) in a) temperature and b) salinity from RECOPESCA in situ profiles (only for profiles deeper than 100 m) for three vertical layers: 0-20 m depth (left), 20-40 m depth (middle), and 40-100 m depth (right).

2.2.3 Singularity Exponents

The frontal structures observed in satellite images are regions delimited by sharp variations of the gradient's norms. The detection of these sharp variations can be done according to different methods in image processing.

The present study is based on the use of singularity exponents. Singularity exponent analysis is the process of calculating a measure of the degree of regularity or irregularity of a function at each point in a domain (Turiel et al., 2008b). The notion of localized singularity exponent is a generalization, in a microcanonical setting, of the classical multifractal formalism as exposed in Arneodo et al. (1998). Singularity Exponents (SE) are dimensionless quantities evaluated at each point signal (here the SST on the Bay of Biscay represents this signal). The theory behind this indicator is explained in detail in Turiel et al. (2008b), where they improved the approach to reach a finer spatial resolution.

Following the main lines from Maji et al. (2013), a signal s is multiscale in a microcanonical sense, if a functional $(T_r s(x))$, representing a local dissipation of energy in a ball of radius r and centered on x, is assumed to be satisfying the equation:

$$T_r s(x) = \alpha(x) r^{h(x)} + o(r^{h(x)})(r \to 0) \tag{2.1}$$

where $\alpha(x)$ is an amplitude coefficient and $h(x)$ is the exponent called a singularity exponent or local predictability exponent of the point x. This local dissipation of energy $(T_r s(x))$ is expressed as the gradient's norms of the signal integrated on a ball of radius r centered on x (Yahia et al., 2010; Sudre et al., 2015).

The algorithm to compute the singularity exponents $h(x)$ (Turiel et al., 2006; Pont et al., 2011), solves the equation:

$$h(x) = \frac{log(\tau_\psi s(x, r_0))/\langle \tau_\psi s(., r_0) \rangle}{log(r_0)} + o(\frac{1}{log(r_0)}) \tag{2.2}$$

where $\tau_\psi s(x, r_0)$ is a wavelet decomposition of the signal $s(x)$, $\langle \tau_\psi s(., r_0) \rangle$ is the average of the wavelet projection over the whole signal, $o(\frac{1}{log(r_0)})$ is a diminishing quantity, and r_0 is the minimum scale. If the signal s is an image of size $M \times N$, then we choose $r_0 = 1/\sqrt{M \times N}$.

Following previous studies, this image processing method given by the notion of singularity exponents for edge detection is the most adapted and efficient in the case of natural and turbulent complex signals (Yahia et al., 2010; Maji and Yahia, 2014; Turiel et al., 2008b; Sudre et al., 2015), compared with other classical approaches in image processing (Maji et al., 2013).

Images have been processed using the software developed by H. Yahia (Yahia et al., 2010). The resulting fields are normalized by the image size such that the parameter SE varies between -0.6 and 2. Figure 2.4 shows an example of a SST image and singularity exponent analysis applied to that image. Negative values of SE indicate sharp variations of the gradient at all scales, *i.e.* stronger frontal activity, while positive values denote continuous signals *i.e.* weak frontal activity (Turiel et al., 2008a). The major advantage of using SE instead of calculating the gradient of a signal is that it conveys the information of the scale of the signal's irregularity SE allow us to have an nondimensional classification of all fronts in a set of images, with appropriate multiscale characteristics of each front.

Front detection is performed based on the distribution of the SE. It is considered that a front is located where the largest irregularity in the SST field occurs, *i.e.* where the SE is the lowest. SE fields are analyzed in a pixel by pixel approach. A pixel is considered frontal, if $-0.2 \geq SE \geq -0.6$ for that pixel (Figure 2.4b). In Figure 2.4c, it is seen how the SE correlates to the gradient of the SST and the pixels that fall into

the frontal pixel range. With a gradient based detection method lower gradient pixels would not have been selected, whereas with the singularity exponent analysis we can detect fronts based on the irregularity of the SST around a pixel, irrespective of the local absolute gradient value there.

Great care was taken to prevent false positive detection of fronts at the edges of the SST maps, at the ocean-land transition or at the boundaries of individual cloud masks (note that issues at the latter would be less problematic because clouds are not stationary so incorrect treatment may not significantly alter the spatial patterns of frontal statistics). To this end, land and cloud masks were extended by 3 pixels (see zoom in Figure 2.4b). This restriction gives us confidence in the reality of the nearshore frontal patterns observed in Figure 2.6.

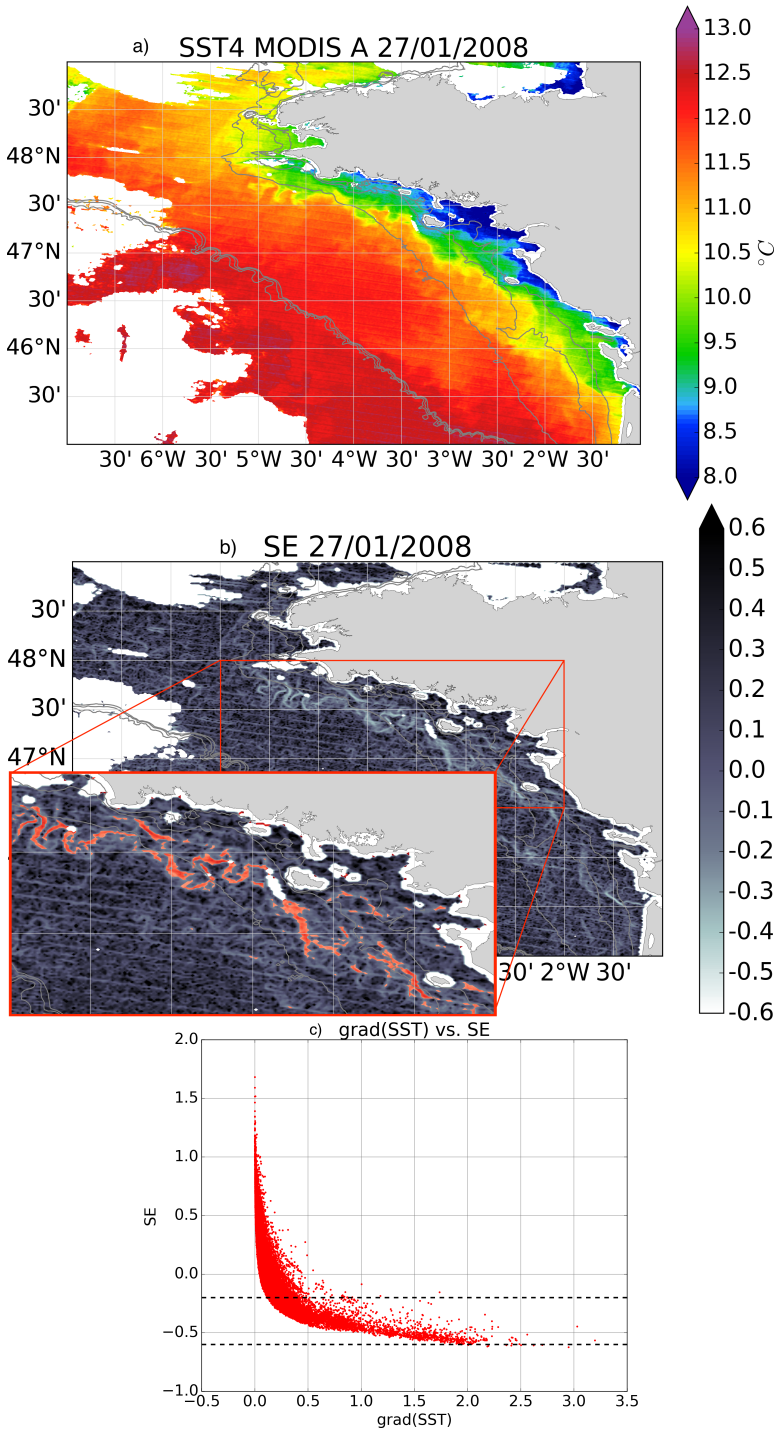

Figure 2.4: An example of a) remotely sensed sea surface temperature, b) the corresponding singularity exponent field (zoom: selected frontal pixels in red), c) gradient magnitude of the remotely sensed sea surface temperature versus the corresponding singularity exponent (area between the dashed lines is the range of frontal pixel selection) on 27/01/2008 (isolines represent the 30, 50, 100, 200, 250 and 500 m depths).

2.3 Observed Frontal Activity

2.3.1 Variability of Sea Surface Temperature

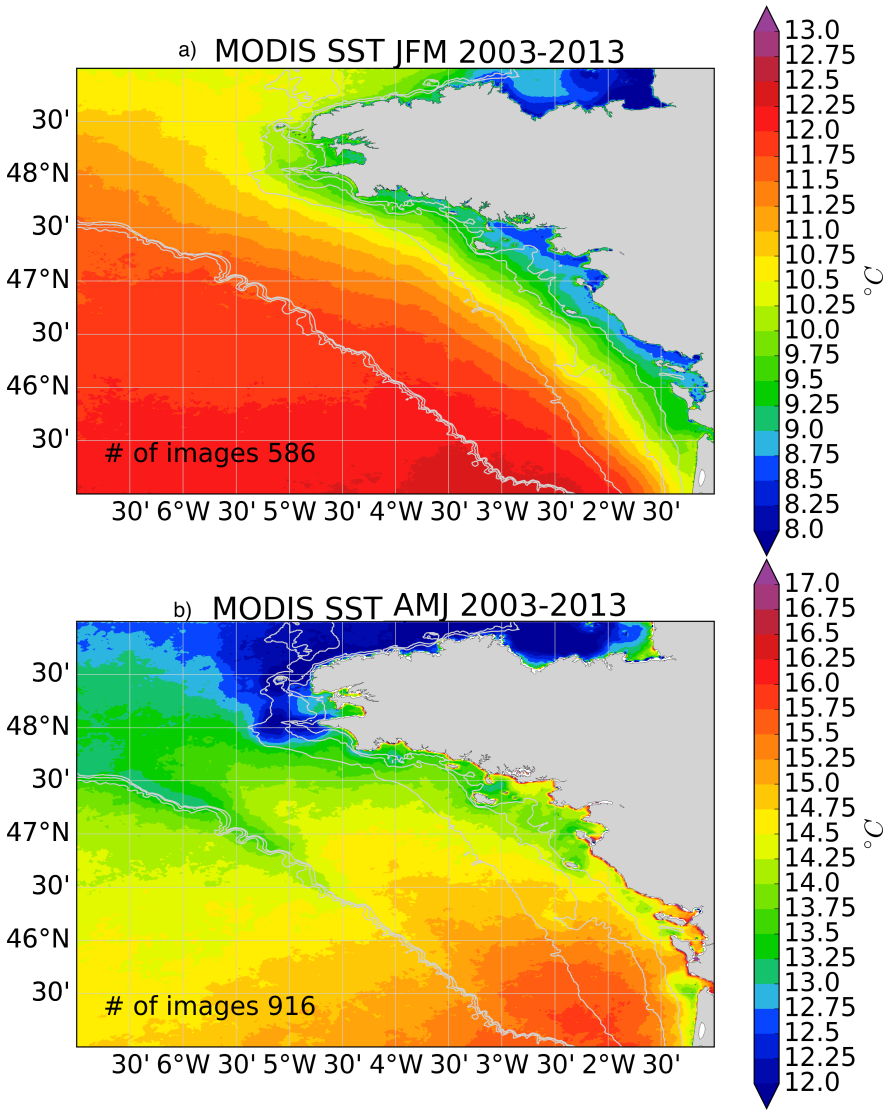

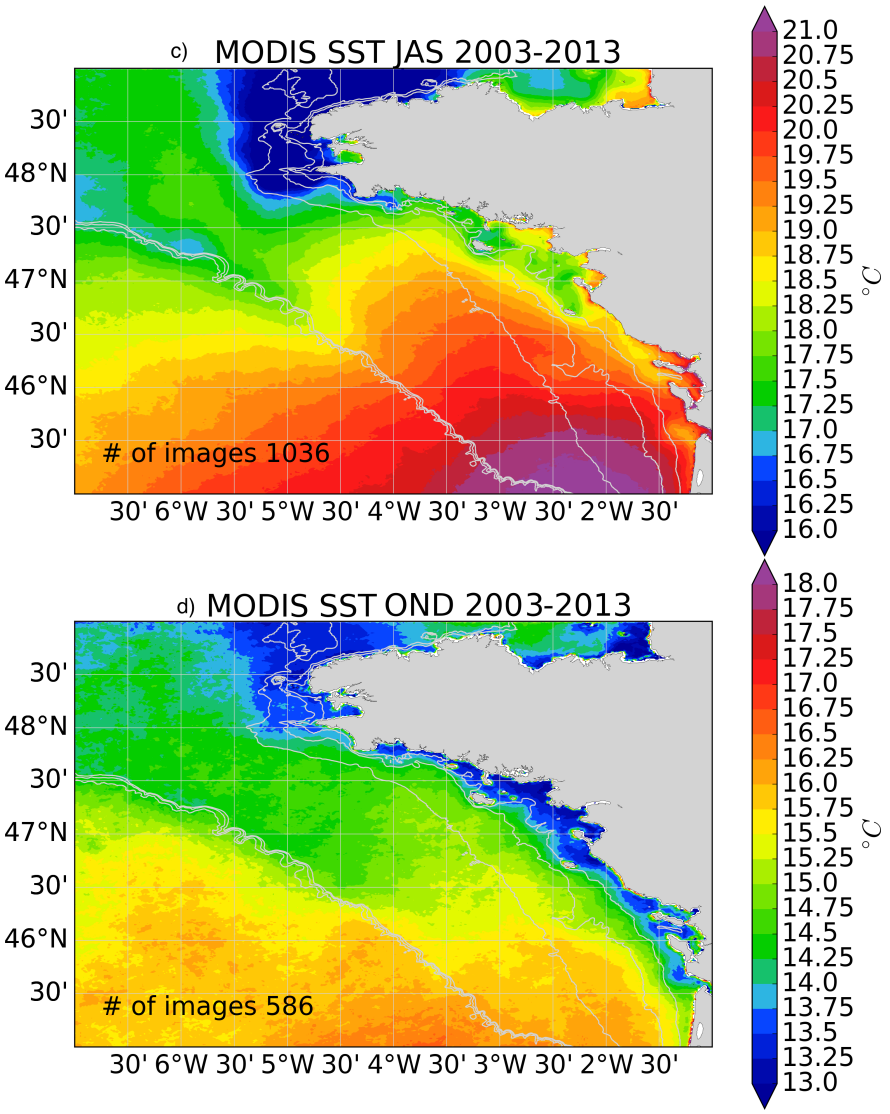

Figure 2.5: Seasonally averaged remotely sensed sea surface temperature from 2003 to 2013 over a) winter (January, February, March), b) spring (April, May, June), c) summer (July, August, September), and d) autumn (October, November, December). Colorscales differ for each panel, but range by schematically 5 °C.

The seasonal distributions of Sea Surface Temperature (SST) are presented to give an overview of the background physical environment of our study area and the natural variability observed in the satellite SST dataset. Figure 2.5 shows the SST over the Bay of Biscay from 2003 to 2013, averaged over each season. During all seasons, over the offshore oceanic part a large scale north - south temperature gradient exists with warmer waters in the south.

Over the shelf, a more complex seasonal cycle is observed. In winter, a marked temperature gradient (up to 0.5 °C km^{-1} amplitude) primarily oriented in the cross-shore direction with a minimal along-shore component is observed over the shelf. Inshore of the 100 m isobath, north of the Loire and Gironde estuaries, average SST is ≤ 10 °C representing the coldest regions in the studied area. In spring is the transition period. The north - south temperature difference continuously increases and the SST gradient orientation over the shelf becomes partly along-shelf direction. Close to the coast, average SST increases to 15 - 18 °C. Signature of the tidal mixing is observed at the Ushant region with colder waters with average temperatures less than 12 °C the front and the coast. A similar, but weaker signal of the internal tidal mixing also forms along the shelf break around the 200 m isobath. In summer, the SST gradient is mainly in the along-shore direction over the shelf with a warm pool in the south-eastern part of the Bay of Biscay with average temperature exceeding 20 °C. During this season, a strong signal induced by tidal mixing is also observed in the Ushant region off Brittany with average SST ≤ 16 °C on the cold side of the front. Similar cold waters are also observed along the coast south of Brittany. Local minima in temperature are also observed near the shelf break. Note, at the shelf break, the trough-like pattern visible in SST isocontours between 46°N and 47°N whose amplitude progressively reduces southward. Autumn is again a transition season. The SST gradient orientation reverses back to the cross-shore direction, especially in the vicinity of major estuaries. Surface cooling

begins in this season, decreasing the average SST to 12 - 14 °C inshore of the 30 m isobath. Stratification reduction weakens the tidal mixing signal observed in summer. South of 47°N approximately between the 50 and 150 m isobaths, the warmer waters with temperature $\sim$ 15 - 16 °C appear to be intruding towards the north.

Based on these general identified features, the investigations are focused on the frontal activity that accompanies these observed mean field patterns.

2.3.2 Spatio-temporal variability of frontal activity

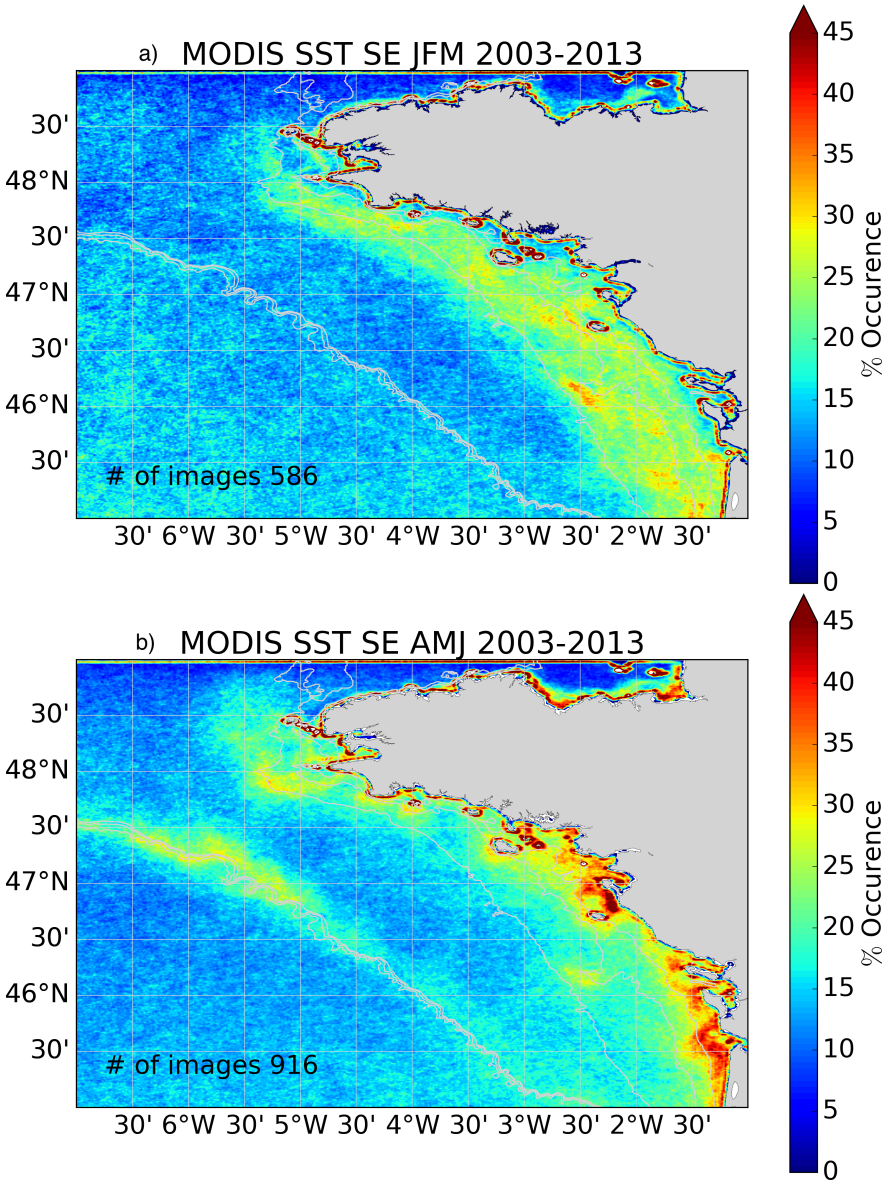
a) MODIS SST SE JFM 2003-2013
30'
48°N
30'
47°N
30'
46°N
30'
# of images 586
30' 6°W 30' 5°W 30' 4°W 30' 3°W 30' 2°W 30'
45
40
35
30
25
20
15
10
5
0
% Occurence
b) MODIS SST SE AMJ 2003-2013
30'
48°N
30'
47°N
30'
46°N
30'
# of images 916
30' 6°W 30' 5°W 30' 4°W 30' 3°W 30' 2°W 30'
45
40
35
30
25
20
15
10
5
0
% Occurence

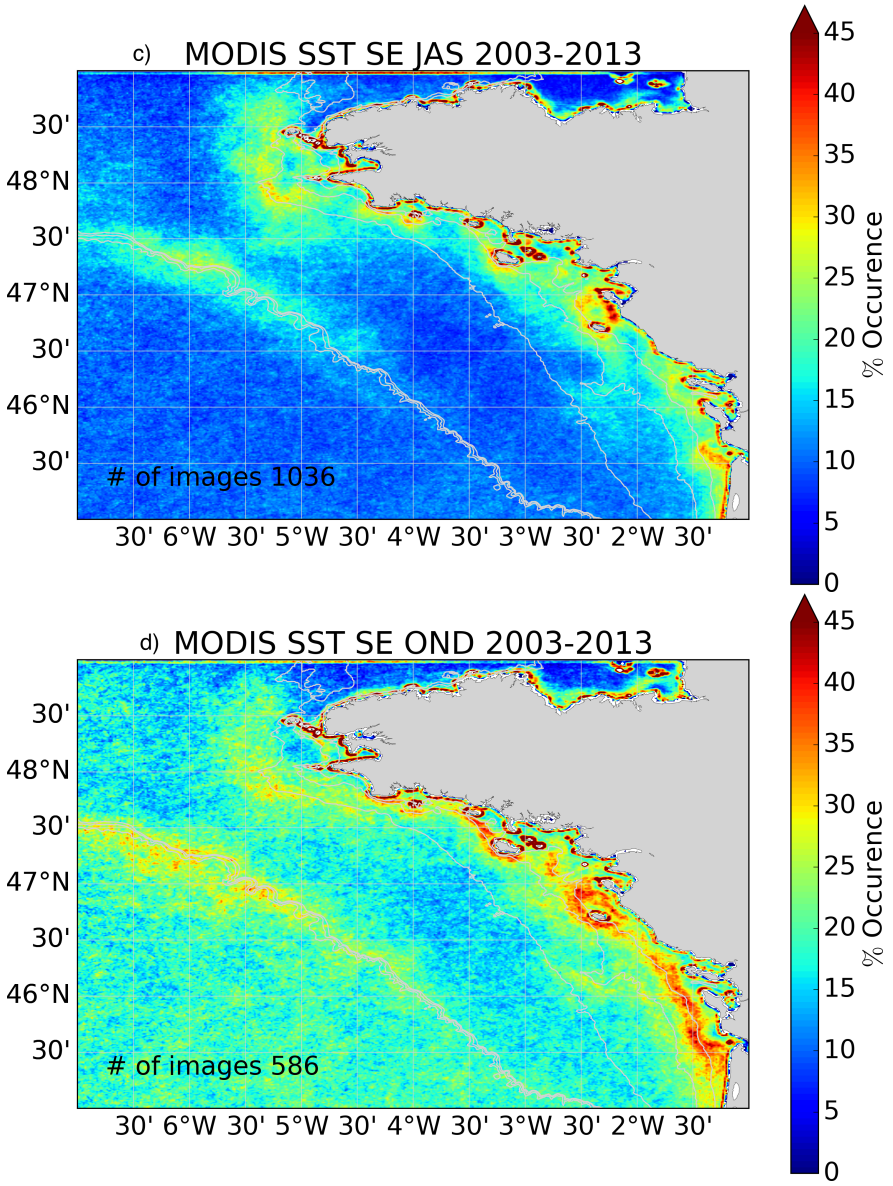

Figure 2.6: Front occurrence frequency of the MODIS remotely sensed sea surface temperature expressed in percentage of number of times a pixel is cloud-free from 2003 to 2013 in a) winter (January, February, March), b) spring (April, May, June), c) summer (July, August, September), and d) autumn (October, November, December) expressed in percentage of number of times a pixel is cloud-free.

The spatial distribution of frontal activity is investigated in terms of the occurrence frequency of fronts during each season. The front occurrence frequency on a pixel is defined as the percentage of the times the pixel is a *frontal pixel* (based on the singularity exponent analysis, see Section 2) out of all times that pixel is cloud-free.

In winter (Figure 2.6a), the majority of the fronts occur in an along-shore band inshore of the 100 m isobath, with the occurrence frequency ranging between 20% and 45%. Within this band, the frequency of front occurrence is locally larger, reaching 40% to 45%, at the offshore edges of bathymetric features, namely, southwest of Archipel des Glénans, Belle-île and Ile d'Yeu islands, and close to Plateau de Rochebonne (a shoal in the Southern part of the Armorican shelf, see Figure 2.1). Significant patches of frontal occurrences with values between 35% to 45% are observed in the vicinity of the Loire and Gironde plumes, approximately along the 50 m depth in front of these estuaries. Over the shelf, offshore of the 100 m depth up to the shelf break between the Gironde estuary and Penmarc'h ($\sim$ 45.5°N-48°N), the front occurrence frequency is mainly $\leq$ 20%. In summary, the winter frontal activity in the region is dominated by a mid-shelf frontal region between the 50 and 100 m isobaths.

In spring (Figure 2.6b), frontal zones are most prominently observed along the coast inshore of the 50 m depth, around the Loire-Vilaine and Gironde estuaries at 46.7°N-47.5°N and 45°N-46.5°N, respectively. The occurrence frequency of fronts just at the estuary mouths of Loire and Gironde is highest with values reaching 50%. Patches of front occurrences observed at the offshore edges of islands are weaker in frequency compared to winter with values $\sim$30%. In the Iroise Sea, along the vicinity of the 100 m depth between 47.7°N and 48°N, the Ushant front is observed as a patch with a significant frequency of occurrence ranging between 30% and 40%. At the shelf break, in the vicinity of the 200 m depth at 47°N - 47.5°N, an elongated patch of front occurrence is observed with frequencies between 25% and 40%. As in winter, front occurrence is

lower and less than 20% offshore of the 100 m isobath.

In summer (Figure 2.6c), the Ushant front, ∼10 km wide patch observed in the Iroise Sea in the vicinity of the 100 m depth between 47.5°N and 49°N, is the most extensive frontal occurrence. Fronts observed in this region have an occurrence frequency reaching 40%. Inshore of the Ushant region, in the vicinity of 50 m depth a second patch of fronts is observed with the occurrence frequency between 20% and 30%. Along the coast, the hot-spots of front occurrences are to the south of the Vilaine, Loire, and Gironde rivers near 47.3°N, 46.8°N, and 45.5°N, respectively, with frequencies 30% to 45%. Significant front occurrences are observed off the coasts of Pointe de Penmarc'h, Archipel des Glénans, Belle-île, and Ile d'Yeu with frequencies ranging between 25% and 35%. Along the shelf break, in the vicinity of the 200 m depth between 47°N - 47.5°N, the patches of large front occurrences are spatially smaller compared to spring and less frequent reaching only 30%. Overall, summer is the season with lowest frontal occurrence with values as low as 5 - 10 % over a large fraction of the outer shelf. During this season, the frontal activity is confined along the coast, in the Iroise sea, and over the shelf break.

In Autumn (Figure 2.6d), the front patches are observed to be spatially more extended compared to the other seasons. In the vicinity of the 100 m depth between 47.7°N and 48.7°N, the Ushant front is observed to occur as a ∼40 km wide patch with an occurrence frequency of 25% to 40%. Inshore of this region, a second band of large values is present near shore, with a frequency ranging between 25% and 35%. North of the Gironde estuary at 45.5°N up to Penmarc'h point at 47.7°N, a very intense ∼10 km wide band of fronts with frequencies 30% to 50% occurs along the vicinity of the 30 m depth. Inshore of this band one prominent patch of fronts occurs with similar frequency south of the Loire estuary at 46.8°N. The patch of fronts observed at the shelf break along the 200 m depth between 46.5°N and 47.5°N is larger and more prominent in this

season compared to summer and spring, and its frequency ranges between 30% to 45%. An increased occurrence frequency should also be noted over the shelf between the 100 to 200 m depths and also offshore of the shelf, where the frontal activity is minimum in all other seasons.

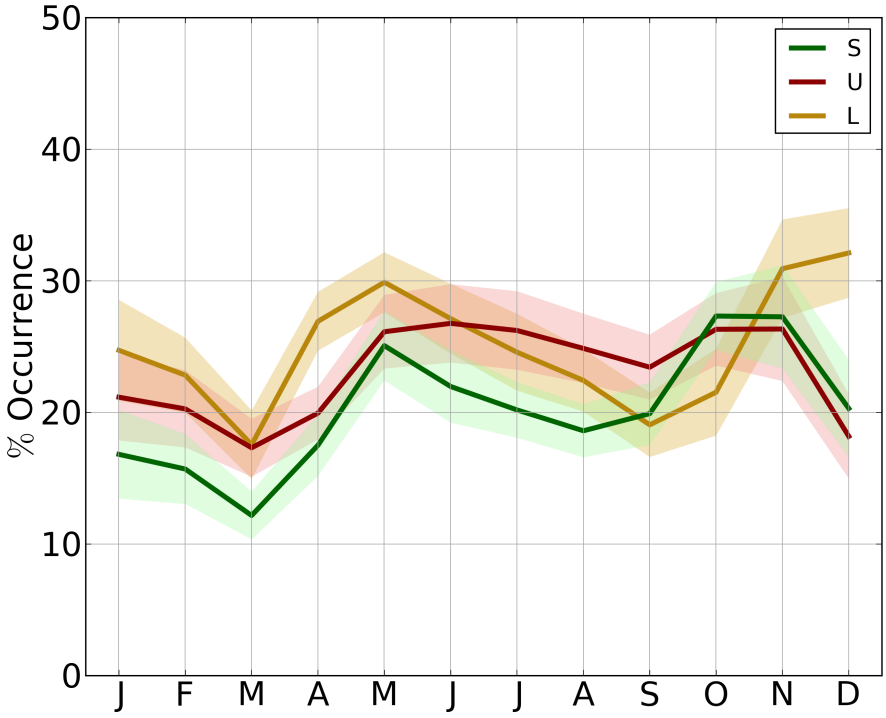

Figure 2.7: Observed monthly averaged front occurrence frequency in each of the regions defined in Figure 2.1. Error represents one standard deviation centered around the average.

Three areas of interest, as shown in Figure 2.1, have been defined within our domain in light of the occurrence patterns of frontal activity revealed from the seasonal maps (Figure 2.6). L is the Loire river plume region, U is the Ushant frontal region in the Iroise Sea, and S is the shelf break region along the 200 m isobath. Figure 2.7 shows the climatology of front occurrence frequency. It is calculated for each month (similarly to the seasonal distributions) and averaged over each box.

In L (Loire river plume) region, two peaks are observed in April-May and in November-December. The frontal activity is decreasing smoothly after each peak until minima (below 20%) of frontal activity. Conversely, increases toward maximum values are more abrupt and take place over periods of $\sim$ 1 month. In U (Ushant front) region, the frontal activity is minimum in winter and increases in May. This rate of frontal activity ($\sim$25%) is sustained during the whole stratified season from May until November. In S (shelf break) region, the frontal activity is very low (<15%) in winter. With the onset of seasonal stratification, the frontal activity is increasing to reach high values in May.

2.4 Modeled Frontal Activity

2.4.1 Spatio-temporal variability of frontal activity

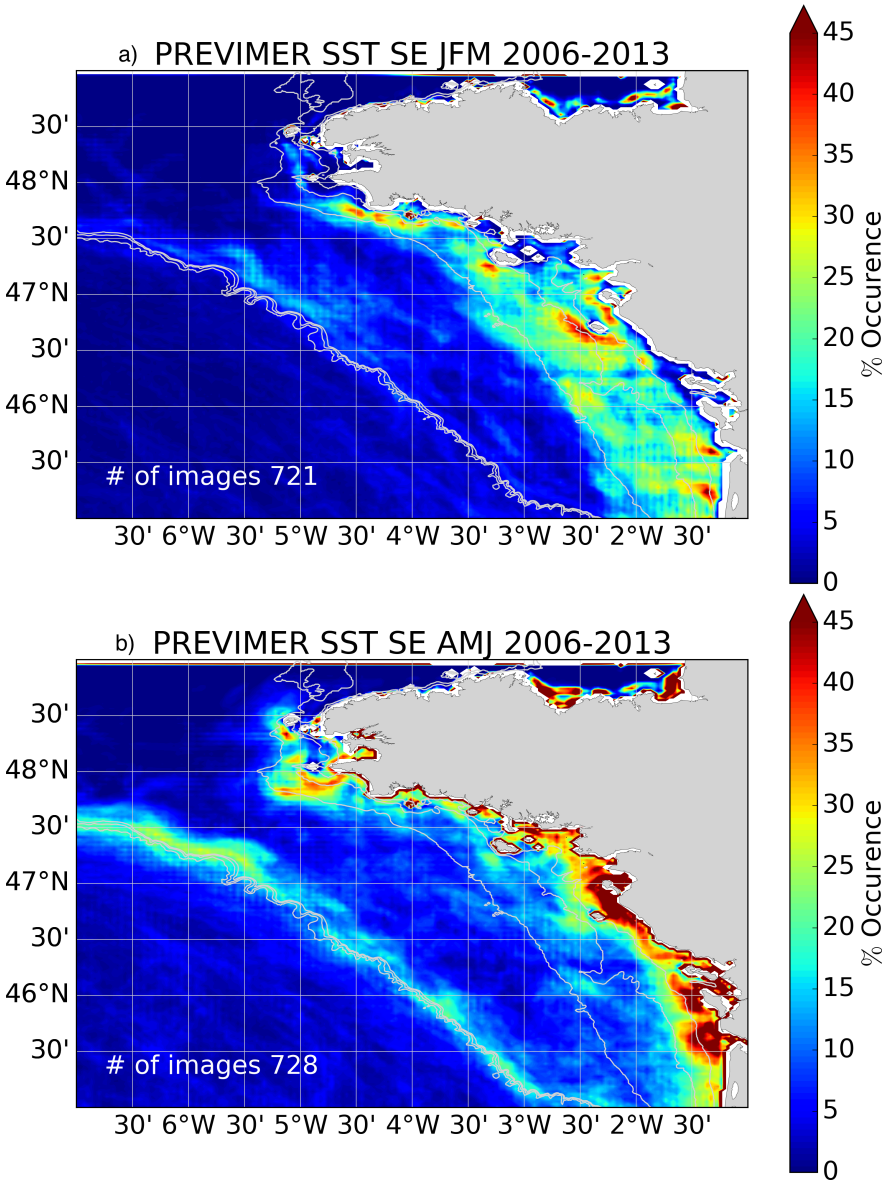
a) PREVIMER SST SE JFM 2006-2013
30'
48°N
30'
47°N
30'
46°N
30'
# of images 721
30' 6°W 30' 5°W 30' 4°W 30' 3°W 30' 2°W 30'
45
40
35
30
25
20
15
10
5
0
% Occurence
b) PREVIMER SST SE AMJ 2006-2013
30'
48°N
30'
47°N
30'
46°N
30'
# of images 728
30' 6°W 30' 5°W 30' 4°W 30' 3°W 30' 2°W 30'
45
40
35
30
25
20
15
10
5
0
% Occurence

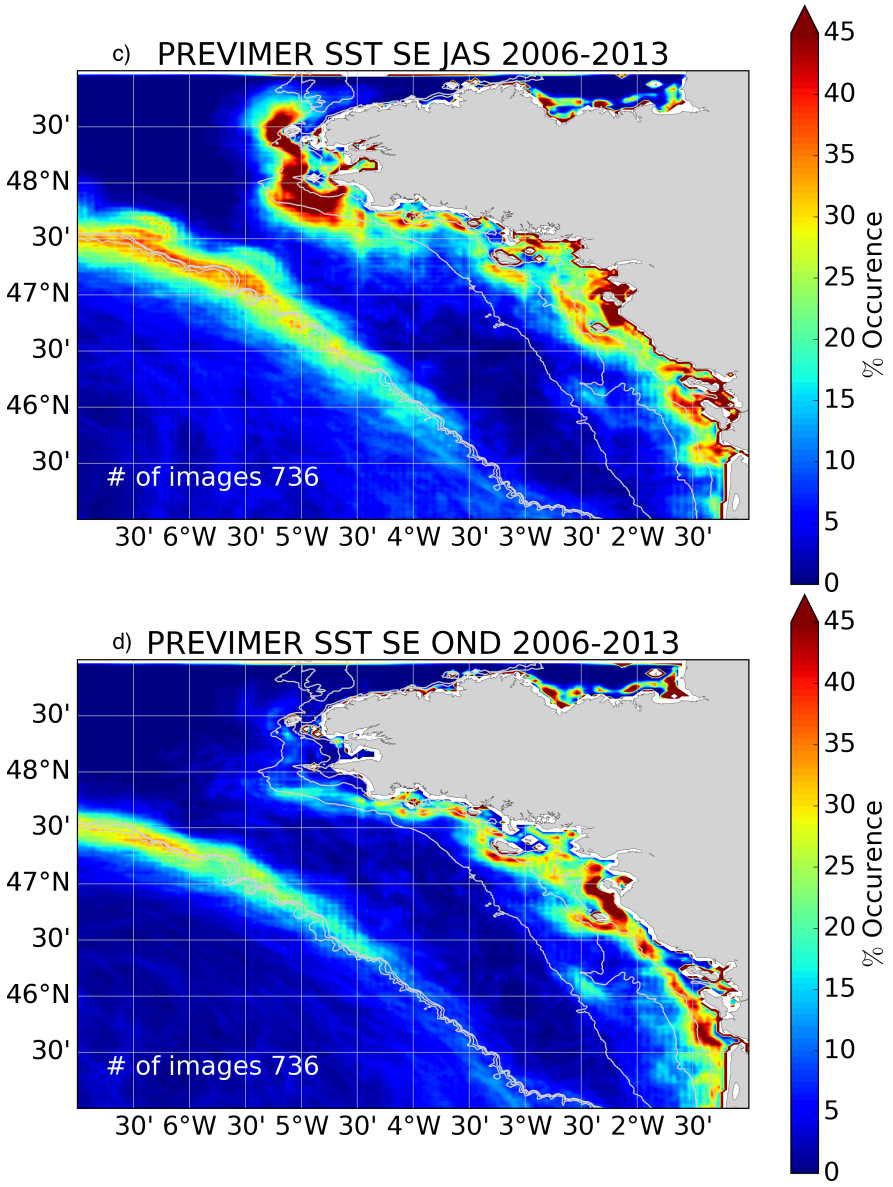

Figure 2.8: Front occurrence frequency of the modeled sea surface temperature expressed in percentage of number of times a pixel is cloud-free from 2006 to 2013 in a) winter (January, February, March), b) spring (April, May, June), c) summer (July, August, September), and d) autumn (October, November, December).

To connect the model simulations with the remotely sensed observation analysis performed in this study, the front occurrences have also been estimated from the modeled fields following the same methodology. However, two differences have to be mentioned: *i)* in the model analysis, there is no cloud coverage so there is no gap in the time series or masked pixels, and *ii)* modeled SST fileds have a lower resolution of 2.5 km. As displayed in Figure 2.8, from the continuous simulation from 2006 to 2013, the seasonal front occurrence frequency maps exhibit a good qualitative agreement with the seasonal maps from satellite observations (Figure 2.6). The wintertime fronts over the inner shelf are followed by the tidal and shelf break fronts in summer, and between them the transition periods in spring and autumn. Intensity of the model front occurrence frequency is generally lower than the observations outside of the frontal regions. The model has difficulties reproducing low but non-zero levels of occurrence, *i.e.* it has insufficient background frontal activity. Horizontal resolution is 2.5 km, which in practice means that features smaller than $\sim$ 10 km scale cannot be represented by the model, whereas satellite observations can in practice detect arbitrary contrasts between one pixel and its neighbors. Nonresolved ocean dynamics and atmospheric variability (*e.g.* fine-scale random fluctuations of winds and heat fluxes), possibly in combination, are the presumable source of this difference. Note that instrument noise may also be a reason for these differences.

After exploring the spatial distribution of the modeled frontal activity, the climatology of the annual evolution (Figure 2.9) has been computed and compared with observed climatology for the three specific regions (Ushant front, Loire river plume, and shelf break regions). In the case of modeled fields, analyzed fields are continuous in time and covers every day from 2006 to 2013, whereas the observations have gaps due to cloud coverage. Figure 2.9 has several important similarities with observations (Figure 2.7). This is particularly true for the L region with extreme of frontal oc-

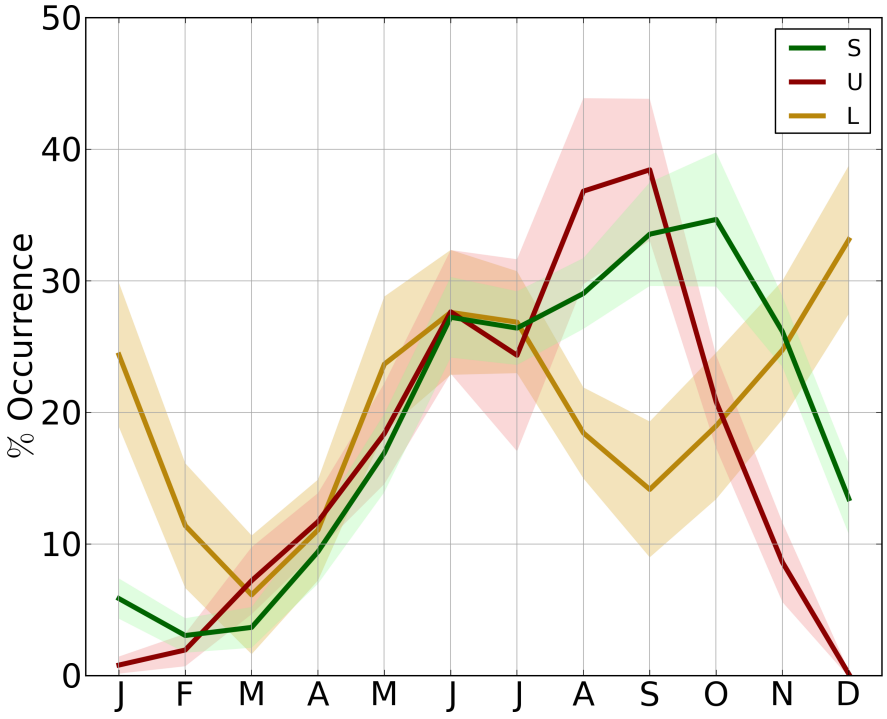

Figure 2.9: Monthly averaged front occurrence frequency in each of the regions defined in Figure 2.1. Error bars represent one standard deviation centered around the average.

currence that are quite accurately coincidental in model and observations. However, seasonal variations are more contrasted in the model. The modeled front occurrence probability is higher than the observed maxima, especially during summer-time in S and U regions. Modeled fields have a resolution of 2.5 km where as the observations have ∼1 km. These respective resolutions imply that roughly nine MODIS grid cells fit in one model grid cell. Consider a simple situation with a single stationary front present in one given model pixel. Frontal probability for that "large scale "pixel will be 1. If the front undergoes small - scale spatial fluctuations captured at 1 km resolution, frontal probability at 1 km resolution will be less than one over several 1 km pixels. Overall the area-integrated probability will be 1 at both resolutions, but maxima will be diminished as resolution is increased. In principle a simple rescaling would thus

allow one to compare the amplitude of maxima. In reality though enhanced resolution permits the representation of more fronts, so a simple rescaling shall not suffice and we are reluctant to interpret the difference in magnitude between modeled and observed frontal distribution. Rather we focus on their resemblances and dissimilarities in terms of patterns. As explained previously model lacks the minimum level of front occurrence, making the minimum in March in all regions is very weak with values below 10% of frontal occurrence. Both U and S regions remain active during the stratified period with values around or exceeding 30% from June until October - November. A time shift is also observed in the peak in the beginning of spring. This peak is visible in April - May in remotely sensed observations when the model peaks towards May - June.

The use of coastal modeling in this analysis allows us to explore the full seasonal cycle of the frontal activity and its interannual variability. In Figure 2.10, singularity exponents describe a seasonal cycle with a changing amplitude following the different year (negative values of the singularity exponents represent frontal activity). Although, generally coherent with the climatology, we can notice a marked interannual variability. In the Loire region (Figure 2.10a), most intense frontal activity are the winters of 2006-2007 and 2011-2012 and the summer 2010. The Ushant front (Figure 2.10b) displays a more stable seasonal cycle with small singularity exponents from summer to the beginning of autumn. In the shelf break region (Figure 2.10c), the seasonal cycle tends to have an increasing amplitude with time. From 2006 to 2009, values of singularity exponents remain in a limited range (from $\sim$-0.2 - $\sim$0.4). More recently, from 2010 and onward, maximum values exceed 0.6 representing period with less intense fronts in winter compared with previous years.

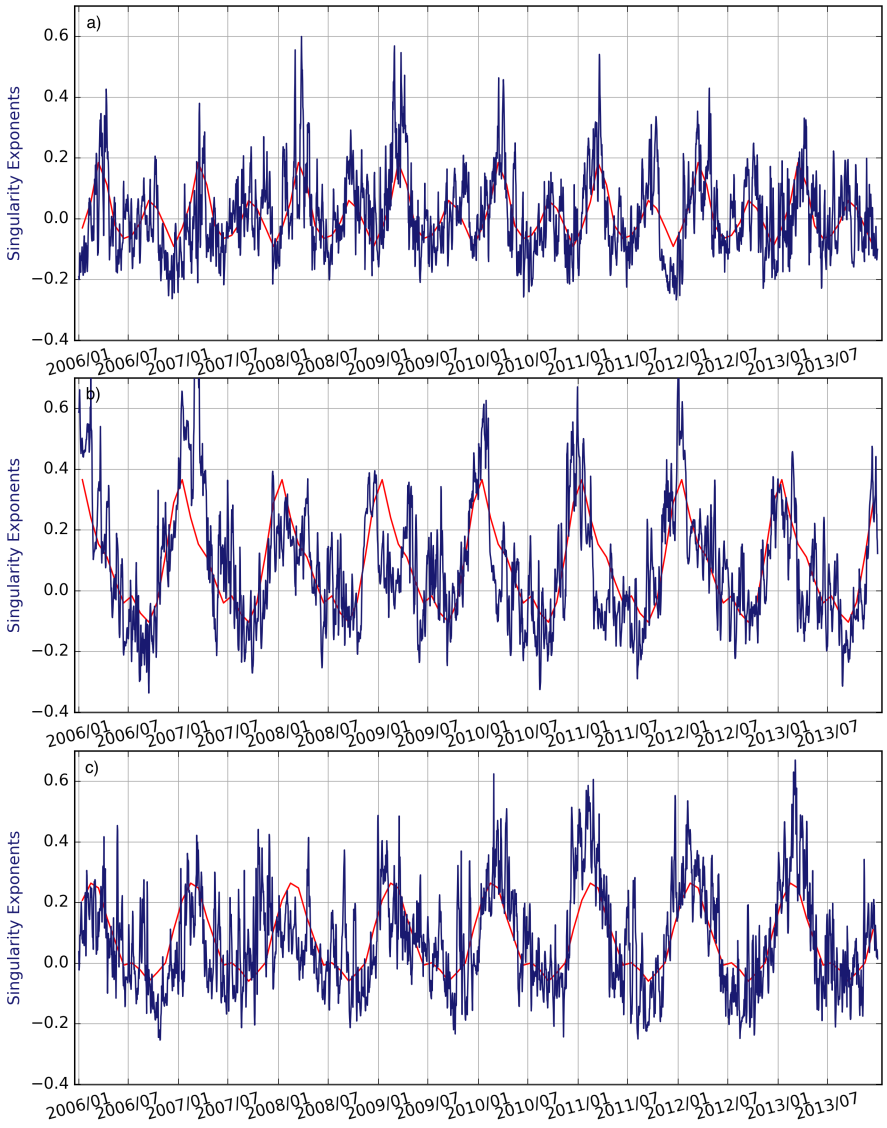

Figure 2.10: Singularity exponents of sea surface temperature (blue) and its climatology (red) from PREVIMER model simulations averaged over box a) L, b) U, and c) S (Figure 2.1) from 2006 to 2013.

2.5 Discussion

Based on these observations and numerical experiments, the frontal activity in the Bay of Biscay has been described including the spatial and temporal structures of the front distribution. The processes driving this frontal activity are discussed following a classification related to the nature of the front: freshwater fronts, tidal fronts, and shelf break fronts. This classification is possible thanks to the Singularity Exponent Analysis approach, which, by construction, can capture different turbulent regimes in the ocean.

2.5.1 Freshwater fronts

Starting from mid-autumn until mid-spring, the plumes of the Gironde and Loire follow the coast line to the north (Puillat et al., 2004). The inner shelf North of these estuaries (*i.e.* up to the location of the 30 - 100 m isobath, on average 20 - 40 km from the coast) is mainly occupied by relatively fresher waters with salinity ≤ 30. During these seasons, prevailing South-West (downwelling favorable) winds and increased freshwater input help maintain a low salinity band attached to the coast (Puillat et al., 2004; Lazure et al., 2006). The limit of this region of freshwater influence corresponds to large frontal activity (Figures 2.6 and 2.8). For example, in Figure 2.11c,d, the vertical structure of a density front from model simulations is shown for a winter condition (11 February 2008). In this season, closer to the coast plumes are surface-advected (Yankovsky and Chapman, 1997). They occupy the upper $\sim$10 m layer and cause a haline stratification. As explained in Ullman and Cornillon (2001), when the shelf is subject to winter cooling, this upper fresher/lighter layer cools faster than the offshore well-mixed waters, because the convection due to heat losses is frequently arrested by the halocline. Towards the midshelf, they are bottom-trapped as explained in Chapman and Lentz (1994). The waters with temperature $\leq 10\,^{\circ}$C are then confined along the coast (Figure 2.5a). Due to this differential cooling, we can identify these SST fronts as freshwater fronts. They

occur mainly at the offshore edge of this freshwater band, where average cross-front temperature difference reaches 2 °C km^{-1}. Note that, in the example MODIS image in Figure 2.11a, interesting signs of classical submesoscale baroclinic instability can be seen with filamentary and eddy features folding this plume edge front between the waters with relatively uniform SST $\geq$ 11.2 °C and colder inshore waters. The signature of dynamical instability becomes less clear fronts south, perhaps because stirring of the flow by topographic constraints is stronger (for example, in the vicinity of the Plateau de Rochebonne).

The seasonal behavior of the freshwater fronts are detailed in Figure 2.10a from the singularity exponent averaged over the localized region in the vicinity of the Loire river plume (Figure 2.1b). Based on the continuous dataset from modeled fields, the seasonal variability is confirmed. Indeed, it is seen that the seasonal signal of the frontal activity correlates to the river discharge into this region (not shown). A sharp increase in frontal activity coincides with the first increase in river fluxes each year around the beginning of autumn. In autumn, the band of fresh water fronts are more coherent and pronounced compared to winter such that they reach a frequency of 50% of the time. However, it should be noted that in this season the frontal occurrence frequency is observed to be noisier in all regions of the bay. Cloud cover is highest in autumn (not shown). This reduces the number of cloud free images/pixels, but also increases the number of cloud contaminated pixels that are not properly detected by the masking algorithm of the MODIS dataset, hence the noisier SST signal at this season. The pronounced coastal strip of increased frontal activity in autumn can be explained by the average poleward current over the shelf in this season that carries warmer waters to the north (Lazure et al., 2008; Le Cann and Serpette, 2009). The coastal waters starting to cool in autumn are surrounded by these warmer waters, and furthermore, are confined by the along-shore current creating a sharper temperature gradient (Figure 2.12). Figure

2.9a shows the interanuual variability of front occurrence in Loire region. The winters with increased frontal strength is found to be occurring after dry summers (not shown). This can be explained by the fact that dry summers cause warmer coastal waters that create larger gradients when the river discharge starts to reappear in autumn. In this season, fronts are visible consistently along the 30 m isobath in model (Figure 2.8d) and in observations (Figure 2.6d). From autumn to winter as the plume develops, the maximum frontal occurrence travels offshore from the vicinity of the 30 m to a band between the 50 to 100 m isobaths (Figure 2.8a and Figure 2.6a). Around January, the frontal activity peaks and then declines towards the spring. The minimum activity is observed during March to April because the main frontal activity associated with the edge of the plume is located offshore of the L region. In spring, fronts appear just adjacent to the coast (Figure 2.6b), unlike in winter when they occur as far as the 100 m isobath. River run-offs decrease during spring (Puillat et al., 2004) and the prevailing winds reverse to northwestern (upwelling favorable) direction. This prevents the along shore northward propagation of the plumes and cause them to detach from the coast and disperse (Lazure and Jégou, 1998; Puillat et al., 2006, 2004). Freshwater no longer occupies such an extensive coastal area, and the above mentioned low salinity structure remains inside the river mouths. During summer, when the river discharge is minimum, there is an increase in frontal activity along the coast which can be attributed to the tidal fronts.

The process explaining the development of similar density fronts has been described in Chapman and Lentz (1994) and Yankovsky and Chapman (1997). In the Bay of Biscay, these fronts remain difficult to observe (in *in situ* or remotely) because their typical spatial scales are close to 1km. As for the realistic simulations, like ours, still tend to be a little too coarse to fully resolve the processes at play. Nevertheless, the present results illustrate, from ocean observations and coastal model simulations, the

development of these fronts initiated by a surface-to-bottom density gradient over a sloping continental shelf as well as the "trapped" fronts (Chapman and Lentz, 1994), here along the 100 m isobath.

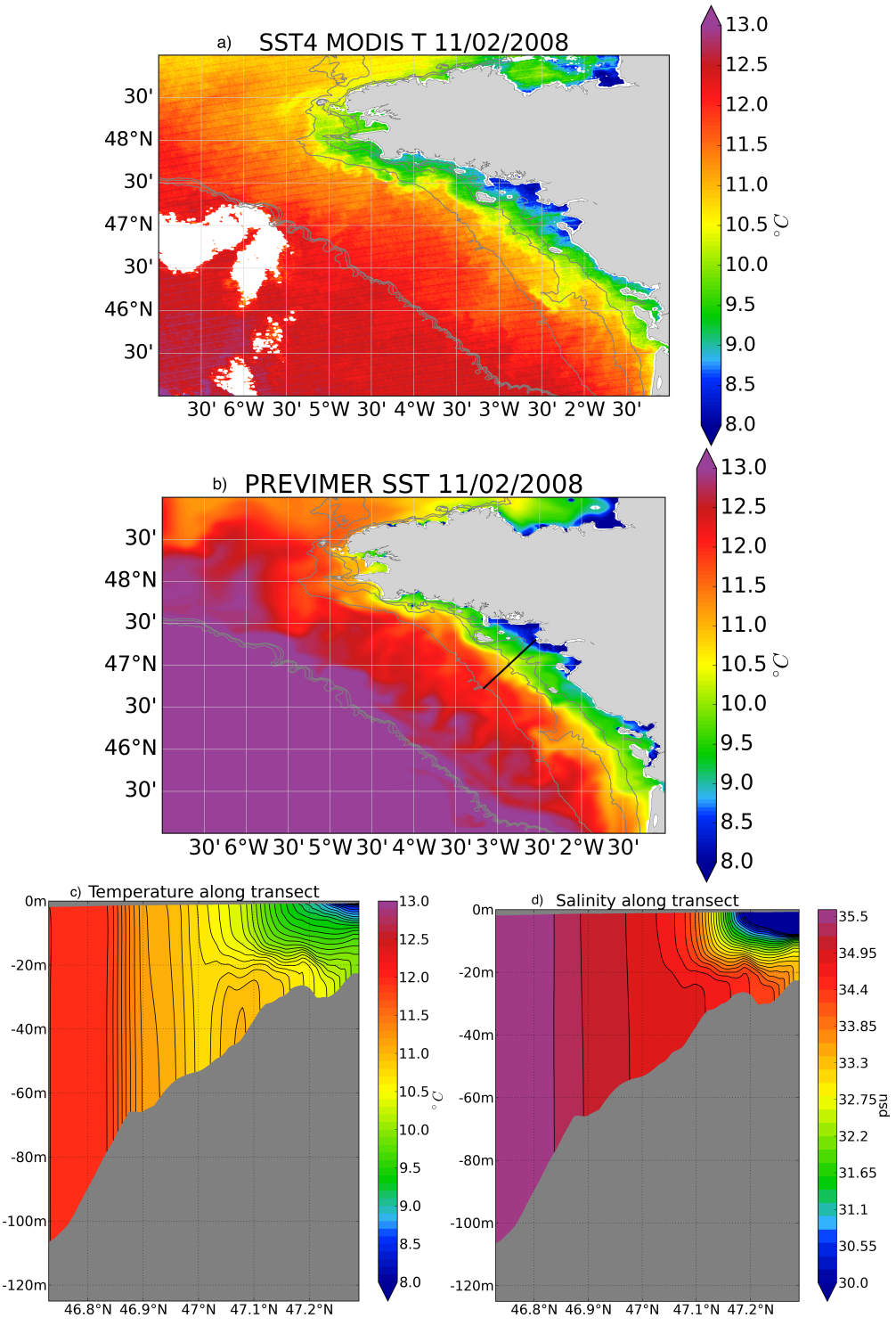

Figure 2.11: Remotely sensed sea surface temperature (a), modeled sea surface temperature (b), temperature (c) and salinity (d) along transect (black line on (b)) from the PREVIMER model simulations on 11/02/2008.

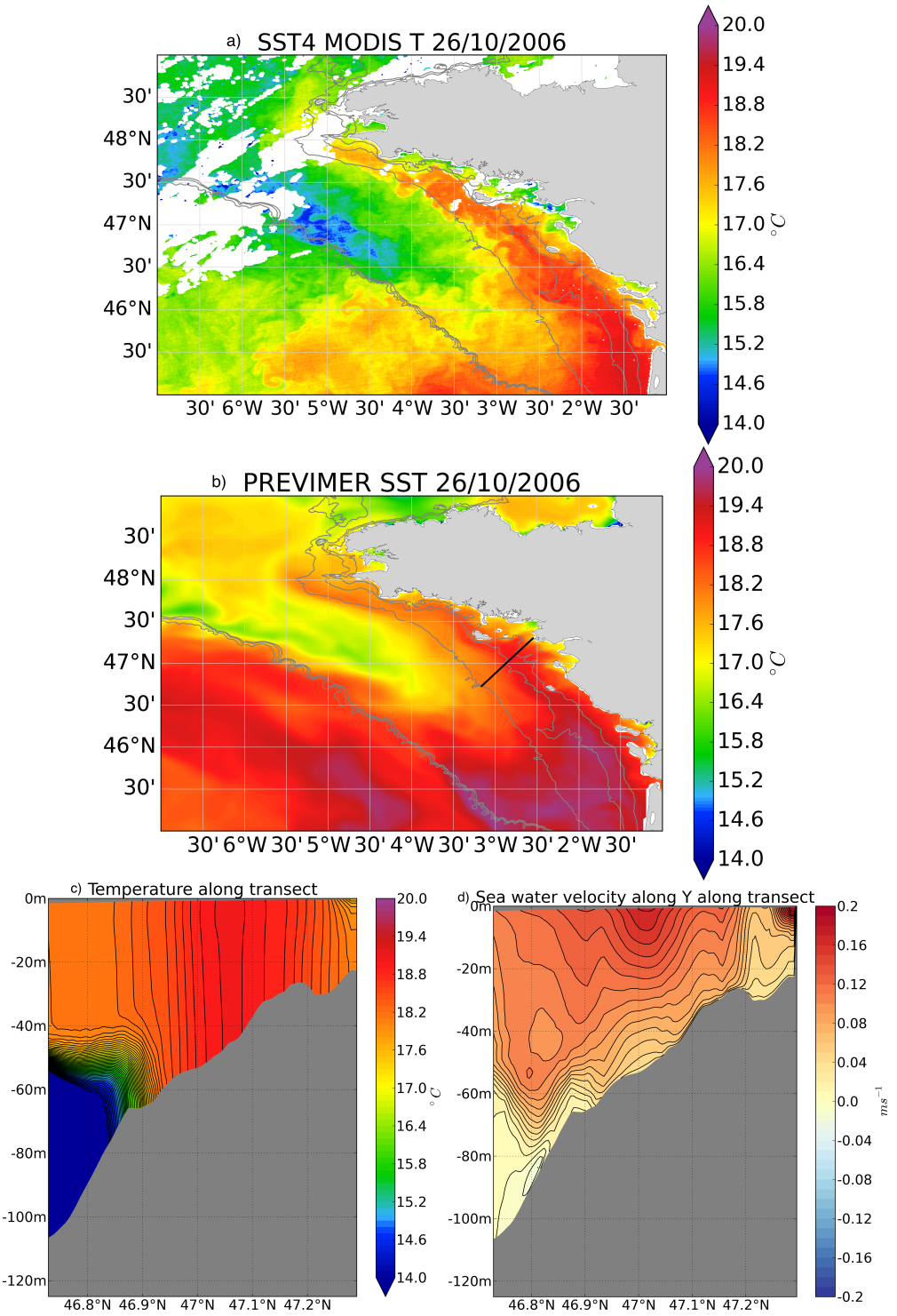

Figure 2.12: Remotely sensed sea surface temperature (a), modeled sea surface temperature (b), temperature (c) and meridional velocity (d) along transect (black line on (b)) from the PREVIMER model simulations on 26/10/2006.

2.5.2 Tidal fronts

Tidal mixing at the coast that results from the interaction between the tidal currents and the bottom topography can create a cool vertically mixed water mass. A tidal front is the region of temperature contrast separating this mixed water from the thermally stratified offshore waters. The northeastern European continental shelf is a well studied region in terms of the dynamics of such tidal fronts (Simpson and Hunter, 1974; Simpson et al., 1978; Pingree and Griffiths, 1978; Bowers and Simpson, 1987). In the investigated region tidal fronts are observed in the Iroise Sea and along the coasts of Pointe de Penmarc'h, Archipel des Glénans, Belle-île, and Ile d'Yeu. Their appearance coincides with the onset of surface warming and stratification increase in spring. They become more prominent through summer and early autumn as the stratification is established. Then, they disappear in winter. The most significant tidal front occurrence among these is the Ushant front, which is the most prominent feature observed in SST as in Figure 2.13a. Its location is observed from the satellite dataset to be within a 5 - 10 km wide patch along the ∼100 m isobath off west of Brittany, which is in accordance with previous studies (*e.g.* Mariette and Le Cann, 1985; Le Boyer et al., 2009; Pasquet et al., 2012; Chevallier et al., 2014). This patch of frontal occurrences gradually expands to a much larger area from summer to autumn and appears less structured. Pasquet et al. (2012) explains the expansion and the deviation from the predicted front location as the dispersion of the mixed waters for which baroclinic instability is mostly responsible (the prediction is based on the criterion that compares the relative importance of mixing effects (proportional to u^3) and resistance to mixing (assumed to vary as h, the depth of the water column), Simpson and Hunter, 1974). We also observed that a second band of fronts appears inshore of the main frontal region near the 50 m isobath as previously observed (*e.g.* Pasquet et al. 2012).

Figure 2.10b shows the seasonality of the frontal activity in the Ushant region. As

expected in a tidally dominated coastal area, the frontal activity increases in spring, with the onset of the seasonal stratification, and peaks in July - August. From autumn to spring the frontal activity is significantly decreased, with some small but sharp increases around February, which is possibly caused by storms or extreme atmospheric events occurring in the Iroise Sea region.

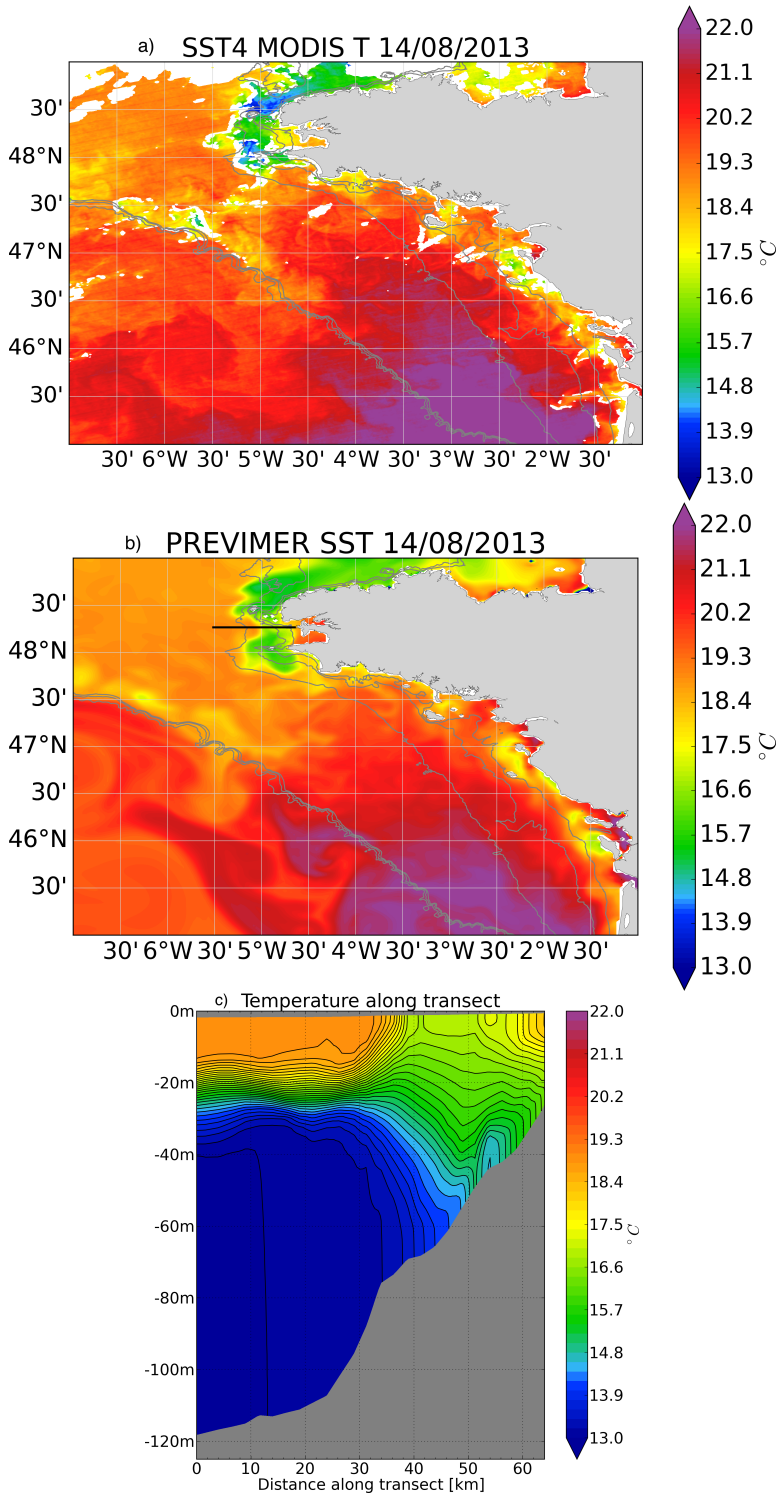

Figure 2.13: Remotely sensed sea surface temperature (a), modeled sea surface temperature (b), and temperature (c) along transect (black line on (b)) from the PREVIMER model simulations on 14/08/2013.

2.5.3 Shelf break front

Celtic and Armorican shelf breaks have been studied as one of the major large amplitude internal tidal wave generation sites in the world (Baines, 1982; Pingree et al., 1984; Serpette and Mazé, 1989; Pichon and Mazé, 1990), with La chapelle bank in the Bay of Biscay identified as a major generation region (Pairaud et al., 2010; New and Pingree, 1990; Pichon and Correard, 2006). In the Bay of Biscay, shelf break cooling and enhanced biological activity in its vicinity were first associated with internal tidal waves by Pingree et al. (1981). They lift cooler water (and nutrients) to the surface especially at spring tides during summer months (New, 1988; New and Pingree, 1990; Pingree and New, 1995). Large internal tidal waves are generated due to the interaction between the barotropic tidal currents and steep topography at the shelf break in the presence of strong stratification and they travel both onshelf and offshelf along the seasonal thermocline (Pingree and New, 1995; Pairaud et al., 2010). A large fraction of these waves dissipate locally through breaking which results in mixing. How this energy dissipation and mixing is distributed as a function of depth has important consequences for tracer fluxes and critically depends on the background stratification. When a sharp thermocline is present, as during summer in the Bay of Biscay, a significant fraction of the mixing involves thermocline and surface waters. Figure 2.14c shows the vertical structure of such a front. The surface manifestation of this mixing is described by Pingree and New (1995) as a 1 to 2 °C cooler than further on the shelf, $\sim$ 30 km wide patch along the shelf break from late spring to autumn. Figure 2.14a is one such example from 20/10/2007, where the region above the shelf break north of 46.5°N is $\sim$1 °C colder. In our study, frontal activity is observed to be very significant in thermally stratified months along the 200 m isobath. It first appears in spring and prevails through summer. In autumn, the number of frontal pixels in this region increases and the patch of occurrence extends spatially. In Figure 2.9, this is seen in model simula-

tions as a peak in frontal activity at the shelf break region in October. Pingree et al. (1981) report on the broadening of the cool water band in this region towards autumn and explain it as the release of the potential energy stored in summer in the form of irregular baroclinic eddies. Note that in Figure 2.14a the patch of cold water at the shelf break is elongated and folded in ways that reflect mesoscale stirring with several mushroom-like cold SST patterns, (*e.g.*, near 4.5°W, 46.5°N or 5.7°W, 46.7°N). The extent to which this mesoscale activity results from local instabilities due to internal wave mixing itself (as opposed to being preexistent and related to other processes) is unknown at the present. Our model in its present version cannot be used to explore this, because there is a noticeable model bias at this season in the box S sector. There, the real ocean has its main temperature contrast over the slope whereas it is located over the shelf in the model (albeit just a few tens of kilometers too far north). This is expected to result in a very different expression for the instability processes, if only because the baroclinic Rossby radius is much greater over the slope than over the shelf. As a consequence the model is unable to produce large mesoscale structures, which unavoidably affects frontal statistics.

Figure 2.10c presents the seasonal cycle of the shelf break frontal activity is presented. The shape of the seasonal signal is correlated to the seasonality of the stratification, which is slightly asymmetrical in that it gradually increases from the beginning of spring through summer, but rapidly declines in autumn. The maximum activity occurs towards the end of summer and beginning of autumn, which agrees with the peak we observe in October (in the satellite data in Figure 2.7 and in model simulations Figure 2.9).

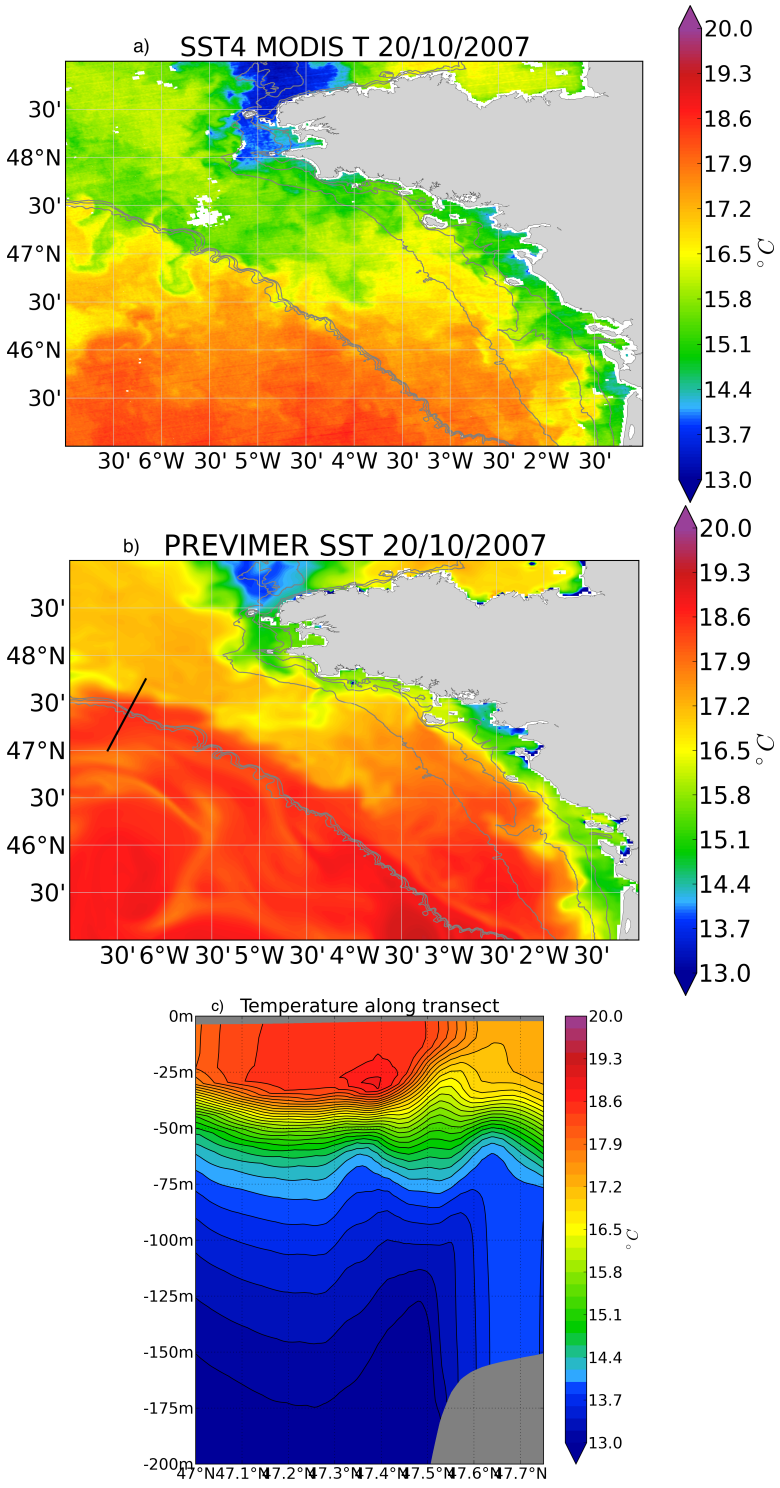

Figure 2.14: Remotely sensed sea surface temperature (a), modeled sea surface temperature (b), and temperature (c) along transect (black line on (b)) from the PREVIMER model simulations on 20/10/2007.

2.6 Conclusion

The length of the observation period by satellites providing high resolution SST information gives the opportunity to explore the frontal activity and to determine frontal statistics with great reliability. The present study considering 11 years (2003 to 2013) of remotely sensed SST in the Bay of Biscay shelf influenced by the Loire and Gironde river plumes provides an integrated view of the front occurrence, based on the singularity exponent decomposition. The use of singularity analysis allows inferring the multi-scale signature of the fronts. The front detection achieved by this method and the statistical analyses lead to a robust classification. The seasonal fluctuations of the frontal activity, deduced from remotely sensed observations and confirmed in numerical experiments, highlight the variety and complexity of the processes responsible for the front generation. Indeed, in summer and autumn, tidal and shelf break fronts developing in stratified conditions are dominant. Conversely, from late autumn to beginning of spring, frontal activity is concentrated over the continental shelf with localized mid-shelf frontal intensification. These winter and spring density fronts are the product of combined forcings. First, the river flow, which provides important sources of freshwater, determines where density gradients are located. Then, the air-sea heat fluxes will increase the temperature contrast between mid-shelf and coastal waters. These hydrodynamical conditions are favorable to the development of coastal density fronts trapped by the bottom boundary layer (Chapman and Lentz, 1994).

The temporal climatology of the frontal activity confirms that seasonal modulations of frontal activity responds to sub-regional environmental characteristics that we strived to identify and describe. Over the continental shelf in the Bay of Biscay, the frontal activity is maximum in winter. On the other hand, in the Iroise Sea or over the shelf break, the peak of the activity is observed in summer. Based on this first description of the spatial and temporal variability of frontal activity, two main regimes (winter

vs. summer) have been identified with the development of previously poorly observed density mid-shelf fronts in winter.

These frontal regimes we describe through their SST imprint must have distinct dynamical behaviors. Indeed, they take place in different parts of the shelf, where the role of friction and topographic stirring are different. In addition, their thermohaline structure also differs, which has some important implications in terms of the amplitude and modal structure of the frontal instabilities they can be subjected to (Hetland, 2010, 2016).

Biological implications of these frontal regimes would also need to be studied specifically. At present, we can only say that the seasonal Ushant frontal zone has well-marked contrasts in plankton composition (Schultes et al., 2013). We presume this must also hold for the more inshore freshwater fronts which are robust semi-permanent features in the Bay of Biscay. The role of the ephemeral fronts also captured by our analysis is less clear. General considerations suggest that they may lead to aggregation and dispersion of biological materials (Mahadevan, 2016), particularly the buoyant ones (Capet et al., 2008a). Clarifying the submesoscale links between ocean physics, biogeochemistry and ecosystem dynamics is the subject of intense research to which the Bay of Biscay has presumably important elements to offer.

2.7 Acknowledgments

This study is part of the LEFE/GMMC project ENIGME and the COCTO project (SWOT Science Team Program). The funding is provided for the Ph.D. study of Ö. Yelekçi by Brittany region and IFREMER. We would like to thank Daneeja Mawren, Louis Marié, Sébastien Theetten, Frédéric Vandermeirsch, Bernard Le Cann, Franck Dumas, Pascal Lazure, and Francis Gohin for insightful discussions; and PREVIMER project for model outputs. We are grateful to Pr. John H. Simpson and to an anonymous

referee for constructive comments on this manuscript.

Chapter 3

Submesoscale Regimes in the Bay of Biscay Continental Shelf

Contents

3.1 Introduction 62

3.2 MARS3D Numerical Model 62

3.2.1 Model Description 62

3.2.2 Bay Of Biscay Fine resolution (BOBF) Configuration 69

3.2.3 Modeled General Circulation and Hydrology 75

3.2.4 Model Skill Assesment 79

3.3 Submesoscale Diagnostics 89

3.3.1 Scale Decomposition 89

3.3.2 Submesoscale Vertical Buoyancy Flux and Eddy Kinetic Energy . 94

3.4 Discussion 103

3.1 Introduction

This chapter is dedicated to the numerical modeling study of the submesoscale dynamics over the continental shelf in the Bay of Biscay. Submesoscale dynamics have been studied with the help of high resolution realistic models for numerous oceanic regions (*e.g.*, Marchesiello et al. 2011; Mensa et al. 2013; Sasaki et al. 2014; Rosso et al. 2014, 2015), however, not as many in shelf regions (Capet et al., 2008a; Hetland, 2016).

One study that specifically deals with a shelf region which is under the influence of river inputs and is one of the main points of reference in this study is by Hetland (2016). Their focus is on the occurrence of baroclinic instability in the vicinity of the Mississippi - Atchafalaya river plume in the Texas - Louisiana shelf. We consider the dynamical setting in the Bay of Biscay shelf is very similar to theirs, and consider the baroclinic instability occurrence as the indicator of the submesoscale dynamics. Their findings suggest that occurrence of baroclinic instability at a plume front depends on the condition that the horizontal slope Burger number, S_H, is $\lesssim 0.2$. We test this condition for our plume region, and show that it is satisfied (see Discussion).

3.2 MARS3D Numerical Model

3.2.1 Model Description

MARS3D (3D hydrodynamical Model for Applications at Regional Scale)[†] is a three dimensional σ-coordinate numerical ocean model developed at IFREMER (Lazure and Dumas, 2008). It solves primitive equations under Boussinesq and hydrostatic approximations. Horizontal discretization is of the type Arakawa-C grid (Arakawa and Lamb, 1977). One specific feature of MARS3D is its coupling method of internal (barotropic) and external (baroclinic) modes, that are computed through "mode splitting", with an iterative predictor-corrector that enables a perfect fit between the barotropic and verti-

cally integrated 3D currents. In the following subsections a detailed description of the MARS3D is given.

3.2.1.1 Core Equations

For simplicity, the equations solved by MARS3D are presented in Cartesian coordinates in the horizontal and σ coordinates in the vertical. Following Hedström (1994),

$$z = \zeta\,(1+\sigma) + h_c\sigma + (H - h_c)\,C(\sigma) \tag{3.1}$$

and

$$C(\sigma) = (1-\beta)\frac{\sinh(\theta\sigma)}{\sinh\theta} + \beta\frac{\tanh\left(\theta\,(\sigma+1/2)\right) - \tanh(\theta/2)}{\tanh(\theta/2)} \tag{3.2}$$

where ζ is the free surface elevation, H is the bottom depth, h_c is the depth above which more resolution is needed, and θ and β are the surface and bottom control parameters. The total depth is defined as $D = \zeta + H$. $\sigma = 0$ at the bottom ($z = -H$) and $\sigma = 1$ at the surface ($z = \zeta$).

Momentum

In σ coordinates material derivative becomes

$$\frac{\mathrm{D}}{\mathrm{D}t} = \frac{\partial}{\partial t} + u\frac{\partial}{\partial x} + v\frac{\partial}{\partial y} + w^*\frac{\partial}{\partial \sigma} \tag{3.3}$$

where u, and v are the x (zonal, positive towards the east) and y (meridional, positive towards the north) velocities, and w^* is the vertical velocity in reference to σ layers, instead of w which is the physical vertical velocity. The relation between the two is as

[†]http://wwz.ifremer.fr/mars3d/

follows

$$w^* = \frac{1}{D}\left(w - \sigma\frac{\partial\zeta}{\partial t} - u\left(\sigma\frac{\partial\zeta}{\partial x} + (\sigma-1)\frac{\partial H}{\partial x}\right) - v\left(\sigma\frac{\partial\zeta}{\partial y} + (\sigma-1)\frac{\partial H}{\partial y}\right)\right). \quad (3.4)$$

Then, the x and y components of the Navier-Stokes equation, and the hydrostatic relation are

$$\frac{\partial u}{\partial t} + u\frac{\partial u}{\partial x} + v\frac{\partial u}{\partial y} w^*\frac{\partial u}{\partial \sigma} - fv = -g\frac{\partial\zeta}{\partial x} - \frac{1}{\rho_0}\frac{\partial P_a}{\partial x} + \Pi_x + \frac{1}{D}\frac{\partial\left(\frac{n_z}{D}\frac{\partial u}{\partial\sigma}\right)}{\partial\sigma} + F_x, \quad (3.5)$$

$$\frac{\partial v}{\partial t} + u\frac{\partial u}{\partial x} + v\frac{\partial v}{\partial y} w^*\frac{\partial v}{\partial \sigma} + fu = -g\frac{\partial\zeta}{\partial y} - \frac{1}{\rho_0}\frac{\partial P_a}{\partial y} + \Pi_y + \frac{1}{D}\frac{\partial\left(\frac{n_z}{D}\frac{\partial v}{\partial\sigma}\right)}{\partial\sigma} + F_y, \quad (3.6)$$

and

$$\frac{1}{D}\frac{\partial p}{\partial\sigma} = -\rho g \quad (3.7)$$

where f is the Coriolis parameter ($f = 2\Omega\sin\phi$, Ω: Earth's angular velocity, ϕ: latitude), ρ is density, ρ_0 is the reference density, p is pressure, P_a is the air pressure, and n_z is the vertical eddy viscosity.

Π_x and Π_y are the baroclinic pressure gradient terms in x and y directions and defined as

$$\Pi_x = \frac{\partial}{\partial x}\left[D\int_\sigma^1 b\mathrm{d}\sigma\right] + b\left(\sigma\frac{\partial D}{\partial x} - \frac{\partial H}{\partial x}\right), \quad (3.8)$$

and

$$\Pi_y = \frac{\partial}{\partial y}\left[D\int_\sigma^1 b\mathrm{d}\sigma\right] + b\left(\sigma\frac{\partial D}{\partial y} - \frac{\partial H}{\partial y}\right), \quad (3.9)$$

where b is buoyancy, and it is defined as $b = -g(\rho - \rho_0)/\rho_0$.

F_x and F_y are the horizontal friction terms in x and y directions and defined as

$$F_x = \frac{\partial}{\partial x}\left(\nu_H \frac{\partial u}{\partial x}\right) + \frac{\partial}{\partial y}\left(\nu_H \frac{\partial u}{\partial y}\right), \tag{3.10}$$

and

$$F_y = \frac{\partial}{\partial x}\left(\nu_H \frac{\partial v}{\partial x}\right) + \frac{\partial}{\partial y}\left(\nu_H \frac{\partial v}{\partial y}\right), \tag{3.11}$$

where ν_H is the horizontal eddy viscosity coefficient.

Continuity

The model is considering the following continuity equation:

$$\frac{\partial \zeta}{\partial t} + \frac{\partial (Du)}{\partial x} + \frac{\partial (Dv)}{\partial y} + \frac{\partial (Dw^*)}{\partial \sigma} = 0 \tag{3.12}$$

Advection-Diffusion

Transport of any tracer C (temperature, salinity, or dissolved matter) is governed by

$$\frac{\partial DC}{\partial t} + \frac{\partial D\left(uC - \kappa_H \frac{\partial C}{\partial x}\right)}{\partial x} + \frac{\partial D\left(vC - \kappa_H \frac{\partial C}{\partial y}\right)}{\partial y} + \frac{\partial D\left(w^*C - \kappa_V \frac{\partial C}{\partial \sigma}\right)}{\partial \sigma} = \text{Sources} - \text{Sinks}. \tag{3.13}$$

where κ_H and κ_V are the horizontal and vertical diffusivity coefficients.

3.2.1.2 Turbulence Closure ($k - \varepsilon$)

In MARS3D three types of turbulence closure options exist, that are algebraic, single-equation, and two-equation models. Information on all three types can be found on

MARS3D website[†]. The two-equation $k-\varepsilon$ model is used in this study. k stands for the turbulent kinetic energy, and ε stands for the dissipation of k. First of the equations gives the transport of k as

$$\frac{\partial k}{\partial t}+u\frac{\partial k}{\partial x}+v\frac{\partial k}{\partial y}+w^{*}\frac{\partial k}{\partial \sigma}=\frac{1}{D}\frac{\partial\left(\frac{\nu_V}{s_k}\frac{\partial k}{\partial \sigma}\right)}{\partial \sigma} + \underbrace{\nu_V\left(\left(\frac{\partial u}{\partial z}\right)^2+\left(\frac{\partial u}{\partial z}\right)^2\right)}_{\substack{\text{production}\\ \text{by velocity shear}}} - \underbrace{\kappa_V\frac{\partial b}{\partial z}}_{\substack{\text{destruction}\\ \text{by buoyancy}}} -\varepsilon, \tag{3.14}$$

where s_k is the turbulence Schmidt number for k and ν_V is the vertical eddy viscosity coefficient.

The second equation for ε is a simplified model by Luyten et al. (1996), and it is a relation between k, mixing length l, and ε, such that

$$\varepsilon=\varepsilon_0\frac{k^{3/2}}{l}, \text{ where } l=\kappa z_*\left(1-\frac{z_*}{H}\right)^{1/2} \tag{3.15}$$

ε_0 is computed from the stability coefficient, C_μ^0, based on experimental data and it is equal to 0.166. Above formula for the mixing length l is devised for the condition when there are surface and a bottom boundary layers, and z_* is the distance from the bottom and $\kappa=0.4$ is von Karman's constant.

Then, the vertical eddy viscosity (ν_V) and diffusivity (κ_V) coefficients are expressed as

$$\nu_V=lk^{1/2}S_M+\nu_{V_{bg}} \text{ and } \kappa_V=lk^{1/2}S_H+\kappa_{V_{bg}}, \tag{3.16}$$

where subscript bg denotes the background value, and S_M and S_H are stability func-

[†]http://wwz.ifremer.fr/mars3d/

tions. In MARS3D, a number of stability function formulations are included (Mellor and Yamada, 1982; Kantha and Clayson, 1994; Galperin et al., 1988; Burchard and Petersen, 1999; Canuto et al., 2001). In practice, these formulations allow us to take into account Richardson numbers from $Ri = 0.19$ (Mellor and Yamada, 1982) to Ri = 0.85 (Canuto et al., 2001), making the model efficient in regions of intense mixing.

3.2.1.3 Heat Fluxes

The net heat flux, Q_{net}, across the surface is computed from its four main components as follows,

$$Q_{net} = \underbrace{Q_{sol}}_{\text{Solar Radiation}} + \underbrace{Q_{ther}}_{\text{Thermal Infrared}} + \underbrace{Q_{lat}}_{\text{Latent Heat}} + \underbrace{Q_{sen}}_{\text{Sensible Heat}} , \tag{3.17}$$

where,

$$\begin{aligned} Q_{sol} &= S_0 \sin(z) f_{abs} f_{ext} (1 - \alpha) \\ Q_{ther} &= \varepsilon \sigma T_0^4 f_{vap} f_{clo} \\ Q_{lat} &= -\rho_a L_v C_E u' q' \\ Q_{sen} &= -\rho_a C_p C_H u' \theta'. \end{aligned} \tag{3.18}$$

For the radiative fluxes Q_{sol} and Q_{ther}, S_0 is the solar radiation reaching the outer atmosphere; $\sin(z)$ is the sun's altitude (function of latitude, day of the year, and time of the day); f_{abs} is the fraction absorbed by particles and gases; f_{ext} is the fraction of cloud extinction; α is albedo; ε is the emissivity of air; σ is the Stefan-Boltzmann constant; T_0 is sea surface temperature; f_{vap} is the function that gives vapor pressure at air temperature T_{air}; and f_{clo} is a function of cloud cover. The turbulent fluxes Q_{lat} and Q_{sen} are computed by the "*bulk*" formula, where ρ_a is the air density; L_v and C_p are the specific latent heat and the specific heat capacity of sea water; C_E

and C_H are drag coefficients; u is horizontal velocity; q and θ are specific humidity and potential temperature at the air-sea interface. The prime notation denotes the turbulent component (with respect to the value at the surface).

3.2.1.4 Boundary Conditions

Surface

At the surface ($\sigma = 1$),

$$\begin{gathered} w = 0 \\ \nu_V \frac{\partial u}{\partial z} = \frac{\tau_{sx}}{\rho_0}, \quad \nu_V \frac{\partial v}{\partial z} = \frac{\tau_{sy}}{\rho_0}, \\ \nu_V \frac{\partial T}{\partial z} = \frac{Q}{\rho_0 C_p}, \quad \nu_V \frac{\partial S}{\partial z} = 0, \\ \tau_{sx} = \rho_a C_d^s \|\overrightarrow{U_{10}}\| U_{10_x}, \quad \tau_{sy} = \rho_a C_d^s \|\overrightarrow{U_{10}}\| U_{10_y}, \; C_d^s = 10^{-3}(0.43 + 0.097 U_{10}), \end{gathered} \tag{3.19}$$

where C_d^s is the wind drag coefficient, and $\overrightarrow{U_{10}}$ is the wind velocity at 10 m.

Bottom

At the bottom ($\sigma = 0$),

$$\begin{gathered} w = 0 \\ \nu_V \frac{\partial u}{\partial z} = \frac{\tau_{bx}}{\rho_0}, \quad \nu_V \frac{\partial v}{\partial z} = \frac{\tau_{by}}{\rho_0}, \\ \nu_V \frac{\partial T}{\partial z} = 0, \quad \nu_V \frac{\partial S}{\partial z} = 0, \\ \tau_{bx} = \rho_a C_d^b \|\overrightarrow{u_b}\| u_{b_x}, \quad \tau_{by} = \rho_a C_d^b \|\overrightarrow{u_b}\| u_{b_y}, \; C_d^b = \left(\frac{\kappa}{\ln(z/z_0)} \right)^2, \end{gathered} \tag{3.20}$$

where C_d^b is the bottom drag coefficient, $\overrightarrow{u_b}$ is the velocity at the bottom, z_0 is the bottom roughness, and κ is the von Karman constant.

Open Boundaries

In the MARS3D code, Neumann ($\partial\overrightarrow{u}/\partial\hat{n}$ set to 0), Dirichlet, or Characteristics options are available. In this study the Dirichlet condition is applied. u, v, ζ, T, and S are prescribed at the boundary from a coarser resolution ocean general circulation model (OGCM) at each model time step.

3.2.2 Bay Of Biscay Fine resolution (BOBF) Configuration

3.2.2.1 Domain, time frame, choice of parameters

The BOBF (Bay of Biscay Fine resolution) configuration domain covers the area in the Bay of Biscay enclosed by 0 - 7°W and 43.25 - 49.25°N (Figure 3.1). It has a 1 km horizontal resolution (486 x 677 grid points) and 40 vertical σ layers. The configuration is based on the similar 1 km resolution BACH (Biscay-Channel) configuration developed in the framework of the ENIGME project (LEFE/GMMC) to explore the interannual variability in the Bay of Biscay (Charria et al., 2017).

Realistic atmospheric forcings and fresh water inputs are applied to the simulations. ARPEGE meteorological model output by Météo-France with 0.1° spatial and hourly temporal resolutions (ARPEGE High Resolution) (Déqué et al., 1994) were used. For freshwater inputs, the dataset constructed by the CDOCO (Data Center for French Coastal Operational Oceanography) with a daily temporal resolution was used. Open boundary conditions (OBC) and initial conditions (IC) are extracted from the outputs of the Ocean General Circulation Model (OGCM) ORCA12-MJM88 simulations. Developed in the frame of the DRAKKAR project[†] , ORCA12-MJM88 global simulation

(Molines et al., 2014) is based on the NEMO model and covers the period from 1958 to 2012. The spatial resolution is 1/12° with 46 vertical z-levels.

The simulation runs for three years from 2008 to 2010. The first two years are considered as spin-up and only the third year is analyzed. One instantaneous and one temporally averaged three dimensional field per day are recorded for each output parameter.

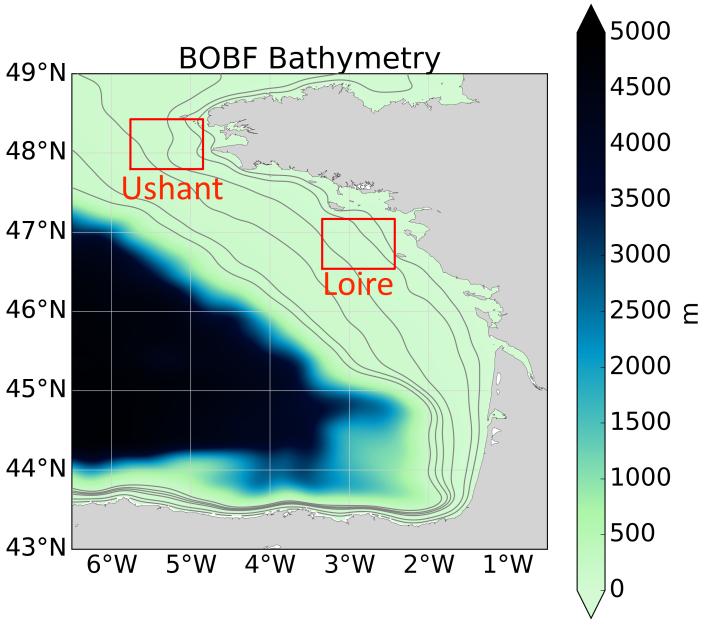

Figure 3.1: BOBF configuration model domain and bathymetry, showing the locations of Loire and Ushant subregions where temporal analyses are applied.

† http://www.drakkar-ocean.eu/

Technical framework on OCCIGEN

OCCIGEN is a Bull super-computer deployed in 2015. With 50544 cores and 2.1 Petaflop/s, it is the most powerful computer dedicated to the public research in France. Following the size of BOBF configuration (486 x 677 grid points), it has been decided to use OCCIGEN as the numerical environment. As part of the ENIGME project, this thesis study was included in the CINES proposal for 2016 to get a dedicated amount of time. Computational environment (libraries, modules, etc) required by MARS3D had been previously installed and tested, and maintained on OCCIGEN by our work group. Simulation launches are optimized for the capabilities of OCCIGEN. A series of performance tests has been launched on a varying number of nodes with different domain decompositions. Currently, the BOBF configuration runs on 53 MPI nodes (1 node = 24 CPUs).

3.2.2.2 Sensitivity runs

Sensitivity simulations are performed, where the OBC parameters are the major issue addressed, as other parameters of the model have been previously tuned for the BACH configuration. Table 3.1 lists the main simulations that are evaluated. Some minor simulations have also been performed, but not included, as they have not contributed to any information.

As an overview, Figure 3.2 shows modeled sea surface temperature (SST) from six of the test simulations on 12/02/2009. REF1 is the base configuration with all the model components included, on which tests are applied (see Table 3.1). REF1 simulations shows significant error at the western open boundary. The jet like velocities and vortices can be seen in temperature as they push colder waters originating further north at the boundary towards the continental slope. Firstly, comparison of REF2 and REF1,

with and without the velocity forcing at the boundary, shows no improvement, so the velocities extracted from the ocean general circulation model (OGCM) is assumed not to be the source of this error. Secondly, viscosity prescribed at the boundary sponge layer (20 grid points wide) is decreased, on the assumption that it might be over-damping the gradients at the boundary. In REF3 and REF4 sponge layer is relaxed such that the viscosity is 50 and 10 $m^2\ s^{-1}$, respectively, and no drastic difference is seen. Even in REF6, where the viscosity is set to 0 $m^2\ s^{-1}$ (equivalent to removing the sponge layer), there is a minor difference, which is not an improvement but strengthening of the jet-like velocities. Up to this point in all of the tests, the free surface, η, at the boundaries is not forced from the OGCM and only the tidal signal from the FES2004 tidal model output is applied. This means that the large scale circulation, besides the barotropic tidal component of η, from outside of the domain is not represented. In REF7, η at the boundaries is applied from the OGCM. The comparison with REF2, with and without η, respectively, shows very significant improvement. It has been decided that all realistic forcings at the boundary, tracers, velocity, and η, should be applied simultaneously.

Table 3.1: List of sensitivity simulations. (IC: initial conditions, OBC: open boundary conditions, T: temperature, S: salinity, U: barotropic current velocity, UZ: 3D current velocity, η: free surface elevation)

Run ID	**IC**	**OBC**	**Meteo.**	**River**
BOBF-REF0	MJM88: T, S	MJM88: T, S sponge visc.=100	ARPEGE	-
BOBF-REF1	MJM88: T, S	MJM88: T, S sponge visc.=100.	ARPEGE	CDOCO
BOBF-REF2	MJM88: T, S	MJM88: T, S, **U**, **UZ** sponge visc.=100.	ARPEGE	CDOCO
BOBF-REF3	MJM88: T, S	MJM88: T, S, **U**, **UZ**	ARPEGE	CDOCO

Table 3.1 – List of sensitivity simulations (continued).

Run ID	IC	OBC	Meteo.	River
		sponge visc.=50.		
BOBF-REF4	MJM88: T, S	MJM88: T, S, **U**, **UZ**	ARPEGE	CDOCO
		sponge visc.=10.		
BOBF-REF5	MJM88: T, S	MJM88: T, S, **U**, **UZ**	ARPEGE	CDOCO
		sponge visc.=1.		
BOBF-REF6	MJM88: T, S	MJM88: T, S, **U**, **UZ**	ARPEGE	CDOCO
		sponge visc.=0.		
BOBF-REF7	MJM88: T, S	MJM88: T, S, **U**, **UZ**, η	ARPEGE	CDOCO
		sponge visc.=100.		

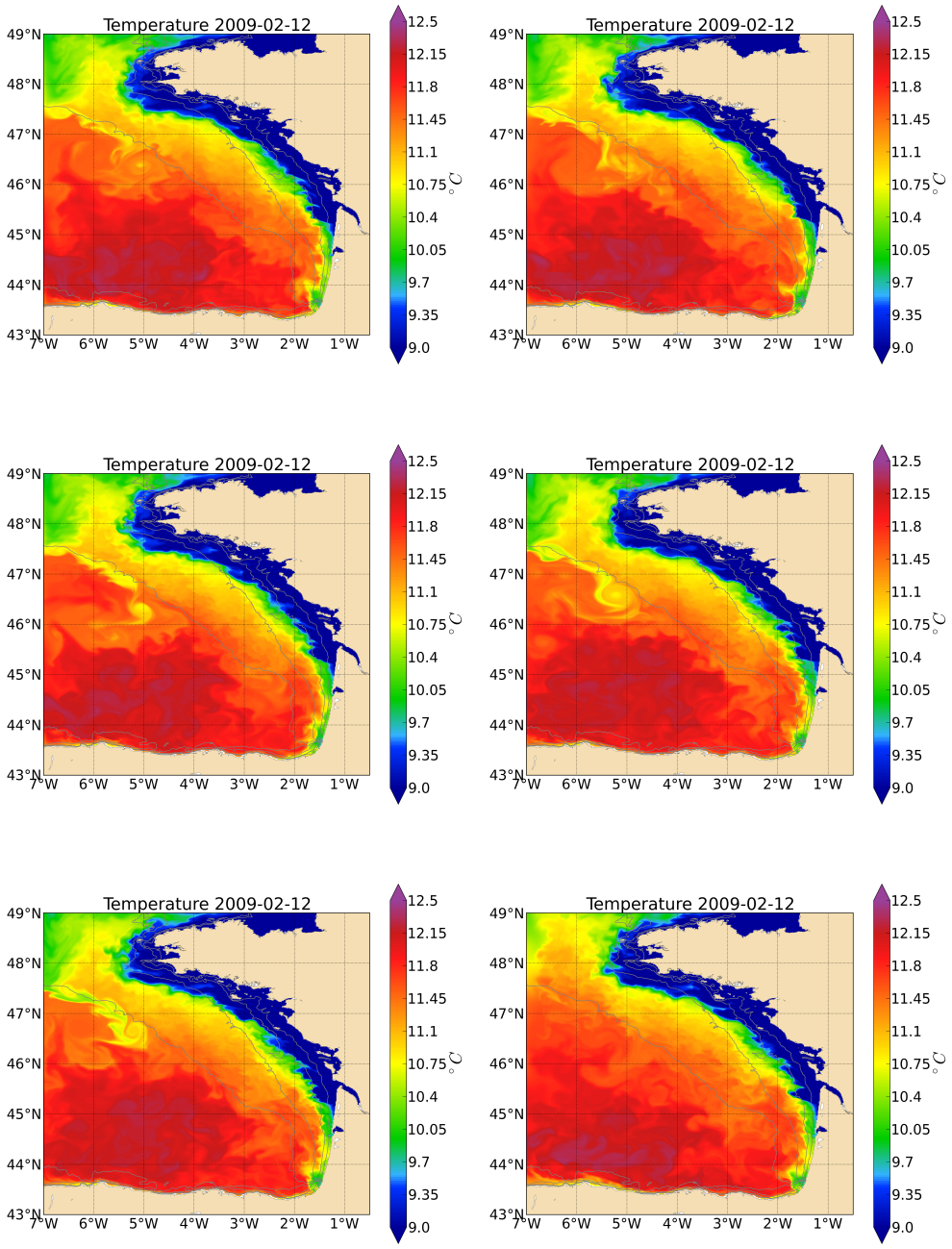

Figure 3.2: Examples of modeled sea surface temperature from a) REF1, b) REF2, c) REF3, d) REF4, e) REF6, and e)REF7 of the sensitivity simulations (Table 3.1) on 12/02/2009.

3.2.3 Modeled General Circulation and Hydrology

Before exploring the fine scale dynamics, simulated general physical properties of the Bay of Biscay shelf are presented in this section.

3.2.3.1 Overview of BOBF simulation

In winter (Figure 3.3), the shelf is dominantly under the influence of the fresh water inputs. Plumes from the Gironde and Loire rivers propagate towards the north following the coast. Dominant onshore winds keep this fresh water attached to the coast in a band roughly up to location of the 50 m depth. Surface salinity drops from $\sim$ 34.9 psu over the shelf to $<$ 30 psu at the coast. Temperature is almost uniformly $\sim$ 11 °C from mid shelf to shelf break and drop to $<$ 6 °C inside the plume. Because of the differential cooling of the plume in this season it's temperature signal is clearly visible. The density front created by the substantial fresh water along the coast creates major lateral gradients of about 0.2 - 0.3 kg m^{-3} km^{-1}. Along the plume front several features such as filaments and folds are seen in surface density that are indicative of instability. Surface circulation is weakly onshore over the shelf driven by seasonal SW winds and density driven along the coast with a moderate density current following the plume with velocities up to $\sim$ 1 m s^{-1}.

In summer (Figure 3.4), the inner shore is no longer occupied by the fresh water. Winds change to the NW direction starting from spring and detach the plumes from the coast. River discharges are decreased and plumes are seen in the surface salinity as thin elongated intrusions cross the shelf from the estuary mouths. Fresh water discharged during winter is advected offshore and covers the shelf up to the shelf break. Along the coast south of Brittany strong wind driven upwelling is evident in surface salinity. A north - south temperature difference over the shelf is significant in summer both due to the surface warming starting from the south and the strong tidal mixing effective in the

northern parts of the shelf. The Ushant tidal front and the shelf break fronts are only weakly produced by the model, reasons of which are explained in the following sections. However, very close to the coast small tidal fronts are visible from Arcachon Bay up to Brittany. Circulation over mid to offshelf is mostly weak in poleward direction, whereas over the inner shelf down front (equator-ward) velocities of up to 0.4 m s^{-1} is present, especially in the Iroise sea, in the vicinity of the Ushant front.

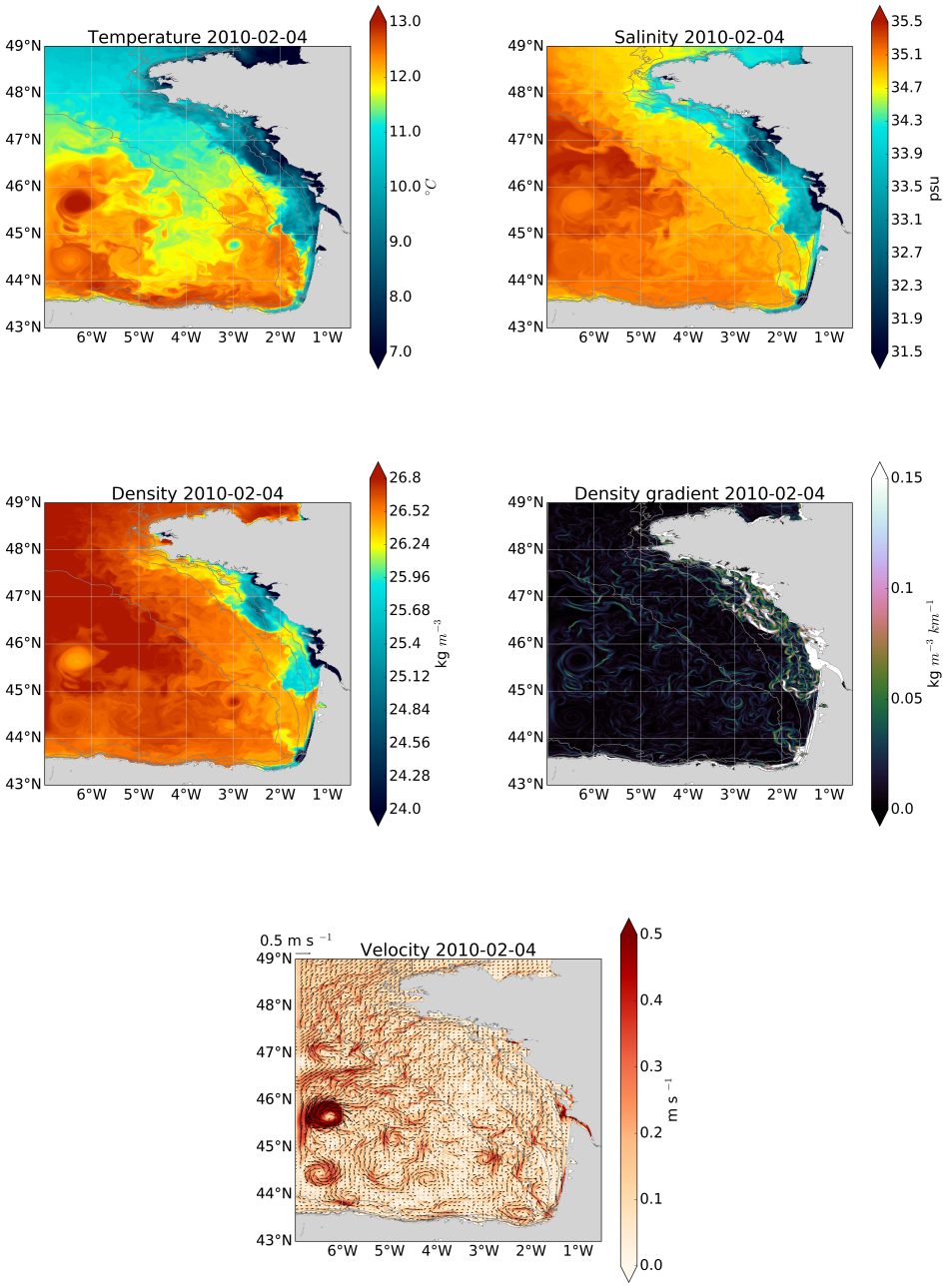

Figure 3.3: Examples representing the winter time conditions of modeled sea surface a) temperature, b) salinity, c) density, d) density gradient, e) velocity on 02/04/2010. The isolines represent the 30, 50, 125, 150, and 250 m isobaths.

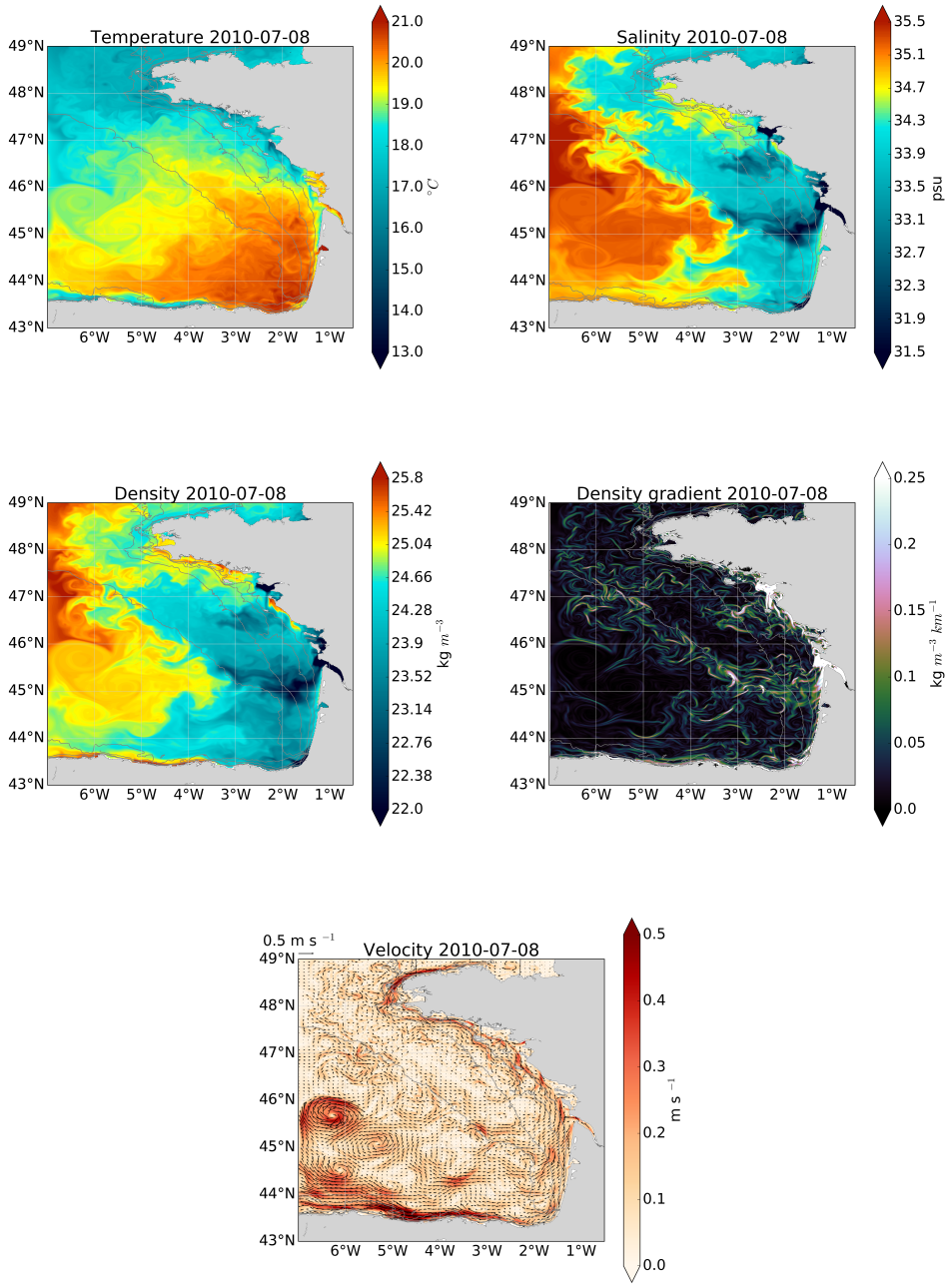

Figure 3.4: Examples representing the summer time conditions of modeled sea surface a) temperature, b) salinity, c) density, d) density gradient, e) velocity on 08/07/2010. The isolines represent the 30, 50, 125, 150, and 250 m isobaths.

3.2.4 Model Skill Assesment

To evaluate the capabilities of the BOBF configuration a comparison of model outputs to in situ data is presented. The measurements we considered are the RECOPESCA dataset. This dataset is based on profiles collected by voluntary fisheries vessels since 2007 from sensors implemented on fishing gears measuring temperature, conductivity, and pressure (Leblond et al., 2010; Lamouroux et al., 2016)[†]. We considered the data from all the available depths of the profiles collected over the Bay of Biscay shelf for the year 2010 (Figure 3.5).

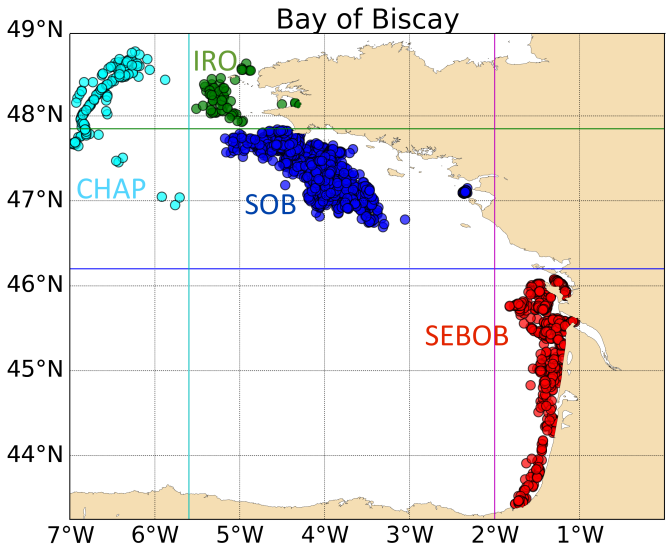

Figure 3.5: Locations of the RECOPESCA profiles that are compared to BOBF simulations, and four subregions defined for detailed comparisons.

Figure 3.6, shows the distribution of measured versus (measured - modeled) for

[†]http://www.coriolis-cotier.org

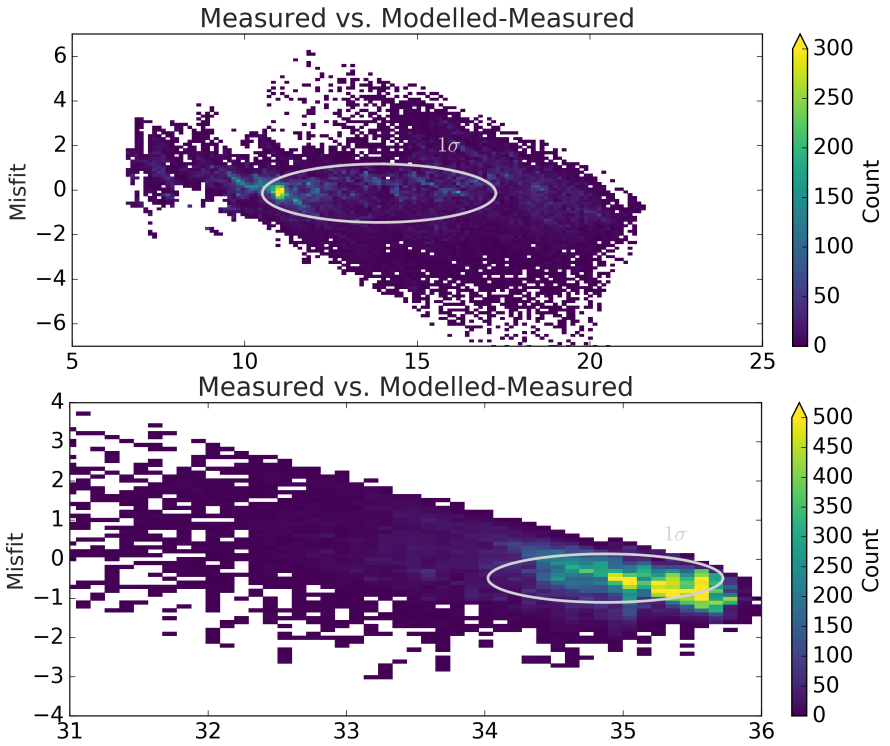

Figure 3.6: Composite comparison of BOBF simulations to RECOPESCA dataset. Modeled *vs.* (modeled - measured) temperature (top) and salinity (bottom). White ellipses are drawn such that their major(minor) axes is one standard deviation (σ) of the data along x(y), and the center is the point of maximum counts for the respective panels. (Locations of profiles in Figure 3.5).

temperature and salinity up to 180 m depth from the available profiles. For temperature, it shows that most of the profiles have a misfit lower than $\pm$ 1 ^oC. Model performs better at values lower than $\sim$ 14 ^oC where the misfit range is narrower. In salinity, misfit is mostly smaller than $\pm$ 1. The misfit spread of the model below 34 increases with values reaching 4. Above 34 the model simulations have a tendency to underestimate the salinity and the peak of the comparison falls slightly below zero misfit line.

Detailed versions of the Figure 3.6 shows the misfit diagrams in salinity and temperature for four subregions, color coded with respect to month and depth. In temperature (Figure 3.7), we observe that the better agreement between model and the observations

is in winter with misfit lower than 2 ^oC. The largest errors occur from August to November, mostly at depths shallower than 80 m. For example, in the south of Brittany misfits larger than 6 ^oC appear in August, whereas in Iroise sea it is in November. In salinity (Figure 3.8), we observe that the model does not perform well in producing the observed extrema. Indeed for lower salinities, model is saltier and for higher salinities model is fresher than observations. Almost all of the large errors occur in the surface layers, and from August to November.

From these comparisons, it can be concluded that the model does a better job where the water column is mixed. Most of the large errors are due to the difference in modeled and observed thermocline and halocline depths in stratified seasons.

Besides evaluating the vertical performance of the model, we also compared frontal activity from the model with the one from remotely sensed SST (Figure 3.9 and 3.10). Frontal occurrence maps are constructed as explained in Chapter 2. It should be brought to attention that the remotely sensed dataset covers 11 years from 2003 to 2013, whereas the simulated fields are from 2009 to 2010. Thus, due to both their smaller dataset size and the fact that there are no cloud masked pixels, modeled frontal occurrences lack the level of noise the observed fields have. It is seen that the model does a moderate job reproducing the features observed by the satellite. In winter, we see the band of fronts inshore of the 100m isobath driven by the river input. Although the modeled salinity has a certain misfit, occurrence of fresh water fronts agrees with the observed frontal locations. In summer and spring, the model simulation can produce the tidal fronts along the western coastline, but performs very poorly in producing the Ushant frontal occurrences as strong as the observations. This difference can be explained by the fact that the open boundaries are too close to this region inhibiting the frontal activity. Similarly, the open boundary cuts across the shelf break and damps the internal tidal wave generation there, diminishing the front observed in this region. However, the main

focus, in terms of processes, is dedicated to fronts located over the continental shelf, therefore the model performances are in agreement with the purposes of the study.

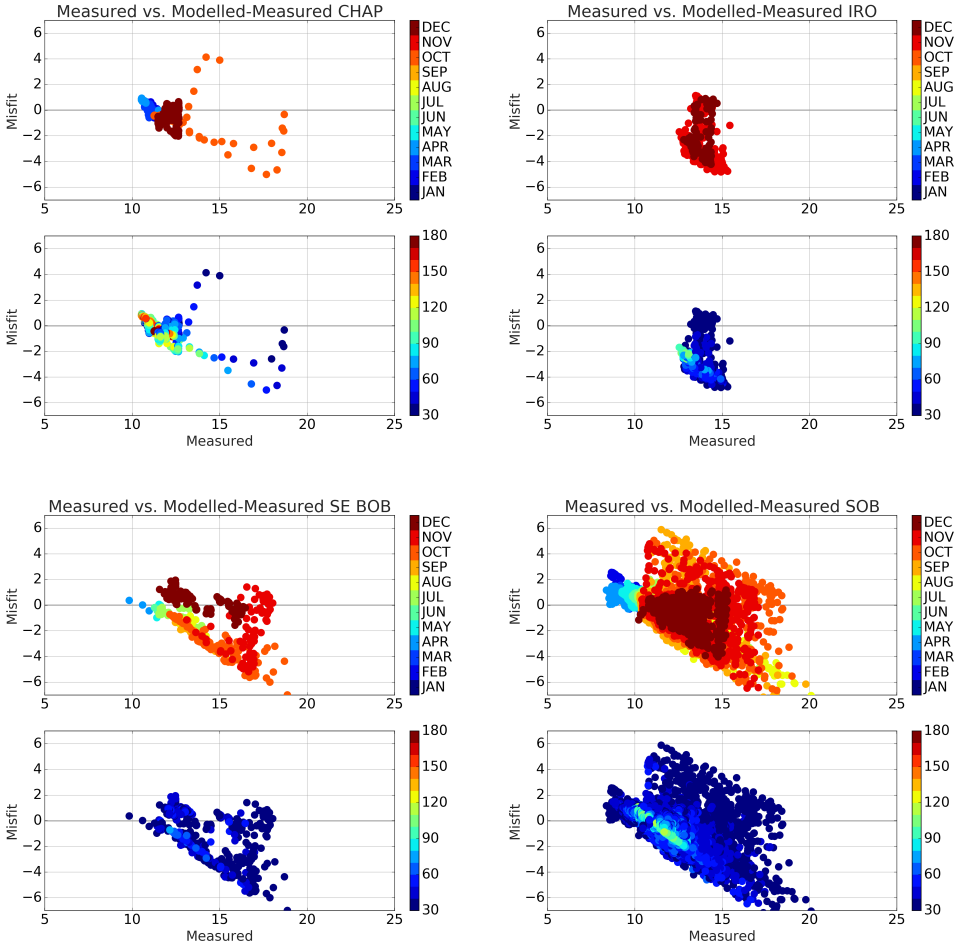

Figure 3.7: Detailed comparison of BOBF simulations to RECOPESCA dataset. Modeled *vs.* (modeled - measured) temperature from a) La Chapelle bank, b) Iroise sea, c) southeast Bay of Biscay, and d) south of Brittany (Locations of profiles in Figure 3.5). Data are color coded with respect to month (top) and depth (bottom) for each panel.

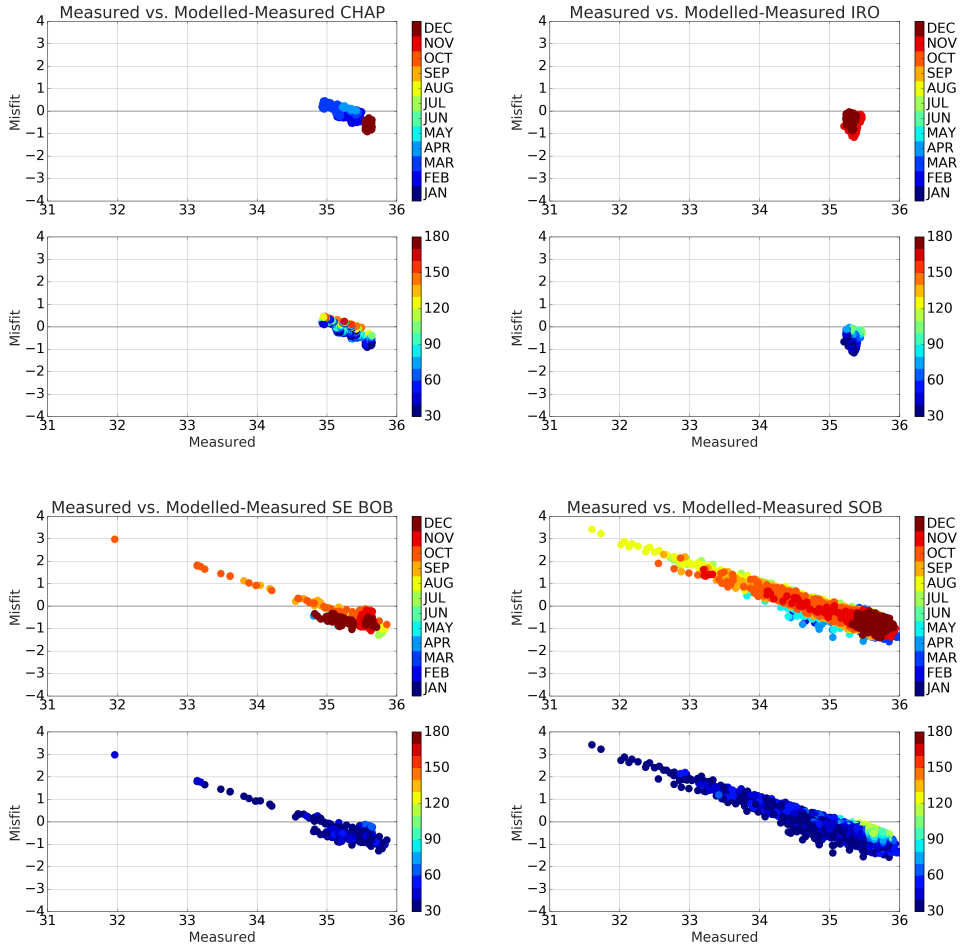

Figure 3.8: Detailed comparison of BOBF simulations to RECOPESCA dataset. Modeled *vs.* (modeled - measured) salinity from a) La Chapelle bank, b) Iroise sea, c) southeast Bay of Biscay, and d) south of Brittany (Locations of profiles in Figure 3.5). Data are color coded with respect to month (top) and depth (bottom) for each panel.

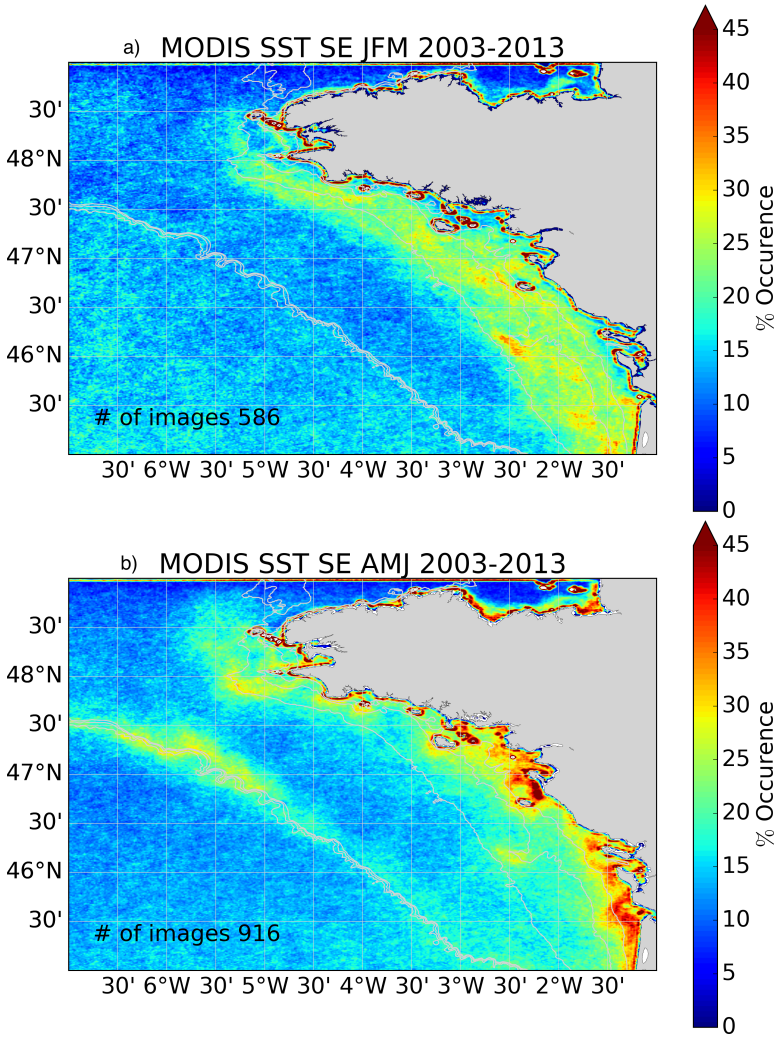
a) MODIS SST SE JFM 2003-2013
30'
48°N
30'
47°N
30'
46°N
30'
# of images 586
30' 6°W 30' 5°W 30' 4°W 30' 3°W 30' 2°W 30'
45
40
35
30
25
20
15
10
5
0
% Occurence
b) MODIS SST SE AMJ 2003-2013
30'
48°N
30'
47°N
30'
46°N
30'
# of images 916
30' 6°W 30' 5°W 30' 4°W 30' 3°W 30' 2°W 30'
45
40
35
30
25
20
15
10
5
0
% Occurence

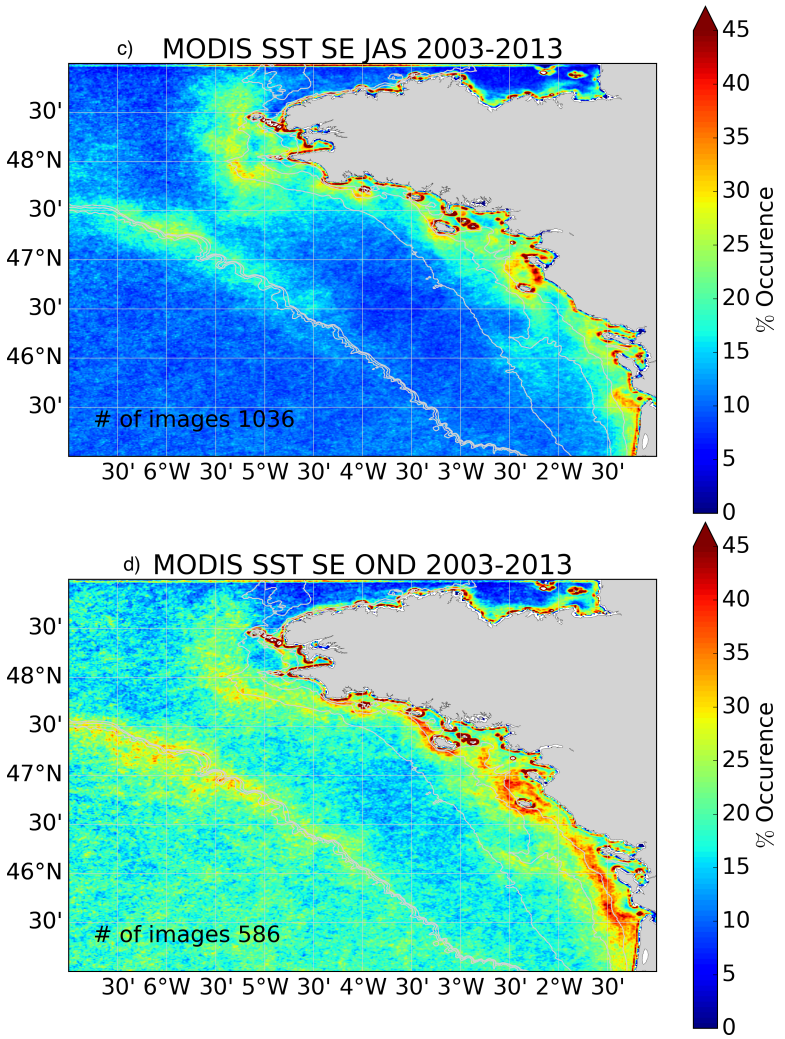

Figure 3.9: Front occurrence frequency of the MODIS remotely sensed sea surface temperature expressed in percentage of number of times a pixel is cloud-free from 2003 to 2013 in a) winter (January, February, March), b) spring (April, May, June), c) summer (July, August, September), and d) autumn (October, November, December). The isolines represent the 30, 50, 125, 150, and 250 m isobaths.

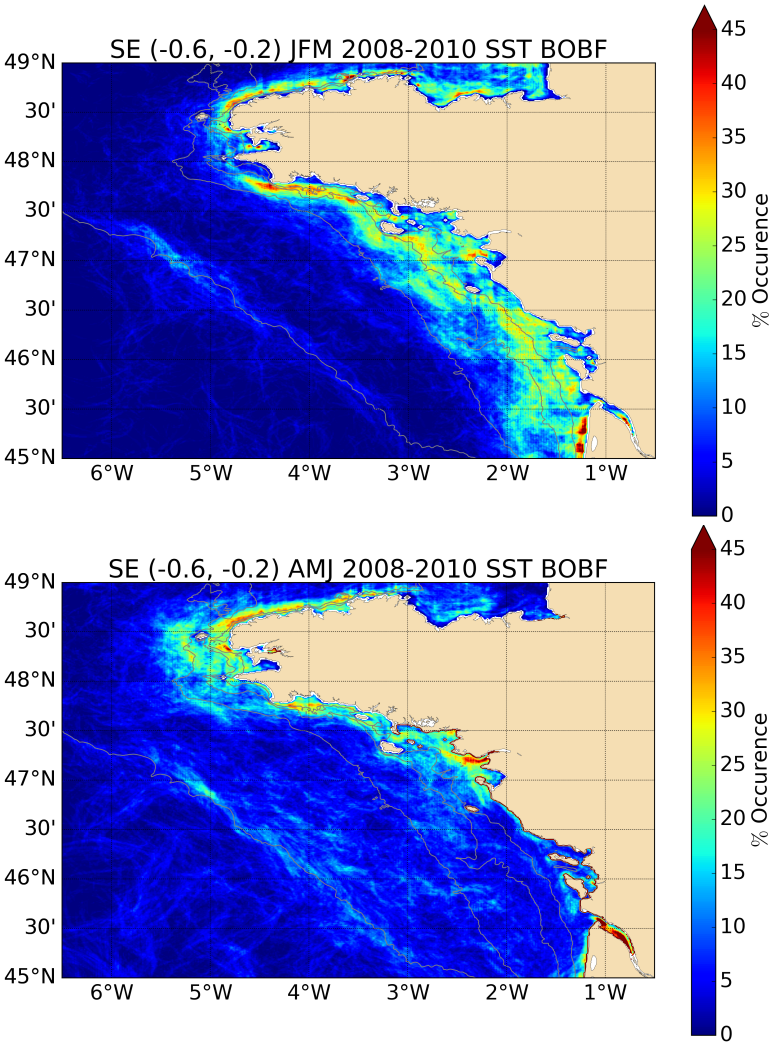
SE (-0.6, -0.2) JFM 2008-2010 SST BOBF
49°N
30'
48°N
30'
47°N
30'
46°N
30'
45°N
6°W
5°W
4°W
3°W
2°W
1°W
45
40
35
30
25
20
15
10
5
0
% Occurence
SE (-0.6, -0.2) AMJ 2008-2010 SST BOBF
49°N
30'
48°N
30'
47°N
30'
46°N
30'
45°N
6°W
5°W
4°W
3°W
2°W
1°W
45
40
35
30
25
20
15
10
5
0
% Occurence

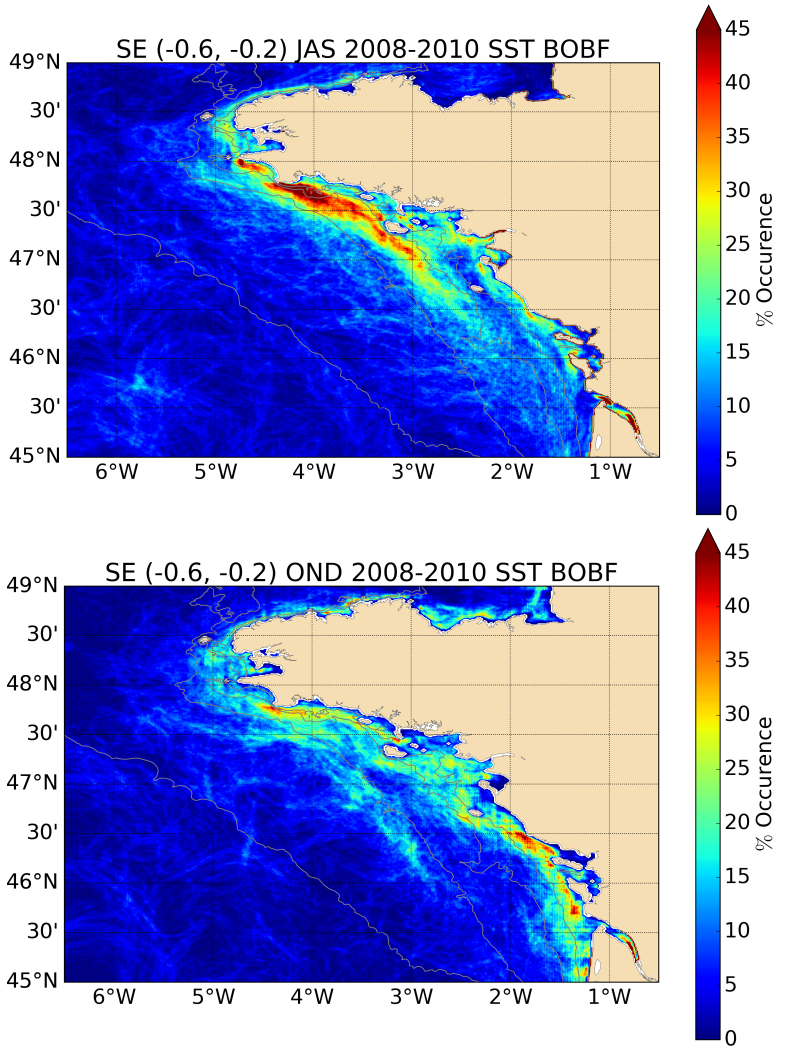

Figure 3.10: Front occurrence frequency of the modeled sea surface temperature from BOBF simulations expressed in percentage of number of times a pixel is cloud-free from 2009 to 2010 in a) winter (January, February, March), b) spring (April, May, June), c) summer (July, August, September), and d) autumn (October, November, December). The isolines represent the 30, 50, 125, 150, and 250 m isobaths.

3.3 Submesoscale Diagnostics

3.3.1 Scale Decomposition

Following Capet et al. (2008b), a decomposition distinguishing the mean, mesoscale, and submesoscale contributions is applied. The decomposition for a model variable V is represented by

$$\mathrm{V} = \bar{\mathrm{V}} + \underbrace{(\tilde{\mathrm{V}} - \bar{\mathrm{V}})}_{\mathrm{V}'} + \underbrace{(\mathrm{V} - \tilde{\mathrm{V}})}_{\mathrm{V}''}. \tag{3.21}$$

$\bar{\mathrm{V}}$, V', and V'' are the mean, mesoscale, and submesoscale components, respectively. $\bar{\mathrm{V}}$ is obtained by a very low pass filter, namely a monthly average. $\tilde{\mathrm{V}}$ is obtained by a medium low pass filter, where an appropriate choice of temporal and spatial averaging distinguishes between the meso- and submesoscale. It should be noted that for regions where mesoscale dynamics are not as dominant as they are in oceanic domain, such as continental shelves (*i.e.* our study region), the separation between meso- and submesoscales becomes less distinct. In this study, the medium low pass filter is performed by combining weekly averaging in time and 8 times 5-point horizontal smoothing in space. It means that submesoscales have time scales shorter than $\sim$ a week and spatial scales finer than $\sim$ 10 km for our 1 km simulation. Temporally, a weekly limit is perhaps a bit generous, but we will see that the dynamics we capture is fully compatible with submesoscale behavior and in particular with the dominance of vertical motions transferring available potential energy into kinetic energy through shallow baroclinic instability.

3.3.1.1 Decomposition of Vertical Buoyancy Flux

As described in chapter 1, submesoscale motions in the upper ocean are manifested in certain dynamical occurrences, one of which is the instabilities. Our approach to

qualitatively evaluate those submesoscale motions with the BOBF simulations is to assess baroclinic instability. Vertical buoyancy flux, wb, is one parameter that can be used to explore baroclinic instability, such that the sign of wb at the slumping isopycnals of an unstable frontal region is positive. Since the vertical velocity, w, and the buoyancy, b have different sources of variability, they are decomposed separately following equation 3.21, as

$$w = \bar{w} + w' + w'' \text{ and } b = \bar{b} + b' + b''. \tag{3.22}$$

Then, the product of these two quantities is

$$wb = \bar{w}\bar{b} + \bar{w}b' + \bar{w}b'' + w'\bar{b} + w'b' + w'b'' + w''\bar{b} + w''b' + w''b''. \tag{3.23}$$

In Figure 3.11a and b, components of w and b is shown for Loire region. w is seen to be mostly submesoscale (w''), whereas b is dominated by the large scale ($\bar{b}$) signal. Because w and b are distributed among their components very differently, the sum of the terms that are purely large, meso-, and submesoscale, $\bar{w}\bar{b} + w'b' + w''b''$, is not sufficient to explain the variability of the total wb, *i.e.* cross products among these terms also have a non-zero contribution. The two most dominant cross terms $w''\bar{b}$ and $w''b'$, together with three pure terms are compared to the total wb in Figure 3.11. It is seen that the seasonal variability in wb explained by the large scale $\bar{b}$ terms, whereas smaller variations are a combination of other terms involving the submesoscale w''.

Spatial distributions of the three purely large, meso-, and submesoscale terms compared with the total wb are given for an example simulation day in Figure 3.12. As described above, these three terms do not make up the total wb quantitatively, however, their spatial variability gives us a summary of what constitutes the features seen in wb, especially over the shelf. It is clear that the small scale variability in the inner shelf is

dominantly constituted by $w''b''$. $\bar{w}\bar{b}$ and $w'b'$ are significant at several localized regions very close to the coast but do not explain any specific pattern of the total wb for the rest of the shelf.

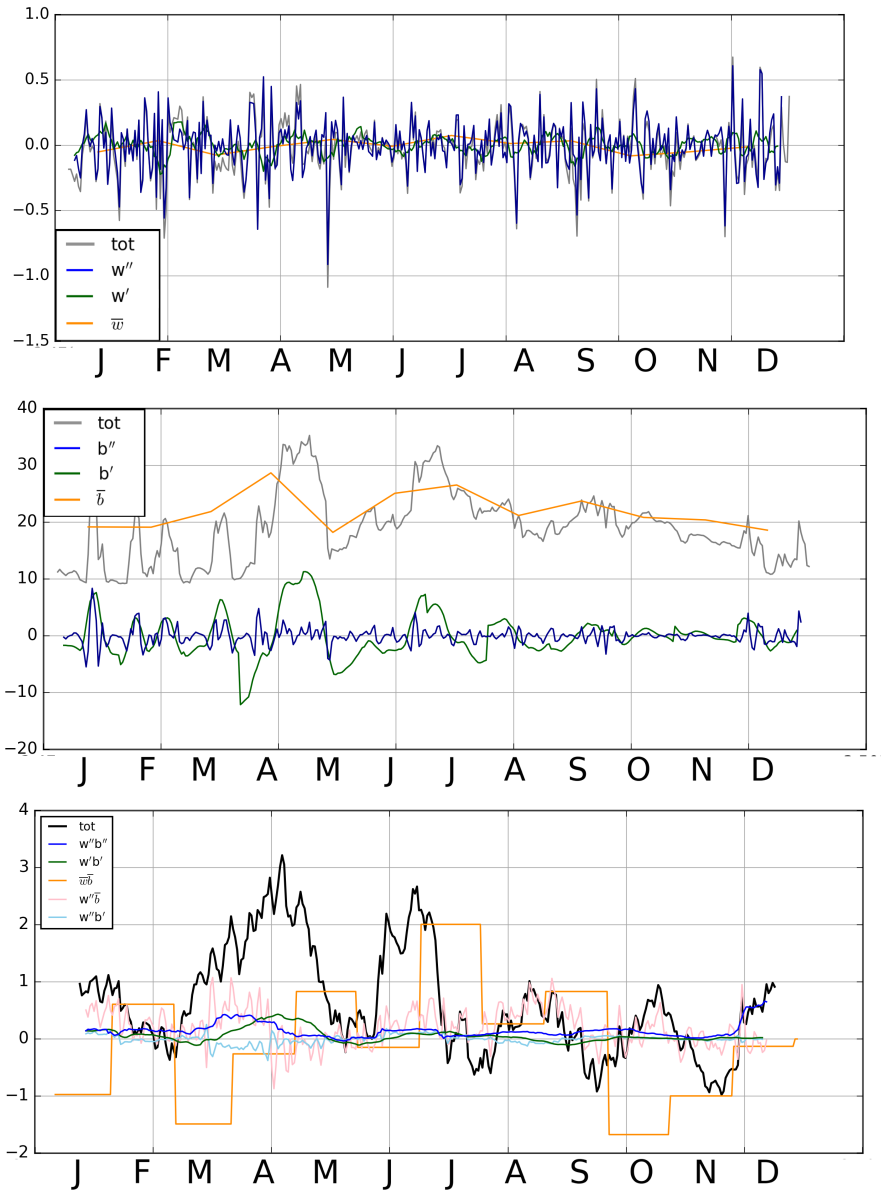

Figure 3.11: Modeled large, meso-, and submesoscale components of w (10^{-4} m s^{-1}) (top), b (10^{-3} m s^{-2}) (middle), and the comparison of the five most dominant wb (10^{-7} m^2 s^{-3}) terms to total wb (bottom), from 7 m depth, averaged over Loire subregion (Figure 3.1).

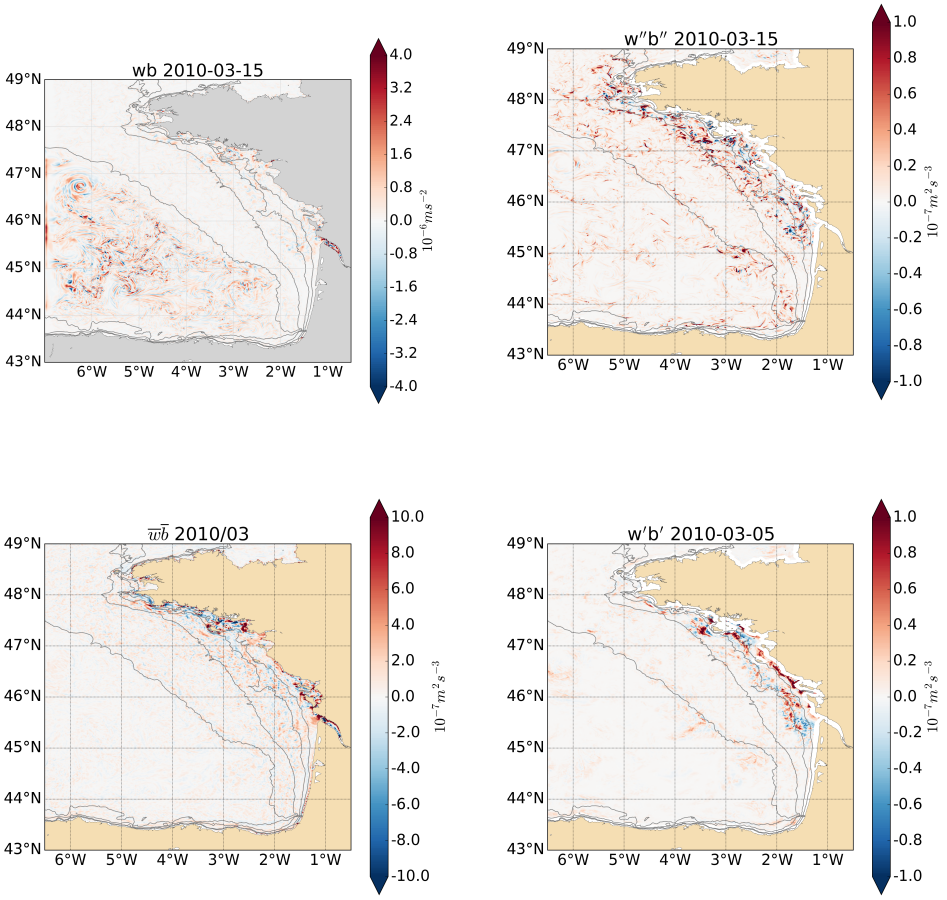

Figure 3.12: Examples of modeled large, meso-, submesoscale components, and total wb on 15/03/2010. The isolines represent the 30, 50, 125, 150, and 250 m isobaths.

3.3.2 Submesoscale Vertical Buoyancy Flux and Eddy Kinetic Energy

Monthly averaged distributions of $w''b''$ and EKE'' are given in this section. The purpose of these fields is to present the scales these parameters have over the shelf and the relation between their occurrence patterns. Therefore, to eliminate the noise, fields are averaged through the entire water column in the vertical and 32 times 5-point smoothed in the horizontal.

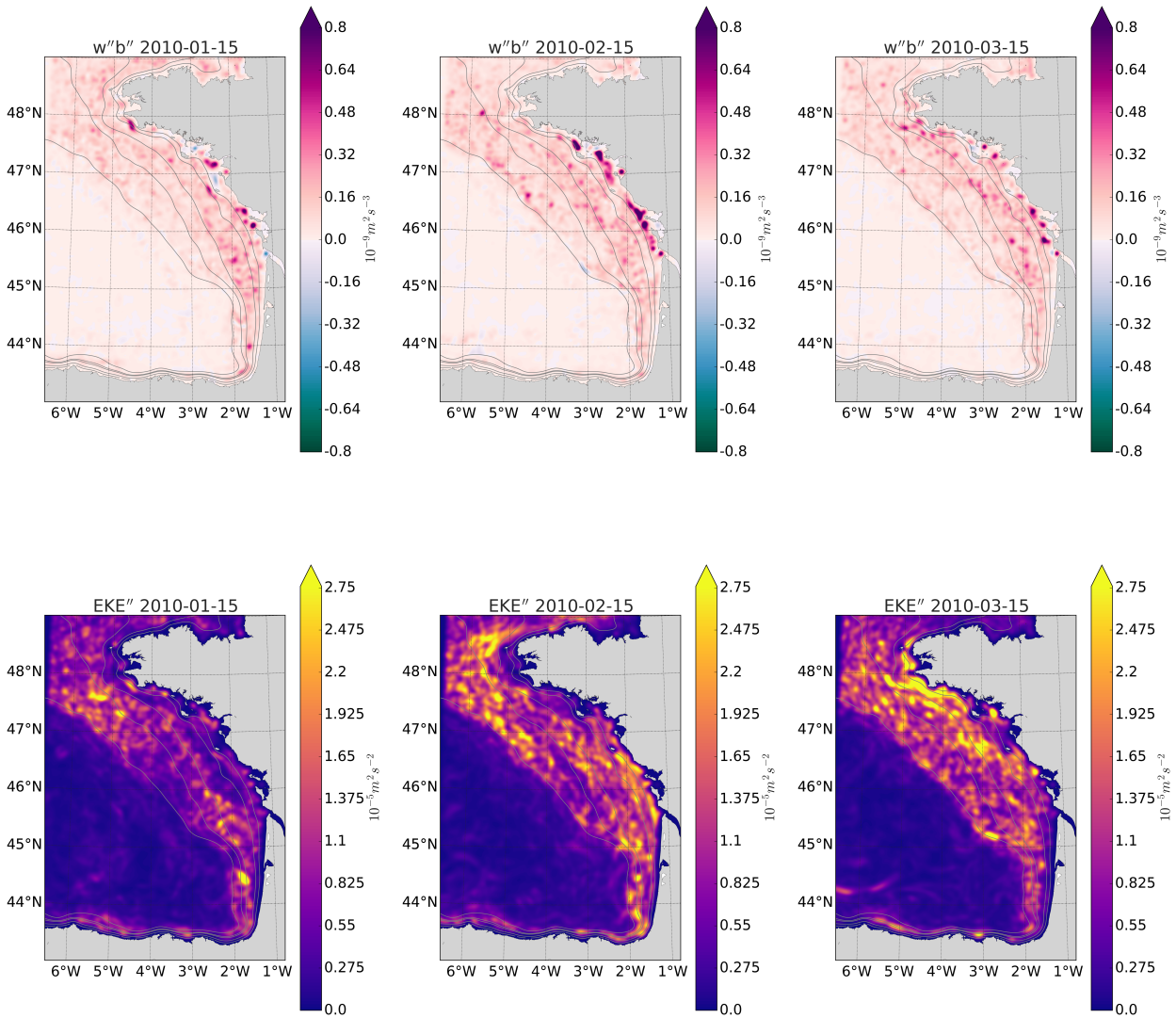

Figure 3.13: Vertically averaged submesoscale vertical buoyancy flux ($w''b''$ - top) and eddy kinetic energy (EKE'' - bottom) simulated in 2010 using the BOBF for the winter season (January-February-March). The isolines represent the 30, 50, 125, 150, and 250 m isobaths.

In winter (Figure 3.13), $w''b''$ is positive with larger values over the shelf than over the oceanic domain, especially inshore of the 100 m depth. In January, there are patches with markedly increased values along the coast at the north of Gironde estuary around Ile d'Oléron and Ile de Ré at 46N and 1.5W, further north around Ile d'Yeu, at the Loire estuary at 47N and 2.5W, and in the south of Brittany at 47.8N and 4.5W. Concerning the Eddy Kinetic Energy at submesoscale (EKE''), the intensity is also prominent over the continental shelf with large patches in front of Arcachon bay and Gironde estuary and along the coast inshore of the 50m isobath. In February, $w''b''$ values are larger than in the previous month with very prominent positive regions inshore of the 30m along the coast starting from Gironde following north up to 46.5N. Maximum values are observed in front of Loire and Vilaine, and north of Belle Ile. Similar patterns are observed in March with a decreasing intensity along the coast and the development of new patterns along the 100m isobath. The eddy kinetic energy (EKE'') in February increases also over the shelf and several spots appear, for example, west of Finistère offshore of the 100m isobath. Maxima are also observed along the coast from Gironde estuary up to Ile d'Yeu. In March, similar activity can be described with advected maxima south of Birttany, elongated patches along 100m north of 46.5N and two smaller structures at Vilaine et Ile d'Oléron.

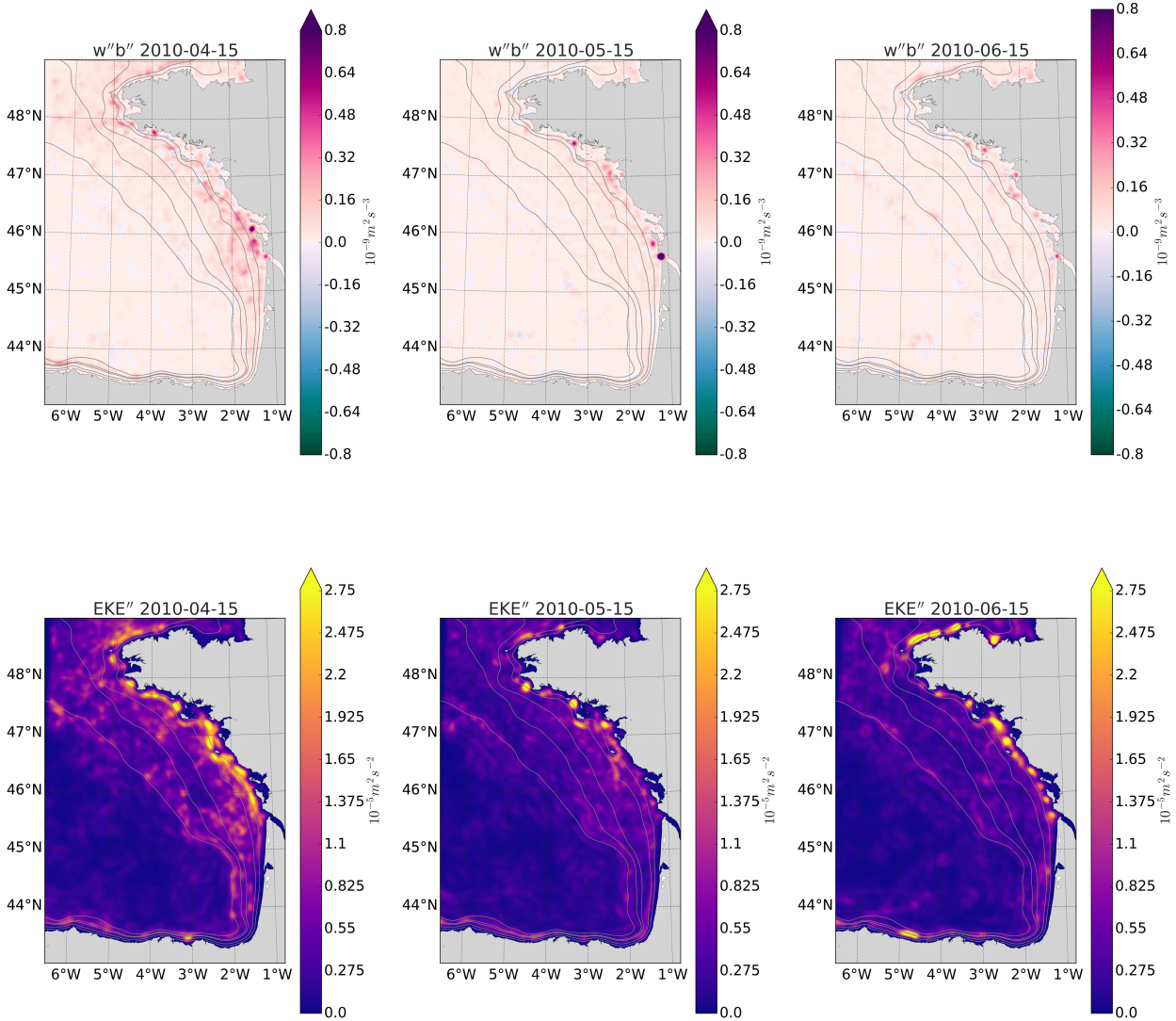

Figure 3.14: Vertically averaged submesoscale vertical buoyancy flux ($w''b''$ - top) and eddy kinetic energy (EKE'' - bottom) simulated in 2010 using the BOBF for the spring season (April-May-June). The isolines represent the 30, 50, 125, 150, and 250 m isobaths.

During spring, the buoyancy vertical flux decreases but remains mainly positive. In April (Figure 3.14), the region with the most intense value is located in front of the Gironde estuary along the coast and remains confined between the 30m-isobath and the coast. During the following months (May and June), the vertical buoyancy flux decreases and only very local intense spots remain visible (Gironde estuary and around Ile d'Oléron, in front of the Loire river in May). In the shelf break region, alternating patches can be observed. Furthermore, in front of the Loire and Vilaine rivers, negative values start to appear. The appearance of these new negative patterns denotes a transition in the dynamics (see Discussion). The EKE'' is coherent with the vertical buoyancy flux with a moderate intensity in April decreasing until June. Larger EKE'' values appears along the coast (even North of Brittany in June) and are also confined between the 30m isobath and the coast. Offshore, along the northern part of the shelf break, patterns with wavelike shapes start to appear.

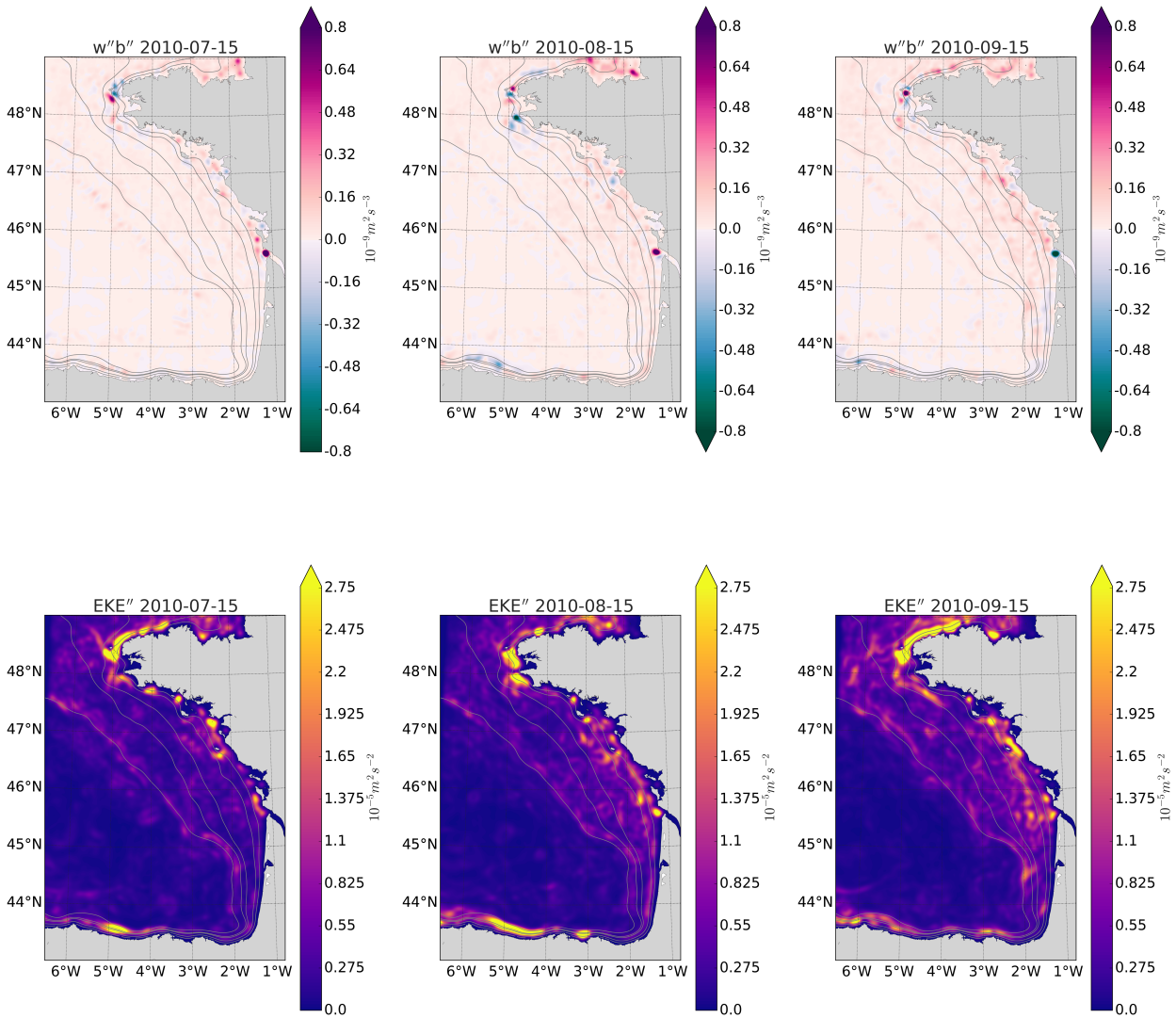

Figure 3.15: Vertically averaged submesoscale vertical buoyancy flux ($w''b''$ - top) and eddy kinetic energy (EKE'' - bottom) simulated in 2010 using the BOBF for the summer season (July-August-September). The isolines represent the 30, 50, 125, 150, and 250 m isobaths.

In summer (figure 3.15), the spatial distribution of the vertical buoyancy flux contrasts with previous months as several alternating (positive and negative) patches appears along the coast. West of Brittany, an intense dipole is developed around the Ushant island. Similar dipoles are detected around other islands (as Ile d'Oléron) but with a smaller amplitude. In the Ushant front region, positive and negative vertical fluxes are simulated and confined inshore the 50m isobath during August a. In front of the Lore estuary, fluxes are weaker and show some negative values unlike other seasons. An intense but localized spot is found in front of the Gironde estuary, which is positive in July - August but turns negative in September. Further south, negative values are observed along the northern Spanish coast over the narrow continental shelf. As expected, the eddy kinetic energy displays the highest values where the vertical buoyancy flux is largest. As a general overview, main EKE'' patterns are located in the Ushant front region west of Brittany, along the coast North of the Gironde estuary and along the Northern Spanish coast. An overall increased activity over the continental shelf is clearly simulated.

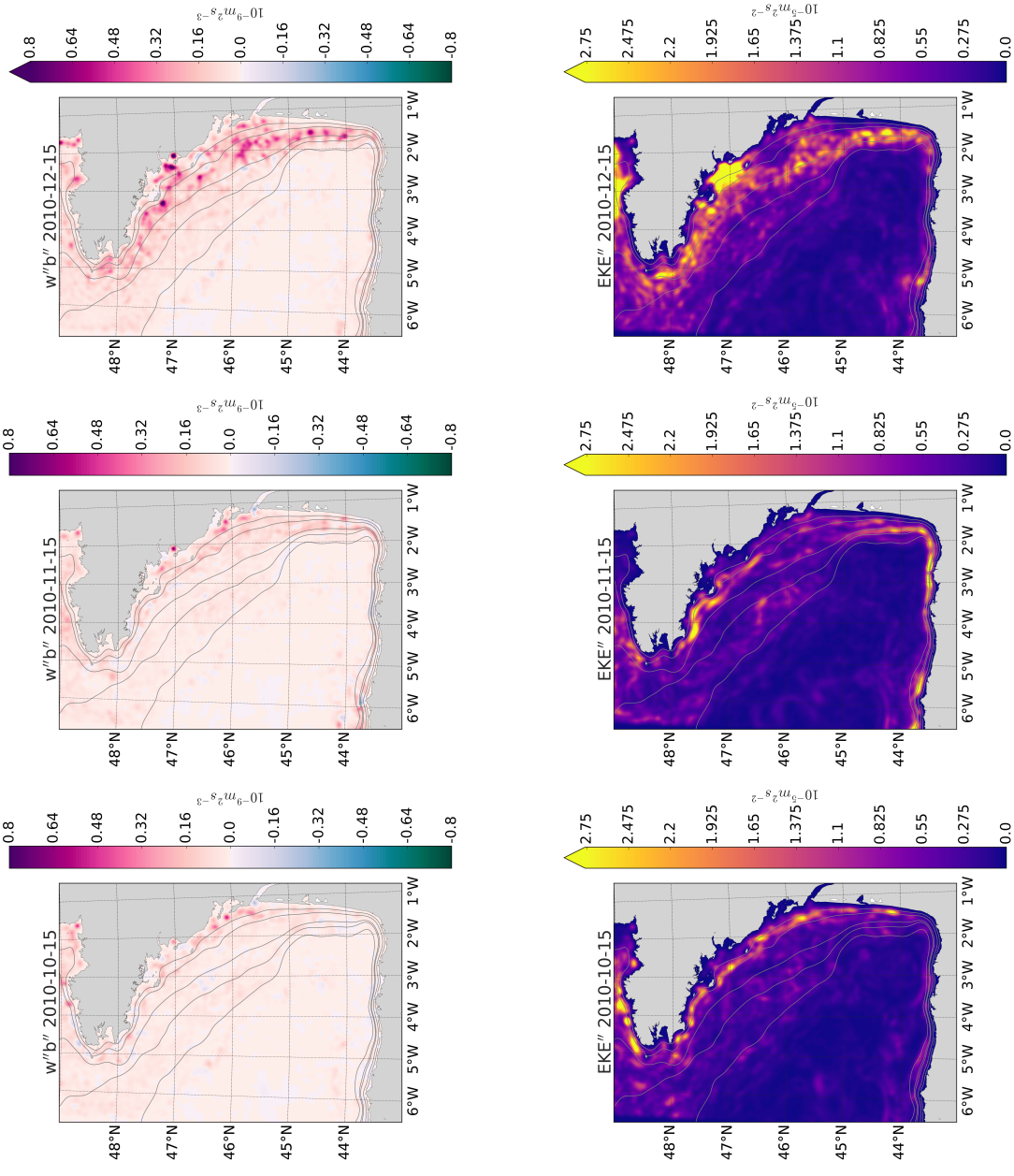

Figure 3.16: Vertically averaged submesoscale vertical buoyancy flux ($w''b''$ - top) and eddy kinetic energy (EKE'' - bottom) simulated in 2010 using the BOBF for the autumn season (October-November-December). The isolines represent the 30, 50, 125, 150, and 250 m isobaths.

During autumn (Figure 3.16), the transition between summer and winter occurs. In October and November, positive and negative $w''b''$ remain confined very close to the coast in waters shallower than 30 m depth, and positive patches increase over the shelf in December between the coast and the 100m isobath. The eddy kinetic energy follows the same trend with an activity more developed in December over the Aquitaine and Armorican shelves. Conversely, the Ushant front signal vanishes west of Brittany. The largest energies are simulated along the coast inshore of the 50m isobath as elongated patterns visible from October to November. In November, a signal also appears north of Spain. Maximum of the activity is reached in December inshore the 100m isobath with a large and increased patch close to Loire and Vilaine rivers.

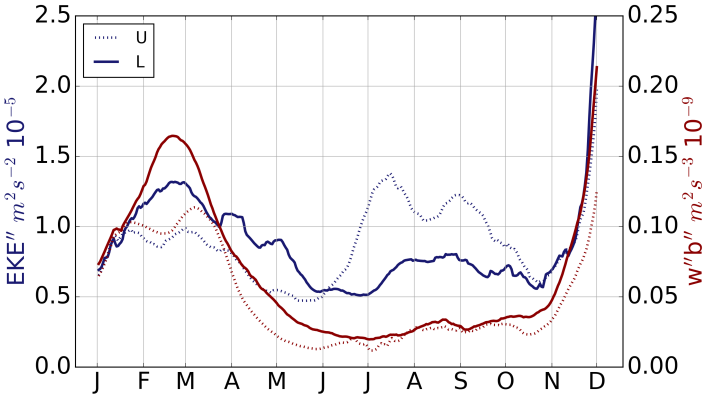

Figure 3.17: Climatology of vertically averaged EKE'' and $w''b''$ averaged over Loire and Ushant subregions (Figure 3.1).

The monthly evolution of the submesoscale vertical buoyancy flux and the eddy kinetic energy is given in Figure 3.17. In both of the regions, $w''b''$ and EKE'' peak in winter months. Although $w''b''$ is significantly larger in Loire region than in the Ushant region in winter, EKE'' shows no difference. Inversely, in summer $w''b''$ is similar for both regions but EKE'' in the Ushant region is larger than the Loire region.

Based on these distributions of buoyancy flux and eddy kinetic energy, processes involved in their occurrences are discussed in the following discussion section.

3.4 Discussion

The purpose of this chapter is to explain the evolution of the submesoscale dynamics over the Bay of Biscay continental shelf. Spatial and temporal distributions of wb, chosen as the main indicator of submesoscale activity, allow us to distinguish between regimes that are driven by a combination of different forcings. Based on the analysis of model experiments (and previous exploration of the frontal dynamics, see Chapter 2), the dynamics can be grouped under two dominant regimes one in winter and one in summer. Spring and autumn seasons, when one regime gradually transitions to the other, show characteristics of both regimes.

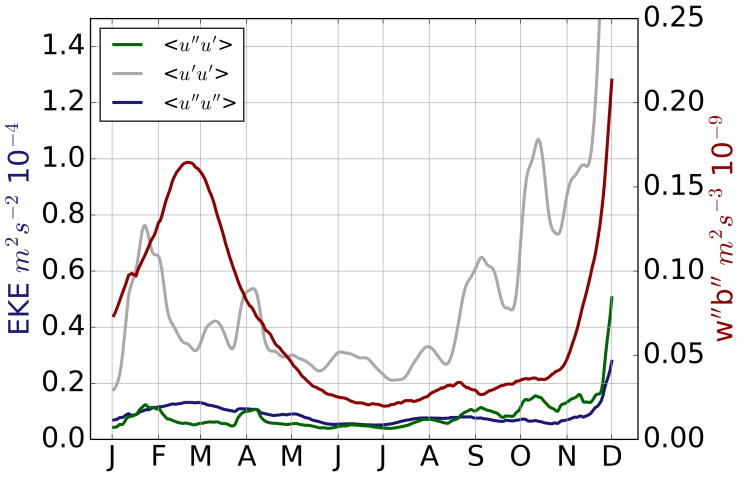

Figure 3.18: Climatology of vertically averaged $w''b''$ and components of EKE computed with velocities that are mesoscale (u'), submesoscale (u''), a combination of both ($u'u''$) averaged over Loire subregion (Figure 3.1).

As explained previously, our exploration of the submesoscale dynamics is based

on the assumption that baroclinic instability is the dominant process involved in its maintenance. Through restratification, Available Potential Energy (APE) is released as submesoscale Eddy Kinetic Energy (EKE'') during this process. However, it is not straightforward to determine which fraction of the EKE is produced by baroclinic instability among other processes. One way to obtain some indication is to determine over which time scale the conversion occurs. Let the submesoscale vertical buoyancy flux ($w''b''$) be a measure of APE to EKE conversion, then the rate of change of EKE is proportional to $w''b''$, *i.e.*,

$$\frac{\partial EKE}{\partial t} \approx w''b''. \tag{3.24}$$

The time scale T is then, $\frac{[EKE]}{[w''b'']}$. Different time scales can be computed for different components of the EKE, mesoscale EKE' or submesoscale EKE''. Occurrence of baroclinic instability and as a consequence the submesoscale energy conversion can be investigated by evaluating T, such that, for submesoscale processes T is in order of days, and longer for larger scales (Boccaletti et al., 2007). Figure 3.18 shows the temporal distributions of $w''b''$ and components of EKE computed with velocities that are mesoscale (u'), submesoscale (u''), a combination of both ($u'u''$) for the Loire region (see Figure 3.1). It shows that $\frac{[EKE']}{[w''b'']}$ is $\sim$ 3 - 30 days (*e.g.* minimum is around February - March, $\sim$ 3 days, for $EKE' \sim 0.4 \times 10^{-4} m^2 s^{-2}$ and $w''b'' \sim 0.16 \times 10^{-9} m^2 s^{-3}$, the maximum is around October - November, $\sim$ 30 days, for $EKE' \sim 1 \times 10^{-4} m^2 s^{-2}$ and $w''b'' \sim 0.04 \times 10^{-9} m^2 s^{-3}$). We consider this time scale longer than the submesoscales. Thus, in our discussion the focus is on exploring the relation between $w''b''$ and EKE'' (see section 3.3.2 for maps) for the Bay of Biscay shelf.

Winter

It is seen that positive $w''b''$ (geostrophic adjustment) occurs over the shelf especially more intensely at certain spots closer to the coast. We know that these spots are

along the density fronts formed by the edges of the combined plumes of Gironde and Loire rivers, as seen on Figure 3.3 salinity map. The mechanism that generates this density front is explained in Chapter 2 in detail. Basically, a combination of northward propagation of river discharge along the coast and SW onshore winds keeps the fresh water constrained along the coast. In the vertical, it occupies the upper $\sim$ 10 m.

As is, this density front may undergo unforced baroclinic instability. Additionally, the wintertime heat loss over the plume causes differential cooling of it, *i.e.* buoyancy loss at the lighter side of the front. This buoyancy loss, as it alters the density gradient, can disrupt a geostrophically balanced front and be responsible for triggering the instability.

The time scale over which the instability generates EKE'' is $\sim O(1)$day ($\sim$ 30 hours) in the vicinity of the Loire river (Figure 3.17). This rapid time scale confirms that this is a submesoscale process.

Existence of baroclinic instability in the vicinity of river plumes is argued by Hetland (2016). They suggest conditions for instabilities to occur depending on certain properties of the plume. They define a new parameter called the horizontal slope Burger number, S_H, such that $S_H = SRi^{-1/2} = Uf^{-1}W^{-1} = M^2 f^{-2}\alpha$, where S is the slope Burger number ($= Nf^{-1}\alpha$, N is the buoyancy frequency, f is the Coriolis parameter, α is the bottom slope), Ri is the Richardson number, U is the horizontal velocity scale, W is the plume width, M^2 is the horizontal buoyancy frequency ($= |\nabla_H b|$). They observe that instabilities occur when $S_H \lesssim 0.2$, which also implies the relation between the inertial length, $L_i = Uf^{-1}$, and W such that W should be wider than $5L_i$ for instabilities to grow. In the Bay of Biscay shelf these parameters for the region in front of the Loire river are $M^2 \sim 10^{-7}$ for the winter time plume, $f \sim 10^{-4}$, and $\alpha \sim 10^{-3}$, thus $S_H \sim 10^{-2}$, which satisfies the criteria for instabilities to occur. Also, starting from around December, when the plume is fully developed and occupy the inner shelf, it is $\sim$ 20 km

wide, **i.e.** much wider than $5L_i$ ($\sim 5 \times 10^{-1}$ m s^{-1}/10^{-4} s^{-1} $\sim$ 5 km).

Summer

The distribution of $w''b''$ in summer is significantly different than in winter. The signal of the plumes is no longer dominant, whereas along the coast intense spots of activity are visible. The locations of higher activity are the well known tidally active regions with very prominent tidal fronts in thermally stratified months (eg. Simpson and Hunter, 1974; Pingree and Griffiths, 1978; Le Boyer et al., 2009; Pasquet et al., 2012; Chevallier et al., 2014). Spots with consistently positive buoyancy flux can be explained by the occurrence of baroclinic instability, which has been reported to happen at tidal fronts (though, not necessarily in the submesoscale range) (Badin et al., 2009; Pasquet et al., 2012). At some of those spots (around islands and topographic obstacles) the $w''b''$ appears in alternating/dipole-like patterns. Dipole vortices (Morel and McWilliams, 1997, 2001) associated with baroclinic instability has been discussed for the Ushant tidal front by Pasquet et al. (2012).

Time scale of energy conversion in summer months is $\sim$ 3 days (Figure 3.17). This places such activity slightly closer to the upper limits of the submesoscale regime (Boccaletti et al., 2007), nevertheless it can be considered shorter than most mesoscale activity.

The seasonal behavior of submesoscale activity we describe above is the result of a combination of factors. First of all, there are the large scale forcings that set the background physical conditions that we termed above as winter and summer. The dominant winds in this region possess a two-mode seasonal signal of the large scale atmospheric forcings, termed "the SOMA effect" (meaning September-October and March-April) (Pingree et al., 1999). Winds are SW from October to March and NW from April to

September, *i.e.* onshore and downcoast, respectively, for the French coast line north of Gironde estuary. Similarly, the fresh water input from the Gironde and Loire rivers have a two-mode pattern throughout the year. They increase rapidly starting from October and their plumes are fully developed during winter until late spring, then they start diminishing and almost disappear in summer. Northern French continental shelf is also subject to large amplitude tidal forcings. Tidal mixing fronts along the coast are very prominent features of the summer months when the seasonal thermocline is established.

How seasonal conditions are giving rise to the submesoscale seasonality is discussed by previous studies. Realistic (Mensa et al., 2013; Sasaki et al., 2014; Capet et al., 2008a), and idealized (Brannigan et al., 2015) simulations find that submesoscale dynamics are more energetic in winter when large scale atmospheric forcings deepen the mixed layer and/or increase the lateral buoyancy gradients. Mensa et al. (2013) argues that, for the realistic simulations of the Gulf stream region, lateral gradients are present throughout the year, so the main driver of the submesoscale emergence is more likely to be the deep mixed layer that acts as a larger reservoir of APE and allows for more mixed layer instabilities than summer. (Brannigan et al., 2015) supports this by showing the increase of both the APE and the vertical buoyancy flux in winter that indicates the increase of overturning instabilities (like baroclinic instability) to be the primary submesoscale driver. Observations presented in Callies et al. (2015) from western subtropical North Atlantic, agreeing with the modeling studies, shows that the submesoscale flows are more energetic in the presence of a deeper mixed layer whereas mesoscale energy have less of a seasonality, which is in favor of the instability as the driver of the submesoscales rather than frontogenesis which only depends on mesoscale eddy field.

Chapter 4

Conclusions and Perspectives

Contents

4.1 Conclusions 109
4.2 Perspectives 112

4.1 Conclusions

This thesis study aims at exploring the submesoscale dynamics over the continental shelf in vicinity of main French rivers. Outcomes of the study are expected to shed light on the role of dynamics at this scale on the physics and biogeochemistry of the region.

The first step of the research is to identify and characterize submesoscale features over the shelf. For this purpose, remotely sensed high resolution images are considered as an optimal resource that allows for synoptic and long term observations. An 11-year dataset of remotely sensed SST by MODIS on Aqua and Terra satellites is constructed. To highlight the submesoscale features on these images a front detection algorithm is applied. The resulting dataset is analyzed spatially and temporally, and an index for quantifying the frontal activity, front occurrence probability, is generated. Seasonal maps and climatologies from selected regions of this index are produced. It is seen that

frontal activity varies greatly in space, and possess a particular seasonality depending on the region. Based on the investigation of the dominant physical drivers for regions that host increased frontal activity, we are able to distinguish the different types of fronts that occur over the French continental shelf.

The first identified type is the tidal mixing fronts that occur in thermally stratified months. They are observed along the coast and most significantly in the Ushant region offshore of western Brittany. This type of frontal activity is well-documented in our region and thus its dynamics is straightforward (*e.g.*, Simpson and Hunter 1974; Pingree and Griffiths 1978; Le Boyer et al. 2009). Another type of mixing front is observed along the continental shelf break. These fronts are the result of mixing due to internal tidal waves generated at the shelf break whose amplitude is large enough to reach above the thermocline. These fronts have been observed and explained previously (*e.g.*, Pairaud et al. 2010; New and Pingree 1990; Pichon and Correard 2006). Our study is the first one where the long term data and seasonal behavior of them are presented.

A second type of frontal activity is observed in the winter months along the edge of the fresh water plumes. They start appearing with the increase of the river discharge in mid-autumn, and are prominent all through winter. The fresh water entering the shelf propagates towards the north attached to the coast and is subject to downwelling winds typical of this season, thus a band of very low salinity water occupies the coast. The winter time heat loss is arrested by this lighter upper layer causing the plume to become colder than the surrounding shelf waters enabling us to observe them on the SST images. The density fronts at the edge of the plume are observed in this region previously (Puillat et al., 2004; Lazure et al., 2006), but their dynamics are not detailed. In our study we observe that they are the single most significant dynamical feature over the shelf in winter months, give an in-depth presentation of their spatial distribution and seasonality.

After the exploration via the observations has given us an overall picture of the frontal dynamics, the second step of the study is to analyze further and understand their submesoscale dynamics. A realistic hydrodynamical model of Bay of Biscay is set up. The model has a 1 km horizontal resolution and 40 σ vertical layers. It is forced with high resolution meteorological model outputs at the air-sea boundary, a larger scale OGCM at the open boundaries, and measured river discharge fluxes. A series of sensitivity test are performed to reach a reference simulation. It runs for two years as spin up and a third year for diagnostics. Its skill is assessed with respect to its ability to reproduce the observed frontal activity. It is shown that the results are in good agreement with observations. To distinguish between their large, meso-, and submesoscale components, a scale decomposition is applied to model parameters. A low pass filter first separates the large scale component and then a medium pass filter distinguishes the meso- and submesoscale components.

Our approach for model diagnostics is based on the idea that the submesoscale features in the upper ocean, generated at fronts, are a result of instability. Specifically, increased frontal activity at a density gradient is considered to be arising from the baroclinic instability. One indication of the occurrence of the baroclinic instability is the positive vertical buoyancy flux, as the isopycnals at a front slump such that the lighter water moves over the denser water. The spatial distributions of the submesoscale component of the buoyancy flux showed us clearly the regions where the instability might be occurring over the shelf. The other indication to assess whether these features are submesoscale in nature is the time scale over which they take place. The distinction between submesoscale instability and the mesoscale one is their time scales. Submesoscale instability characteristically occurs over rapid time scales in $O(1)$ day or less. Since baroclinic instability is a process that converts APE to EKE, we can consider that the time rate of change of EKE is going to be proportional to the produced buoyancy

flux. Thus, the ratio of the EKE to the buoyancy flux gives us the time scale that process takes. Because this is a scale analysis, instead of directly taking the ratio of the two quantities, we constructed monthly averaged, depth averaged, and horizontally smoothed maps of them. By doing so, we eliminated the noise signal, and are able to see the localized regions that consistently generate buoyancy flux.

The buoyancy flux and EKE maps show that, not surprisingly, the submesoscale dynamics have a pattern similar to the observed frontal occurrence. Activity increases in the Ushant region and the coastal regions in summer, whereas in winter activity in the vicinity of the fresh water plumes dominates.

In summer, dominant dynamic is the tidal fronts along the coast and the Ushant region. EKE conversion time scale in this season is $\sim$ 3 days, which can be considered shorter than mesoscale. Other than positive buoyancy flux regions, dipole like positive/negative alternating patterns are seen around topographic obstacles

In winter, we see the positive regions of buoyancy flux along the river plumes. They have a time scale of $O(1)$ day ($\sim$ 30 hours). This is a definite indicator that the submesoscale baroclinic instability is happening at the plume, which has been a topic of debate (Hetland, 2016). Another characteristic of winter time submesoscale dynamics is that they are very rapid, and convert more energy than in other seasons.

There are previous studies that also find that submesoscale dynamics are more active in winter compared to summer, and the explanation for this seasonality is suggested to be the larger reservoir of APE in the deeper mixed layer observed in winter.

4.2 Perspectives

While investigating the submesoscale dynamics in the Bay of Biscay shelf, this study also brings to attention further questions that will need to be addressed.

First of all, findings of this study suggest that fine scale dynamics are under the

influence of numerous drivers in complex physical environments such as continental shelves. For modeling studies like this one, realistic representation of these shelf dynamics, whose variability over scales -especially smaller ones- differ greatly from the open ocean, is very important. This study employs a numerical model that solves primitive equations under hydrostatic assumption with a 1 km horizontal resolution. It has become evident during the analyses of its results that a higher resolving capability for our region is much needed. Furthermore, the scale decomposition we apply to model results depends on distinguishing the submesoscales from the mesoscales. A 1 km resolution simulation's resolving limit ($\sim$ 6-8 km) is very close to the mesoscale - submesoscale distinction for the shelf regions, thus a higher resolution will allow for a more suitable filtering of the submesoscales.

Secondly, the most important implication of the submesoscale dynamics, and the motivation behind majority of the studies in this field, is their impact on the distribution of biogeochemical properties. The review of several studies on this issue by Klein and Lapeyre (2009), comes to the conclusion that submesoscale vertical exchanges are the key physical component to explain fully the ocean nutrient budget. Submesoscale vertical dynamics not only enhance production by bringing nutrients to the sun-lit upper ocean, but also increase the light exposure of phytoplankton through restratification by shallow baroclinic instability (Mahadevan, 2016). There are several modeling studies that explore the biological impact with idealized open ocean cases (*e.g.*, Lévy et al. 2012a,b). Our study shows that Bay of Biscay inner shelf is actively producing submesoscale vertical fluxes, especially in the vicinity of the river plumes. Furthering our analysis towards exploring the role of this submesoscale activity in the fate of the nutrients and in the distribution of buoyant organisms will contribute greatly to the understanding of biological activity in such regions.

Bibliography

Acha, E. M., Mianzan, H. W., Guerrero, R. A., Favero, M., and Bava, J. (2004). Marine fronts at the continental shelves of austral South America. *Journal of Marine Systems*, 44(1-2):83–105. (Cited on page 17.)

Albaina, A. and Irigoien, X. (2004). Relationships between frontal structures and zooplankton communities along a cross-shelf transect in the Bay of Biscay(1995 to 2003). *Marine Ecology Progress Series*, 284(65-75). (Cited on page 18.)

Arakawa, A. and Lamb, V. R. (1977). Computational design of the basic dynamical processes of the UCLA general circulation model. *Methods in computational physics*, 17:173–265. (Cited on page 62.)

Arneodo, A., Audit, B., Bacry, E., Manneville, S., Muzy, J. F., and Roux, S. G. (1998). Thermodynamics of fractal signals based on wavelet analysis: application to fully developed turbulence data and DNA sequences. *Physica A: Statistical Mechanics and its Applications*, 254(1–2):24–45. (Cited on page 25.)

Badin, G., Williams, R. G., Holt, J. T., and Fernand, L. J. (2009). Are mesoscale eddies in shelf seas formed by baroclinic instability of tidal fronts? *Journal of Geophysical Research*, 114(C10). (Cited on page 106.)

Baines, P. G. (1982). On internal tide generation models. *Deep Sea Research Part A. Oceanographic Research Papers*, 29(3):307–338. (Cited on page 54.)

Batifoulier, F., Lazure, P., and Bonneton, P. (2012). Poleward coastal jets induced by westerlies in the Bay of Biscay. *Journal of Geophysical Research: Oceans*, 117(C3). (Cited on page 4.)

Batifoulier, F., Lazure, P., Velo-Suarez, L., Maurer, D., Bonneton, P., Charria, G., Dupuy, C., and Gentien, P. (2013). Distribution of dinophysis species in the bay of biscay and possible transport pathways to arcachon bay. *Journal of Marine Systems*, 109–110, Supplement:S273 – S283. XII International Symposium on Oceanography of the Bay of Biscay. (Cited on page 4.)

Belkin, I. M., Cornillon, P. C., and Sherman, K. (2009). Fronts in Large Marine Ecosystems. *Progress in Oceanography*, 81(1–4):223–236. (Cited on page 17.)

Berger, H., Dumas, F., Petton, S., and Lazure, P. (2014). Evaluation of the hydrology and dynamics of the operational mars3d configuration of the bay of Biscay. *Mercator Ocean Newsletter*, 49. (Cited on page 20.)

Boccaletti, G., Ferrari, R., and Fox-Kemper, B. (2007). Mixed Layer Instabilities and Restratification. *Journal of Physical Oceanography*, 37(9):2228–2250. (Cited on pages 11, 12, 104 and 106.)

Bowers, D. G. and Simpson, J. H. (1987). Mean position of tidal fronts in European-shelf seas. *Continental Shelf Research*, 7(1):35–44. (Cited on pages 17 and 51.)

Brannigan, L., Marshall, D. P., Naveira-Garabato, A., and George Nurser, A. J. (2015). The seasonal cycle of submesoscale flows. *Ocean Modelling*, 92:69–84. (Cited on page 107.)

Burchard, H. and Petersen, O. (1999). Models of turbulence in the marine environment – a comparative study of two–equation turbulence models. *Journal of Marine Systems*, 21(1):29–53. (Cited on page 67.)

Callies, J., Ferrari, R., Klymak, J. M., and Gula, J. (2015). Seasonality in submesoscale turbulence. *Nature Communications*, 6:6862. (Cited on page 107.)

Canuto, V. M., Howard, A., Cheng, Y., and Dubovikov, M. (2001). Ocean turbulence. part i: One–point closure model – momentum and heat vertical diffusivities. *Journal of Physical Oceanography*, 31(6):1413–1426. (Cited on page 67.)

Capet, X., Campos, E. J., and Paiva, A. M. (2008a). Submesoscale activity over the Argentinian shelf. *Geophysical Research Letters*, 35(15). (Cited on pages 12, 58, 62 and 107.)

Capet, X., McWilliams, J. C., Molemaker, M. J., and Shchepetkin, A. F. (2008b). Mesoscale to Submesoscale Transition in the California Current System. Part I: Flow Structure, Eddy Flux, and Observational Tests. *Journal of Physical Oceanography*, 38(1):29–43. (Cited on page 89.)

Chapman, D. C. and Lentz, S. J. (1994). Trapping of a Coastal Density Front by the Bottom Boundary Layer. *Journal of Physical Oceanography*, 24(7):1464–1479. (Cited on pages 45, 47, 48 and 57.)

Charria, G., Lazure, P., Le Cann, B., Serpette, A., Reverdin, G., Louazel, S., Batifoulier, F., Dumas, F., Pichon, A., and Morel, Y. (2013). Surface layer circulation derived from Lagrangian drifters in the Bay of Biscay. *Journal of Marine Systems*, 109-110:S60–S76. (Cited on page 2.)

Charria, G., Repecaud, M., Quemener, L., Menesguen, A., Rimmelin-Maury, P., L'Helguen, S., Beaumont, L., Jolivet, A., Morin, P., Mace, E., Lazure, P., Le Gendre, R., Jacqueline, F., Verney, R., Marie, L., Jegou, P., Le Reste, S., Andre, X., Dutreuil, V., Regnault, J.-P., Jestin, H., Lintanf, H., Pichavant, P., Retho, M., Allenou, J.-P., Stanisiere, J.-Y., Bonnat, A., Nonnotte, L., Duros, W., Tarot, S., Carval, T., Le Hir, P., Dumas, F., Vandermeirsch, F., and Lecornu, F. (2014). PREVIMER: A contribution to in situ coastal observing systems. *Mercator Ocean - Quaterly Newsletter*, 49:9–20. (Cited on page 21.)

Charria, G., Theetten, S., Vandermeirsch, F., Yelekci, O., and Audiffren, N. (Manuscript submitted for publication. 2017). Interannual evolutions of (sub)mesoscale dynamics in the Bay of Biscay, ocean sci. discuss. (Cited on page 69.)

Chelton, D. B., deSzoeke, R. A., Schlax, M. G., El Naggar, K., and Siwertz, N. (1998). Geographical Variability of the First Baroclinic Rossby Radius of Deformation. *Journal of Physical Oceanography*, 28(3):433–460. (Cited on page 10.)

Chevallier, C., Herbette, S., Marié, L., Le Borgne, P., Marsouin, A., Péré, S., Levier, B., and Reason, C. (2014). Observations of the Ushant front displacements with MSG/SEVIRI derived sea surface temperature data. *Remote Sensing of Environment*, 146:3–10. (Cited on pages 51 and 106.)

Cyr, F. and Larouche, P. (2014). Thermal Fronts Atlas of Canadian Coastal Waters. *Atmosphere-Ocean*, 0(0):1–25. (Cited on page 17.)

D'Asaro, E., Lee, C., Rainville, L., Harcourt, R., and Thomas, L. (2011). Enhanced Turbulence and Energy Dissipation at Ocean Fronts. *Science*, 332(6027):318–322. (Cited on page 16.)

Demerliac, A. (1973). Le niveau moyen de la mer. Calcul du niveau moyen journalien. *Rapport du SHOM*. (Cited on page 21.)

Déqué, M., Dreveton, C., Braun, A., and Cariolle, D. (1994). The ARPEGE/IFS atmosphere model: a contribution to the french community climate modelling. *Climate Dynamics*, 10(4-5):249–266. (Cited on pages 20 and 69.)

Duhaut, T., Honnorat, M., and Debreu, L. (2008). Développements numériques pour le modèle MARS. *PREVIMER report-Ref: 06/2 210*, 290. (Cited on page 20.)

Dumas, F., Pineau-Guillou, L., Lecornu, F., Le Roux, J.-F., and Le Squere, B. (2014).

General Introduction: PREVIMER, a French pre-operational coastal ocean forecasting capability. *Mercator Ocean-Quarterly Newsletter*, (49):3–8. (Cited on page 20.)

Fernández, E., Cabal, J., Acuña, J. L., Bode, A., Botas, A., and García-Soto, C. (1993). Plankton distribution across a slope current-induced front in the southern Bay of Biscay. *Journal of Plankton Research*, 15(6):619–641. (Cited on page 18.)

Ferrari, R. (2011). A Frontal Challenge for Climate Models. *Science*, 332(6027):316–317. (Cited on page 16.)

Galperin, B., Kantha, L., Hassid, S., and Rosati, A. (1988). A quasi–equilibrium turbulent energy model for geophysical flows. *Journal of the Atmospheric Sciences*, 45(1):550–62. (Cited on page 67.)

Haine, T. W. N. and Marshall, J. (1998). Gravitational, Symmetric, and Baroclinic Instability of the Ocean Mixed Layer. *Journal of Physical Oceanography*, 28(4):634–658. (Cited on page 12.)

Hedström, K. S. (1994). *Technical manual for a coupled sea-ice/ocean circulation model (version 1)*. Minerals Management Service, Alaska OCS Region. (Cited on page 63.)

Hetland, R. D. (2010). The effects of mixing and spreading on density in near-field river plumes. *Dynamics of Atmospheres and Oceans*, 49(1):37–53. (Cited on page 58.)

Hetland, R. D. (2016). Suppression of Baroclinic Instabilities in Buoyancy-Driven Flow over Sloping Bathymetry. *Journal of Physical Oceanography*, 47(1):49–68. (Cited on pages 12, 58, 62, 105 and 112.)

Hickox, R., Belkin, I., Cornillon, P., and Shan, Z. (2000). Climatology and seasonal variability of ocean fronts in the East China, Yellow and Bohai seas from satellite SST data. *Geophysical Research Letters*, 27(18):2945–2948. (Cited on page 17.)

Huang, D., Zhang, T., and Zhou, F. (2010). Sea-surface temperature fronts in the Yellow and East China Seas from TRMM microwave imager data. *Deep Sea Research Part II: Topical Studies in Oceanography*, 57(11):1017–1024. (Cited on page 17.)

Kantha, L. H. and Clayson, C. A. (1994). An improved mixed layer model for geophysical applications. *Journal of Geophysical Research: Oceans*, 99(C12):25235–25266. (Cited on page 67.)

Ker, S., Le Gonidec, Y., and Marié, L. (2016). Multifrequency seismic detectability of seasonal thermoclines assessed from ARGO data. *Journal of Geophysical Research: Oceans*, 121(8):6035–6060. (Cited on page 5.)

Kersalé, M., Marié, L., Cann, B. L., Serpette, A., Lathuilière, C., Boyer, A. L., Rubio, A., and Lazure, P. (2016). Poleward along-shore current pulses on the inner shelf of the Bay of Biscay. *Estuarine, Coastal and Shelf Science*, 179:155 – 171. (Cited on pages 3 and 4.)

Klein, P. and Lapeyre, G. (2009). The oceanic vertical pump induced by mesoscale and submesoscale turbulence. *Annual Review of Marine Science*, 1:351–375. (Cited on page 113.)

Koutsikopoulos, C. and Le Cann, B. (1996). Physical processes and hydrological structures related to the Bay of Biscay anchovy. *Scientia Marina*, 60:9–19. (Cited on pages ix, 2, 3, 4 and 5.)

Lamouroux, J., Charria, G., De Mey, P., Raynaud, S., Heyraud, C., Craneguy, P., Dumas, F., and Le Hénaff, M. (2016). Objective assessment of the contribution of the RECOPESCA network to the monitoring of 3d coastal ocean variables in the Bay of Biscay and the English Channel. *Ocean Dynamics*, 66(4):567–588. (Cited on pages 22 and 79.)

Lazure, P. and Dumas, F. (2008). An external–internal mode coupling for a 3D hydrodynamical model for applications at regional scale (MARS). *Advances in Water Resources*, 31(2):233–250. (Cited on pages 20 and 62.)

Lazure, P., Dumas, F., and Vrignaud, C. (2008). Circulation on the Armorican shelf (Bay of Biscay) in autumn. *Journal of Marine Systems*, 72(1-4):218–237. (Cited on page 46.)

Lazure, P. and Jégou, A.-M. (1998). 3D modelling of seasonal evolution of Loire and Gironde plumes on Biscay Bay continental shelf. *Oceanologica Acta*, 21(2):165–177. (Cited on pages 4 and 47.)

Lazure, P., Jégou, A.-M., and Kerdreux, M. (2006). Analysis of salinity measurements near islands on the French continental shelf of the Bay of Biscay. *Scientia Marina*, 70(1):7–14. (Cited on pages 2, 45 and 110.)

Le Borgne, P., Roquet, H., and Merchant, C. J. (2011). Estimation of sea surface temperature from the Spinning Enhanced Visible and Infrared Imager, improved using numerical weather prediction. *Remote Sensing of Environment*, 115(1):55–65. (Cited on page 21.)

Le Boyer, A., Cambon, G., Daniault, N., Herbette, S., Le Cann, B., Marié, L., and Morin, P. (2009). Observations of the Ushant tidal front in September 2007. *Continental Shelf Research*, 29(8):1026–1037. (Cited on pages 3, 51, 106 and 110.)

Le Cann, B. (1990). Barotropic tidal dynamics of the Bay of Biscay shelf: observations, numerical modelling and physical interpretation. *Continental Shelf Research*, 10(8):723–758. (Cited on page 3.)

Le Cann, B. and Serpette, A. (2009). Intense warm and saline upper ocean inflow in

the southern Bay of Biscay in autumn-winter 2006-2007. *Continental Shelf Research*, 29(8):1014–1025. (Cited on page 46.)

Leblond, E., Lazure, P., Laurans, M., Rioual, C., Woerther, P., Quemener, L., and Berthou, P. (2010). The Recopesca Project : a new example of participative approach to collect fisheries and in situ environmental data. *CORIOLIS Quarterly Newsletter*, (37):40–48. (Cited on pages 21 and 79.)

Leonard, B. P., Lock, A. P., and MacVean, M. K. (1996). Conservative explicit unrestricted-time-step multidimensional constancy-preserving advection schemes. *Monthly Weather Review*, 124(11):2588–2606. (Cited on page 20.)

Lévy, M., Ferrari, R., Franks, P. J. S., Martin, A. P., and Rivière, P. (2012a). Bringing physics to life at the submesoscale: FRONTIER. *Geophysical Research Letters*, 39(14). (Cited on page 113.)

Lévy, M., Iovino, D., Resplandy, L., Klein, P., Madec, G., Tréguier, A.-M., Masson, S., and Takahashi, K. (2012b). Large-scale impacts of submesoscale dynamics on phytoplankton: Local and remote effects. *Ocean Modelling*, 43-44:77–93. (Cited on page 113.)

Lévy, M., Klein, P., and Treguier, A.-M. (2001). Impact of sub-mesoscale physics on production and subduction of phytoplankton in an oligotrophic regime. *Journal of Marine Research*, 59(4):535–565. (Cited on page 16.)

Luyten, P. J., Deleersnijder, E., Ozer, J., and Ruddick, K. G. (1996). Presentation of a family of turbulence closure models for stratified shallow water flows and preliminary application to the Rhine outflow region. *Continental Shelf Research*, 16(1):101–130. (Cited on page 66.)

Lyard, F., Lefevre, F., Letellier, T., and Francis, O. (2006). Modelling the global ocean tides: modern insights from FES2004. *Ocean Dynamics*, 56(5-6):394–415. (Cited on page 20.)

Mahadevan, A. (2016). The Impact of Submesoscale Physics on Primary Productivity of Plankton. *Annual Review of Marine Science*, 8(1). (Cited on pages 58 and 113.)

Maji, K. S. and Yahia, H. M. (2014). Edges, transitions and criticality. *Pattern Recognition*, 47(6):2104–2115. (Cited on page 26.)

Maji, S. K., Pont, O., Yahia, H., and Sudre, J. (2013). Inferring Information Across Scales in Acquired Complex Signals. In Gilbert, T., Kirkilionis, M., and Nicolis, G., editors, *Proceedings of the European Conference on Complex Systems 2012*, Springer Proceedings in Complexity, pages 209–226. Springer International Publishing. (Cited on pages 25 and 26.)

Marchesiello, P., Capet, X., Menkes, C., and Kennan, S. C. (2011). Submesoscale dynamics in tropical instability waves. *Ocean Modelling*, 39(1–2):31–46. (Cited on page 62.)

Mariette, V. and Le Cann, B. (1985). Simulation of the formation of Ushant thermal front. *Continental Shelf Research*, 4(6):637–660. (Cited on page 51.)

McGillicuddy, D. J., Anderson, L. A., Bates, N. R., Bibby, T., Buesseler, K. O., Carlson, C. A., Davis, C. S., Ewart, C., Falkowski, P. G., Goldthwait, S. A., Hansell, D. A., Jenkins, W. J., Johnson, R., Kosnyrev, V. K., Ledwell, J. R., Li, Q. P., Siegel, D. A., and Steinberg, D. K. (2007). Eddy/Wind Interactions Stimulate Extraordinary Mid-Ocean Plankton Blooms. *Science*, 316(5827):1021–1026. (Cited on page 16.)

McGillicuddy, D. J., Robinson, A. R., Siegel, D. A., Jannasch, H. W., Johnson, R., Dickey, T. D., McNeil, J., Michaels, A. F., and Knap, A. H. (1998). Influence of

mesoscale eddies on new production in the Sargasso Sea. *Nature*, 394(6690):263–266. (Cited on page 16.)

Mellor, G. L. and Yamada, T. (1982). Development of a turbulence closure model for geophysical fluid problems. *Reviews of Geophysics*, 20(4):851–875. (Cited on page 67.)

Mensa, J. A., Garraffo, Z., Griffa, A., Özgökmen, T. M., Haza, A., and Veneziani, M. (2013). Seasonality of the submesoscale dynamics in the Gulf Stream region. *Ocean Dynamics*, 63(8):923–941. (Cited on pages 62 and 107.)

Molemaker, M. J., Mcwilliams, J. C., and Capet, X. (2010). Balanced and unbalanced routes to dissipation in an equilibrated Eady flow. *Journal of Fluid Mechanics*, 654:35–63. (Cited on page 12.)

Molines, J. M., Barnier, B., Penduff, T., Treguier, A. M., and J, L. S. (2014). ORCA12.L46 climatological and interannual simulations forced with DFS4.4: GJM02 and MJM88. *The DRAKKAR Group, Experiment report LGGE-DRA*. (Cited on page 70.)

Morel, Y. and McWilliams, J. (1997). Evolution of Isolated Interior Vortices in the Ocean. *Journal of Physical Oceanography*, 27(5):727–748. (Cited on page 106.)

Morel, Y. and McWilliams, J. (2001). Effects of isopycnal and diapycnal mixing on the stability of oceanic currents. *Journal of physical oceanography*, 31(8):2280–2296. (Cited on page 106.)

Munk, W., Armi, L., Fischer, K., and Zachariasen, F. (2000). Spirals on the sea. *Proceedings of the Royal Society of London A: Mathematical, Physical and Engineering Sciences*, 456(1997):1217–1280. (Cited on page 1.)

New, A. L. (1988). Internal tidal mixing in the Bay of Biscay. *Deep Sea Research Part A. Oceanographic Research Papers*, 35(5):691–709. (Cited on page 54.)

New, A. L. and Pingree, R. D. (1990). Evidence for internal tidal mixing near the shelf break in the Bay of Biscay. *Deep Sea Research Part A. Oceanographic Research Papers*, 37(12):1783–1803. (Cited on pages 54 and 110.)

Oey, L.-Y. (1986). The Formation and Maintenance of Density Fronts on the U.S. Southeastern Continental Shelf during Winter. *Journal of Physical Oceanography*, 16(6):1121–1135. (Cited on page 17.)

Oschlies, A. and Garçon, V. (1998). Eddy-induced enhancement of primary production in a model of the North Atlantic Ocean. *Nature*, 394(6690):266–269. (Cited on page 16.)

Otero, P., Ruiz-Villarreal, M., and Peliz, A. (2009). River plume fronts off NW Iberia from satellite observations and model data. *ICES Journal of Marine Science: Journal du Conseil*. (Cited on page 17.)

Owen, R. W. (1981). Fronts and eddies in the sea: mechanisms, interactions and biological effects. *Analysis of marine ecosystems*, pages 197–233. (Cited on page 16.)

Pairaud, I. L., Auclair, F., Marsaleix, P., Lyard, F., and Pichon, A. (2010). Dynamics of the semi-diurnal and quarter-diurnal internal tides in the Bay of Biscay. Part 2: Baroclinic tides. *Continental Shelf Research*, 30(3–4):253–269. (Cited on pages 54 and 110.)

Pasquet, A., Szekely, T., and Morel, Y. (2012). Production and dispersion of mixed waters in stratified coastal areas. *Continental Shelf Research*, 39–40:49–77. (Cited on pages 51 and 106.)

Pichon, A. and Correard, S. (2006). Internal tides modelling in the Bay of Biscay. Comparisons with observations. *Scientia Marina*, 70(S1):65–88. (Cited on pages 54 and 110.)

Pichon, A. and Mazé, R. (1990). Internal Tides over a Shelf Break: Analytical Model and Observations. *Journal of Physical Oceanography*, 20(5):657–671. (Cited on page 54.)

Pingree, R. D. and Griffiths, D. K. (1978). Tidal fronts on the shelf seas around the British Isles. *Journal of Geophysical Research: Oceans*, 83(C9):4615–4622. (Cited on pages 51, 106 and 110.)

Pingree, R. D., Griffiths, D. K., and Mardell, G. T. (1984). The Structure of the Internal Tide at the Celtic Sea Shelf Break. *Journal of the Marine Biological Association of the United Kingdom*, 64(01):99–113. (Cited on page 54.)

Pingree, R. D. and Le Cann, B. (1989). Celtic and Armorican slope and shelf residual currents. *Progress in Oceanography*, 23(4):303–338. (Cited on pages 3 and 4.)

Pingree, R. D., Mardell, G. T., and Cartwright, D. E. (1981). Slope Turbulence, Internal Waves and Phytoplankton Growth at the Celtic Sea Shelf-Break [and Discussion]. *Philosophical Transactions of the Royal Society of London A: Mathematical, Physical and Engineering Sciences*, 302(1472):663–682. (Cited on pages 54 and 55.)

Pingree, R. D., Mardell, G. T., Holligan, P. M., Griffiths, D. K., and Smithers, J. (1982). Celtic Sea and Armorican current structure and the vertical distributions of temperature and chlorophyll. *Continental Shelf Research*, 1(1):99–116. (Cited on page 3.)

Pingree, R. D. and New, A. L. (1995). Structure, seasonal development and sunglint spatial coherence of the internal tide on the Celtic and Armorican shelves and in the Bay of Biscay. *Deep Sea Research Part I: Oceanographic Research Papers*, 42(2):245–284. (Cited on page 54.)

Pingree, R. D., Sinha, B., and Griffiths, C. R. (1999). Seasonality of the European slope current (Goban Spur) and ocean margin exchange. *Continental Shelf Research*, 19(7):929–975. (Cited on pages 2, 4 and 106.)

Pont, O., Turiel, A., and Yahia, H. (2011). An Optimized Algorithm for the Evaluation of Local Singularity Exponents in Digital Signals. In Aggarwal, J. K., Barneva, R. P., Brimkov, V. E., Koroutchev, K. N., and Korutcheva, E. R., editors, *Combinatorial Image Analysis*, number 6636 in Lecture Notes in Computer Science, pages 346–357. Springer Berlin Heidelberg. (Cited on page 25.)

Puillat, I., Lazure, P., Jégou, A., Lampert, L., and Miller, P. (2004). Hydrographical variability on the French continental shelf in the Bay of Biscay, during the 1990s. *Continental Shelf Research*, 24(10):1143–1163. (Cited on pages 2, 4, 45, 47 and 110.)

Puillat, I., Lazure, P., Jegou, A.-M., Lampert, L., and Miller, P. (2006). Mesoscale hydrological variability induced by northwesterly wind on the French continental shelf of the Bay of Biscay. *Scientia Marina*, 70(S1):15–26. (Cited on pages 4 and 47.)

Rosso, I., Hogg, A. M., Kiss, A. E., and Gayen, B. (2015). Topographic influence on submesoscale dynamics in the Southern Ocean. *Geophysical Research Letters*, 42(4):2014GL062720. (Cited on page 62.)

Rosso, I., Hogg, A. M., Strutton, P. G., Kiss, A. E., Matear, R., Klocker, A., and van Sebille, E. (2014). Vertical transport in the ocean due to sub-mesoscale structures: Impacts in the Kerguelen region. *Ocean Modelling*, 80:10–23. (Cited on page 62.)

Sasaki, H., Klein, P., Qiu, B., and Sasai, Y. (2014). Impact of oceanic-scale interactions on the seasonal modulation of ocean dynamics by the atmosphere. *Nature Communications*, 5:5636. (Cited on pages 62 and 107.)

Schultes, S., Sourisseau, M., Le Masson, E., Lunven, M., and Marié, L. (2013). Influence of physical forcing on mesozooplankton communities at the Ushant tidal front. *Journal of Marine Systems*, 109–110, Supplement:S191–S202. (Cited on pages 18 and 58.)

Seity, Y., Brousseau, P., Malardel, S., Hello, G., Bénard, P., Bouttier, F., Lac, C., and Masson, V. (2011). The AROME-France convective-scale operational model. *Monthly Weather Review*, 139(3):976–991. (Cited on page 20.)

Serpette, A. and Mazé, R. (1989). Internal tides in the Bay of Biscay: a two-dimensional model. *Continental Shelf Research*, 9(9):795–821. (Cited on page 54.)

Simpson, J. H., Allen, C. M., and Morris, N. C. G. (1978). Fronts on the continental shelf. *Journal of Geophysical Research: Oceans*, 83(C9):4607–4614. (Cited on pages 17, 18 and 51.)

Simpson, J. H., Crisp, D. J., and Hearn, C. (1981). The Shelf-Sea Fronts: Implications of their Existence and Behaviour and Discussion. *Philosophical Transactions of the Royal Society of London A: Mathematical, Physical and Engineering Sciences*, 302(1472):531–546. (Cited on pages 17 and 18.)

Simpson, J. H. and Hunter, J. R. (1974). Fronts in the Irish Sea. *Nature*, 250(5465):404–406. (Cited on pages 17, 18, 51, 106 and 110.)

Soufflet, Y., Marchesiello, P., Lemarié, F., Jouanno, J., Capet, X., Debreu, L., and Benshila, R. (2016). On effective resolution in ocean models. *Ocean Modelling*, 98:36–50. (Cited on page 20.)

Sudre, J., Yahia, H., Pont, O., and Garçon, V. (2015). Ocean turbulent dynamics at super resolution from optimal multiresolution analysis and multiplicative cascade.

IEEE Transactions on Geoscience and Remote Sensing, 2015:TGRS–2014–00385.R2. (Cited on pages 25 and 26.)

Taylor, J. R. and Ferrari, R. (2010). Buoyancy and Wind-Driven Convection at Mixed Layer Density Fronts. *Journal of Physical Oceanography*, 40(6):1222–1242. (Cited on page 16.)

Thomas, L. N., Tandon, A., and Mahadevan, A. (2008). Submesoscale processes and dynamics. In Hecht, M. W. and Hasumi, H., editors, *Geophysical Monograph Series*, volume 177, pages 17–38. American Geophysical Union, Washington, D. C. (Cited on pages 10, 11 and 12.)

Turiel, A., Pérez-Vicente, C. J., and Grazzini, J. (2006). Numerical methods for the estimation of multifractal singularity spectra on sampled data: a comparative study. *Journal of Computational Physics*, 216(1):362–390. (Cited on page 25.)

Turiel, A., Solé, J., Nieves, V., Ballabrera-Poy, J., and García-Ladona, E. (2008a). Tracking oceanic currents by singularity analysis of Microwave Sea Surface Temperature images. *Remote Sensing of Environment*, 112(5):2246–2260. (Cited on page 26.)

Turiel, A., Yahia, H., and Pérez-Vicente, C. J. (2008b). Microcanonical multifractal formalism-a geometrical approach to multifractal systems: Part I. Singularity analysis. *Journal of Physics A: Mathematical and Theoretical*, 41(1):015501. (Cited on pages 25 and 26.)

Ullman, D. S. and Cornillon, P. C. (1999). Satellite-derived sea surface temperature fronts on the continental shelf off the northeast U.S. coast. *Journal of Geophysical Research: Oceans*, 104(C10):23459–23478. (Cited on page 17.)

Ullman, D. S. and Cornillon, P. C. (2001). Continental shelf surface thermal fronts in

winter off the northeast US coast. *Continental Shelf Research*, 21(11–12):1139–1156. (Cited on page 45.)

Umlauf, L. and Burchard, H. (2005). Second-order turbulence closure models for geophysical boundary layers. A review of recent work. *Continental Shelf Research*, 25(7):795–827. (Cited on page 20.)

van Aken, H. M. (2002). Surface currents in the Bay of Biscay as observed with drifters between 1995 and 1999. *Deep Sea Research Part I: Oceanographic Research Papers*, 49(6):1071–1086. (Cited on page 2.)

Yahia, H., Sudre, J., Pottier, C., and Garçon, V. (2010). Motion analysis in oceanographic satellite images using multiscale methods and the energy cascade. *Pattern Recognition*, 43(10):3591–3604. (Cited on pages 25 and 26.)

Yankovsky, A. E. and Chapman, D. C. (1997). A simple theory for the fate of buoyant coastal discharges*. *Journal of Physical Oceanography*, 27(7):1386–1401. (Cited on pages 45 and 47.)

Yelekçi, O., Charria, G., Capet, X., Reverdin, G., Sudre, J., and Yahia, H. (2017). Spatial and seasonal distributions of frontal activity over the French continental shelf in the Bay of Biscay. *Continental Shelf Research*, 144:65–79. (Cited on page 16.)